THESIS

EVIDENCE FOR A ROTATION IN ASTHENOSPHERIC FLOW IN NORTHWEST CANADA: INSIGHTS FROM SHEAR WAVE SPLITTING

Submitted by

Andrew R. Bolton

Department of Geosciences

In partial fulfillment of the requirements

For the Degree of Master of Science

Colorado State University

Fort Collins, Colorado

Spring 2021

Master's Committee:

Advisor: Derek L. Schutt

Richard C. Aster
F. Jay Breidt

ABSTRACT

EVIDENCE FOR A ROTATION IN ASTHENOSPHERIC FLOW IN NORTHWEST CANADA: INSIGHTS FROM SHEAR WAVE SPLITTING

The Mackenzie Mountains (MM) of northwest Canada are an actively uplifting, seismogenic salient of the northern Canadian Cordillera that lie 750 km NE of the nearest plate boundary. We present new shear wave splitting measurements for the region from a linear array which transects the region to characterize upper mantle anisotropy. A gradual rotation in anisotropy occurs across the Canadian Cordillera, with stations nearest to the craton yielding fast axis orientations that are subparallel to North America absolute plate motion (~230°). Moving SW from the craton, across the MM and towards the plate boundary, fast-axis orientations rotate to become aligned with major lithospheric fabrics (NW-SE). Previous work has shown that the Cordilleran lithosphere is thin (~50 km) in this region. We therefore interpret these results to primarily reflect sublithospheric flow. Three subduction-transpressional related hypotheses for flow are presented, where our preferred hypotheses invokes depth-dependent, subduction-induced flow.

ACKNOWLEDGEMENTS

I would like to thank Derek Schutt, my advisor, for the opportunity to be a part of the Mackenzie Mountain Earthscope Project and his unyielding patience with me throughout this project. Another big thanks to my fellow graduate students for their friendship and perspective they have given me throughout my time at CSU. I would further like to thank my family and my girlfriend Shannon for their support and the happiness they've brought me through this time. Furthermore I am very grateful to the NSF for their funding through grants 5300798, 5300799, and 5309798. All seismic data were downloaded through the IRIS Web Services (https://service.iris.edu/) for the Mackenzie Mountain Earthscope Project seismograph deployment (network code 7C, station codes MM01-MM41).

TABLE OF CONTENTS

LIST OF TABLES

LIST OF FIGURES

Chapter 1

1.1 Organization of Thesis

This thesis is formatted into three chapters. Chapter 1 gives an overview of all the background material necessary to understand this project. This overview includes information regarding seismic anisotropy, shear wave splitting, and the methodology utilized in this research. Chapter 2 is a prepared manuscript detailing some necessary background to the study, the method used, results determined, and a discussion of those results with conclusions. Chapter 2 is meant as a standalone study ready to be sent to Geophysical Journal International for publication. The final chapter details some ideas future work as well as an overview of how to repeat this study with the necessary data acquisition techniques and scripts developed. Chapter 3 serves as a guide for future graduate students and researchers to further this work.

1.2 Seismic Anisotropy

Seismic anisotropy is a term for the directional dependence of seismic wave velocities as they propagate through a medium. Anisotropy is generally caused by one of two end-member phenomena: shape preferred orientation (SPO) or lattice preferred orientation (LPO), also called crystallographic preferred orientation, (CPO) (e.g. *Long and Silver*, 2009). SPO describes anisotropy produced due to the alignment of elastically different materials, such as the foliation in metamorphic bodies, fractures, presence of fluid or melt within a medium, or stacking of different layers of media. LPO describes the alignment of crystallographic axes in anisotropic minerals that are not elastically distinct from one another (Figure 1.1, 1.2). In the upper mantle, anisotropy is commonly attributed to LPO development of olivine, the volumetrically dominant mineral phase (e.g. *Ben-Ismail and Mainprice*, 1998; *Frost*, 2008). Under certain conditions the olivine becomes mostly oriented along the crystallographic a-axis, creating directionally dependent seismic velocities as the a-axis has a higher shear and bulk modulus (e.g. *Hess*, 1964). This alignment occurs due to a glide plane along the a- and b-axes of the olivine crystal, which accommodates stress more read-

ily than other planes of weakness. In the lithosphere, olivine LPOs are thought to result from fossilized strain created from the most recent large-scale tectonic activity within the study region (*Crampin*, 1984; *Park and Levin*, 2002). In the asthenosphere these orientations are attributed to regional lateral mantle flow (*Crampin*, 1984; *Hanna and Long*, 2012).

Olivine LPO is produced from deformation within the dislocation creep regime, as confirmed both by microstructures observed in mantle xenoliths and experimentally deformed olivine. (*Green II and Radcliffe*, 1972; *Gueguen*, 1977; *Jin et al.*, 1989; *Karato and Wu*, 1993). Dislocation creep occurs due to atomic imperfections within the crystal lattice. These imperfections can be organized into two end-member types: edge dislocations and screw dislocations. These dislocations are defined by their Burgers vector, which denotes the direction of slip that occurs when a dislocation moves through a crystal lattice. Edge dislocations form as a result of a half-plane of atoms within the lattice structure, which creates compressional stresses above the edge dislocation (the last atom on the half-plane) and tensional stresses below it, and have a Burgers vector perpendicular to the half plane. Screw dislocations consist of a rotation out of the plane of the crystal lattice, which pushes some atom-planes outward from the crystal center and others inward, similar to the threads on a screw, with a Burgers vector parallel to this motion (Figure 1.3) (*Stein and Wysession*, 2003; *Turcotte and Schubert*, 2014). The dislocation creep regime occurs at high strain rates and large grain sizes, which produce a non-linear rheology in the crystal body. This creep regime is thought to dominate upper mantle rheology (*Karato and Wu*, 1993; *Ranalli and Fischer*, 1984). In the lower mantle, olivine deformation is not thought to produce anisotropy, as decreases in grain size coupled with increases in temperature and pressure push the lower mantle into the diffusion creep regime, where deformation doesn't result in LPO (e.g. *Long and Silver*, 2009). Diffusion creep results from the migration of atoms through vacancies present in the interiors of crystal grains when subjected to stress. This change in creep regime explains why the lower mantle is generally thought to be isotropic despite being predominantly composed of anisotropic minerals such as bridgemanite (*Karato et al.*, 1995). These assertions of an isotropic lower mantle are compounded by laboratory studies that indicate random orientations in perovskite-structured analog crystals at

lower mantle temperatures and pressures (*Karato et al.*, 1995); however, some studies question the validity of using analogs to investigate deep mantle structures (e.g. *Cordier et al.*, 2004). Because of these observations, anisotropic measurements within the mantle are often inferred to stem solely from the upper mantle. One should note that despite the generally isotropic lower mantle, the D" region is thought to be anisotropic, and can be probed by comparing SKS and SKKS arrivals at the same station (e.g. *Kendall*, 2007).

The elasticity tensor, which relates the second-order stress tensor to the second-order strain tensor, gives information regarding the strength of an elastic medium in all directions. This tensor is fourth-order and, due to the various symmetries can have between 2 and 21 independent components. In the case of a two-component elastic tensor, the elastic material is isotropic and is described only by the first Lamé parameter λ and the shear modulus μ. If the elastic tensor has more than two independent components, then the given elastic material is anisotropic. In shear wave splitting studies, hexagonal symmetry of anisotropy is often assumed, which reduces the number of independent terms in the elastic tensor to 6 (e.g. *Stein and Wysession*, 2003). This assumption is made because the alignment of olivine a-axes does not guarantee alignment of the crystallographic b- or c-axes in these orthorhombic crystals, and random orientations of b- and c-axes within nearby crystals approximates a hexagonal symmetry (Figure 1.1) (e.g. *Savage*, 1999). However, this approximation is not always sufficient to explain upper mantle anisotropy (e.g. *Savage*, 1999).

The type of olivine anisotropy described above is termed A-type anisotropy, but there are five different olivine fabric types that have been observed in laboratory studies (e.g. *Karato et al.*, 2008). These fabric types vary by the crystallographic slip system. For example, A-type olivine fabrics form, as described above through the [100](010) slip system; the bracketed [100] refers to the crystallographic axis that the slip occurs in, and the parenthetical (010) refers to which crystallographic axis is a vector normal to the plane that accommodates slip (*Skemer and Hansen*, 2016) (Figure 1.4). The position of the digits denotes the particular axis related to that slip (i.e. these slip-system are denoted by (a b c)[a b c]). B-type olivine fabrics are thought to form within

the mantle wedges in some subduction zones or in partially melted rock, with the [001](010) slip system being dominant (*Mizukami et al.*, 2004; *Skemer and Hansen*, 2016). C-type fabrics have been identified in deep mantle xenoliths and correspond to the [001](100) slip system. D-type fabrics are likely the second-most abundant fabric after A-type; these fabrics have a dominant slip system of [100](0kl), and occur when the [100](010) and [100](001) slip systems have similar strength (*Bernard et al.*, 2019). The k and l terms within D-type anisotropy signifies that slip can occur on any plane along the a-axis. The final E-type olivine fabric has the slip system [100](001) (*Karato et al.*, 2008). B-, C-, and E-type fabrics are thought to only control 7%, 7%, and 2% of the global olivine fabrics, respectively, and are typically disregarded in shear wave splitting studies (*Long and Silver*, 2009). The geometry of the anisotropy generally does not change the relationship between mantle flow and fast-axis orientation for any fabric besides B-type, which is geographically sparse (*Long and Silver*, 2009; *Skemer and Hansen*, 2016). In other words, the relationship between fast direction of anisotropy and mantle flow direction is the same for all olivine anisotropy types except B-. In all cases except B-type anisotropy, the fastest propagation direction for seismic waves traveling through this anisotropic media will be subparallel to the flow direction of the mantle.

1.3 Shear Wave Splitting

Shear wave splitting is one of the most common methods used to determine mantle anisotropy. These types of studies typically use SKS, SKKS, PKS, and similar phases, (refered to as XKS for the remainder of this paper) (Figure 1.5). XKS phases are useful because they propagate through the outer core as a P-wave and then convert to an S-wave on the receiver-side of the ray path. Due to the coupling of P- and S_V-waves, any S_H energy within the source-side S-wave in the SKS or SKKS phase will be reflected at the core-mantle boundary, while some S_V energy transmits as a P-wave. Some of this P- energy within the outer core will then convert back into S_V energy upon re-entry into the mantle, and at this point the XKS will have a known polarization in the plane between source and receiver. For this reason, we generally rotate our seismograms into radial and

transverse directions, where the radial direction is the horizontal projection of the source-receiver plane, and the transverse is orthogonal to the radial. Furthermore, any anisotropy measured from an XKS phase must occur on the receiver-side leg of the ray path since any signature of anisotropy from the source-side leg is destroyed upon entering the outer core. The receiver-side S-wave continues to be polarized in the S_V direction so long as it stays within an isotropic medium, such as the lower mantle. When the S-wave encounters a hexagonally anisotropic medium, it splits into two orthogonal quasi S-waves; one wave is polarized parallel to the fast direction of anisotropy and the second perpendicular to that direction (Figure 1.1). The wave polarized along the fast direction is termed the "fast wave" and its orthogonal pair is termed the "slow wave." If the incoming S-wave is perfectly parallel or perpendicular to the fast direction of hexagonal anisotropy, no splitting will occur - waves of this nature are called null measurements or null splits, an example of which can be seen in Figure 1.6 (*Menke and Levin*, 2003; *Silver and Chan*, 1991). The two quasi S-waves are measured by the horizontal channels of the seismograph due to the near-vertical incidence (and therefore near-horizontal particle motion) as the XKS phase approach the surface. Due to this vertical incidence, hexagonal anisotropy that is also vertical will not produce a shear wave split (e.g. *Savage*, 1999). It is easy to observe null splits on the radial and transverse traces, as XKS energy is solely observed on the radial channel (Figure 1.7).

Anisotropy is typically quantified in terms of the fast-axis azimuth, ϕ, and the delay time between fast and slow arrivals at the seismometer, δt. Fast-axis orientations allow one to quantify the directionality of the anisotropy, whereas delay time (also called split time) is generally interpreted to suggest the thickness of the anisotropic medium. S_V waves traveling through peridotite are estimated to have around 4% anisotropy; hence waves traveling along the fast-axis have velocities 4% greater than those traveling in the slow-direction (e.g. *Crampin*, 1981; *Peselnick and Nicolas*, 1978).

Given this simplified view of peridotite anisotropy, the source function $s(t)$ of the shear wave split will have the following relations on radial and transverse waveforms, given that the peri-

dotite is hexagonally symmetric, horizontally oriented, and the incoming XKS phase has vertical incidence:

$$R(t) = s(t)\cos^2\phi + s(t-\delta t)\sin^2\phi \tag{1.1}$$

$$T(t) = \left[\frac{s(t) - s(t-\delta t)}{2}\right]\sin 2\phi \tag{1.2}$$

The above equation holds true under the assumption that the thickness of the anisotropic layer is much greater than the ($\sim$40 km) wavelength of the incident XKS wave (i.e. this is a ray theoretical approximation). (*Stein and Wysession*, 2003).

1.4 The Whittle Likelihood Estimation Method

We use a method developed by *Corbalán* (2016); *Corbalán et al.* (in revision), which builds upon the cross-convolution method described in *Menke and Levin* (2003). A convolution describes how the shape of one function is altered by a second function. The convolution theorem is described as:

$$f(t) * g(t) = (f * g)(t) = \int_{-\infty}^{\infty} f(\tau)g(t-\tau)d\tau \tag{1.3}$$

The cross-convolution method of *Menke and Levin* (2003) shows that for a true anisotropic model m_0, the radial waveform convolved with the tangential impulse response τ is exactly equal to the transverse waveform convolved with the radial impulse response ρ:

$$R(t) * \tau_{m_0} = T(t) * \rho_{m_0} \tag{1.4}$$

Therefore, to find the true anisotropic model one can minimize the function:

$$\|R(t) * \tau_m - T(t) * \rho_m\|^2 \tag{1.5}$$

over likely values of anisotropy m, which is usually described in terms of fast-axis orientation, ϕ, and delay time between fast and slow waves, δt. The *Menke and Levin* (2003) method also approximates the impulse response functions for radial (ρ_m) and transverse (τ_m) signals for single-layer anisotropy with normally incident shear waves. These impulse response functions are:

$$\rho_m = \rho_1 \delta(t) + \rho_2 \delta(t - \delta t) \tag{1.6}$$

$$\tau_m = \tau_1 \delta(t) + \tau_2 \delta(t - \delta t)$$

$$\rho_1 = \cos^2 \phi - \theta$$

$$\rho_2 = \sin^2 \phi - \theta$$

$$\tau_1 = -\tau_2 = \cos \phi - \theta \sin \phi - \theta$$

where θ represents the backazimuth of the event. *Menke and Levin* (2003) also demonstrate that this method is well suited for application to two layers of anisotropy.

A major issue in shear wave splitting methods is uncertainty estimation (*Sandvol and Hearn*, 1994; *Walsh et al.*, 2013). In some cases shear wave splitting measurements can have uncertainties in fast-axis orientation as high as 90° or split times of greater than 1 s, making those measurements functionally useless to determine mantle processes. For example, note that Equation 1.5 will not be exactly zero if there is noise present in $R(t)$ or $T(t)$, and is thus a source of uncertainty. The *Corbalán* (2016); *Corbalán et al.* (in revision) Whittle Likelihood Estimation Method, herein referred to as the WLEM, builds upon the *Menke and Levin* (2003) cross-convolution method by better quantifying the effects of pre-event microseismic noise on the estimation of m_0. By taking into account the effects of pre-event noise, this method can better constrain uncertainties of ϕ and δt. The resulting likelihoods from multiple events observed at one location can be summed to produce a more accurate estimation of the station-averaged splitting parameters, as opposed to other techniques that make approximations to estimate station averages (*Schutt et al.*, 1998; *Wolfe and Silver*, 1998).

Corbalán (2016); *Corbalán et al.* (in revision) assumes a vertically incident XKS phase travelling through a non-dipping, hexagonally anisotropic medium to derive a formula for the spectral characteristics of the pre-event noise. This method transforms the pre-event noise time series into the frequency domain and computes normalized radial and transverse noise spectra that are then smoothed to produce stable estimates of the noise spectral density (*Corbalán*, 2016; *Corbalán et al.*, in revision). With these known spectral characteristics, the WLEM runs a grid search over plausible values of the cross-convolution radial and tangential impulse response parameters ρ_m and τ_m, specifically varying fast-axis orientation ϕ (0-180°) and integer-valued lag, $L = \frac{\delta t}{SI}$, where SI is the sampling interval. A theoretical spectral density is calculated using the grid search parameters to compare with the spectral density of the cross-convolved signal in Equation 1.5. These spectral densities are compared using a Whittle likelihood approximation (*Whittle*, 1953). The splitting parameter grid search produces a log-likelihood surface whose maximum is the best-fit splitting parameters $\hat{\phi}$ and $\hat{\delta t}$ (*Corbalán*, 2016; *Corbalán et al.*, in revision). The data must be windowed such that grid-searched models with different lag values use the same number of observations, N (i.e. the data must have a uniform sampling rate).

The uncertainty of the best-fitting parameters $\hat{\phi}$ and $\hat{\delta t}$ is assessed by perturbing the signal with randomly phase-shifted microseismic noise, which is obtained by cutting the trace before the determined XKS arrival (*Corbalán*, 2016; *Corbalán et al.*, in revision). Synthetic radial and transverse traces are produced with input anisotropic parameters $\hat{\phi}$ and $\hat{\delta t}$. The pre-event noise is extracted from the input signals $R(t)$ and $T(t)$ and randomly phase-shifted over 100 bootstrap realizations, b. For each realization new likelihood surfaces are generated with new maxima and thus new best-fitting splitting parameters $\hat{\phi}_b$ and $\hat{\delta t}_b$ (*Corbalán*, 2016; *Corbalán et al.*, in revision). The WLEM then assesses the distribution of $\hat{\phi}_b$ and $\hat{\delta t}_b$ values about the true best-fit splitting parameters $\hat{\phi}$ and $\hat{\delta t}$ to give an estimate of the uncertainty. After performing this uncertainty analysis for each event recorded at a station of interest, the station-event likelihood surfaces are then summed to generate a station "average" likelihood surface whose maximum represents the

best-fitting anisotropic parameters for all events. The bootstrapping uncertainty analysis is then performed on the summed likelihood surface to assess station-average uncertainty.

We note that due to some inconsistencies in the WLEM code, we opted to use SplitLab (*Wüstefeld et al.*, 2008) to determine shear wave splitting measurements for our study. In synthetic tests, the cloud of bootstrapping estimates did not cover the input anisotropy used to create the synthetic traces; we also observed an azimuthal dependence on best-fitting splitting parameters in synthetic tests with realistic signal-to-noise ratios (SNR) (e.g. 5), though this dependence does not show up for large, unrealtistic SNR values (e.g. 1000). These synthetic traces were created using Telewavesim (*Audet et al.*, 2019a), and tested the assumptions of the WLEM by generating synthetic traces with a vertically incident raypath passing through a single-layer of hexagonally anisotropic upper mantle.

1.5 SplitLab

SplitLab (*Wüstefeld et al.*, 2008) is a MATLAB user interface for shear-wave splitting. This package allows users to query FDSN (International Federation of Digital Seismograph Networks) servers to download North-East-Vertical (NEZ) seismograms and manually process them per-event at a given station. After windowing the arrival, SplitLab computes individual station-event best-fitting splitting parameters using the rotation correlation (RC) method (*Bowman and Ando*, 1987), minimum energy (ME) method (*Silver and Chan*, 1991), and eigenvalue minimization method (EV) (also *Silver and Chan*, 1991). These best-fitting splitting parameters are computed via grid search over likely values of ϕ (from -90 to 90 degrees) and δt (from 0 to 4 s). SKS signals are windowed about the arrival in NEZ and these traces are rotated to compute the best-fitting parameters. The rotation correlation method used in *Bowman and Ando* (1987) maximizes the correlation coefficient between radial and transverse traces. The *Silver and Chan* (1991) minimum energy method finds the minimum displacement energy on transverse traces, and the final eigenvalue minimization method maximizing the λ_1 or λ_1/λ_2 eigenvalues and minimizing the λ_2 or $\lambda_1 * \lambda_2$. The

user defines which two methods they would like to obtain δt-ϕ maps of, though all three methods will compute results.

For our SplitLab analysis, we focus on the RC and ME methods. We applied a filter on each trace, either a lowpass filter with 0.4 Hz corner or a bandpass filter with corner frequencies of 0.01 Hz and either 0.3 or 0.4 Hz. Filter corners were determined manually based on the characteristics of each signal and noise. SKS windowing is also chosen manually and cover at least a whole period of the arriving SKS. We assign a manual quality to each filtered and windowed waveform, based on the agreement between RC and ME methods. We assign qualities of "Good," "Fair," or "Poor" to the waveforms, based on agreement between RC and ME methods' fast-axes and delay times as well as linearity of particle motion after the rotation correction. Good quality arrivals have a very linear particle motion, and poorer quality results have less linear particle motion.

1.6 Figures

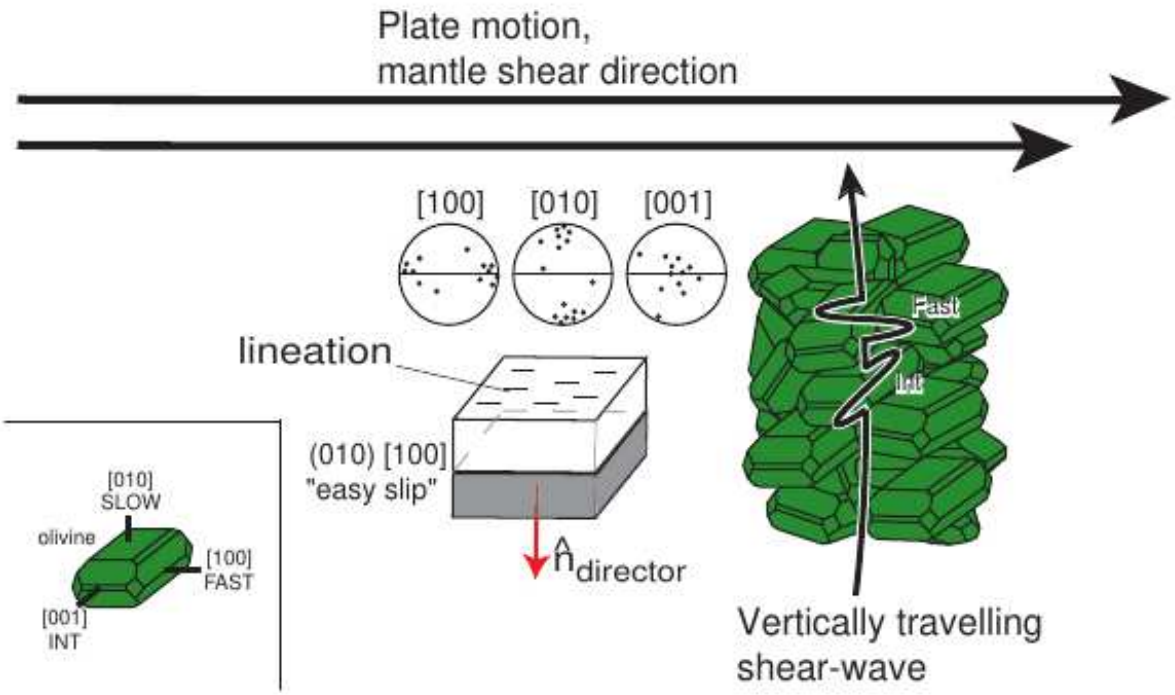

Figure 1.1: Schematic example of A-type aligned olivine and the splitting of a shear wave. The bottom-left inset shows a single olivine crystal with crystallographic axes labeled. In the middle lineations are shown, that are aligned parallel to the maximum shear direction (arrows above). The rightmost schematic depicts a collection of olivine crystals with generally aligned fast-axes splitting a shear wave into two orthogonal waves. The fast wave is polarized parallel to the crystallographic fast-axes while the slow wave is polarized parallel to the horizontal slow axis. After *Lev* (2009).

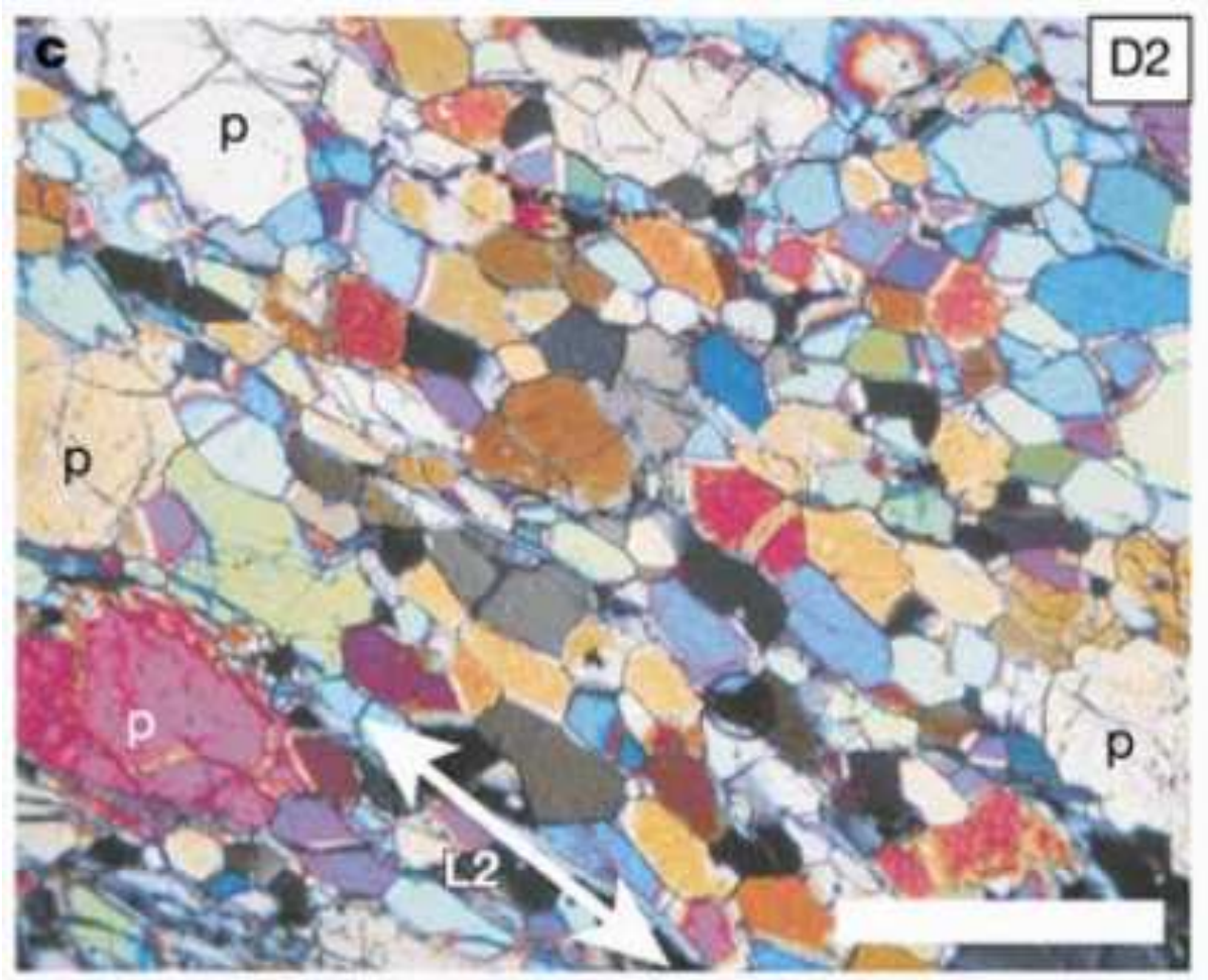

Figure 1.2: Natural example of olivine grains showing lattice preferred orientation (LPO) in a photomicrograph of the Higashi - Akaishi dunite of southwest Japan. Note that grains are aligned along L2 direction. p denotes coarse porphyroclasts within the dunite, but are generally irrelevant for the LPO alignment. After *Mizukami et al.* (2004).

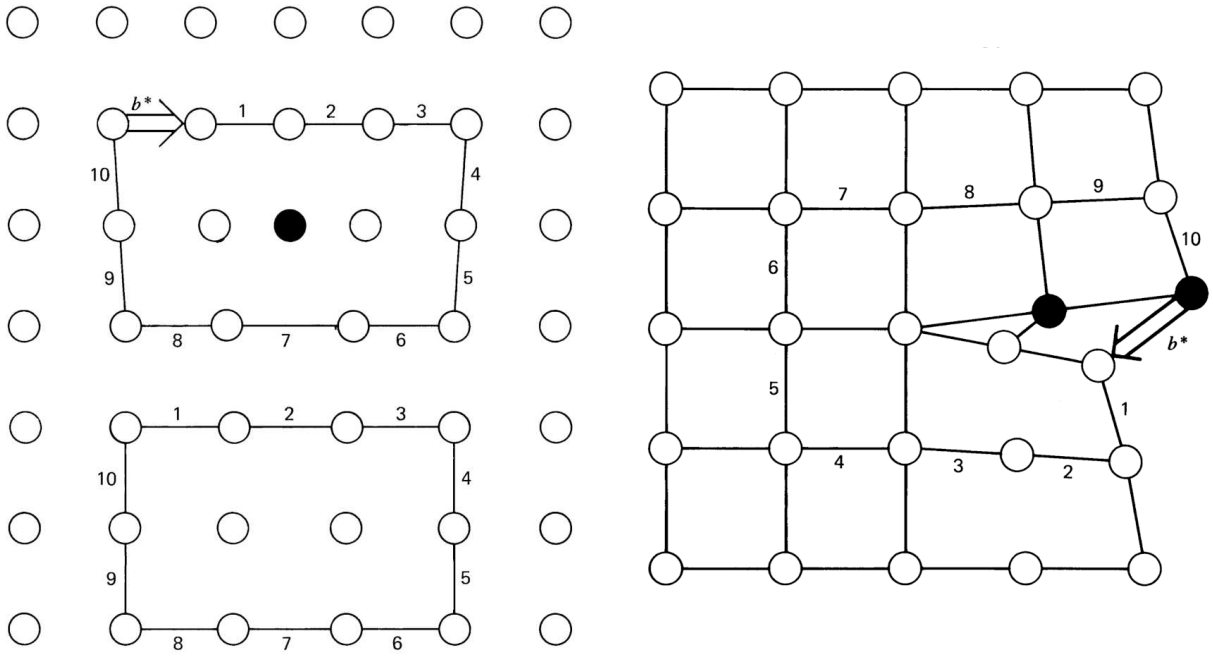

Figure 1.3: Examples of dislocation creep mechanisms. Edge dislocation (left, black circle) shows an inserted half plane of atoms between two whole-planes of atoms. The edge dislocation is denoted by the last atom along the half plane. The Burgers vector, $b*$, is perpendicular to the half plane of atoms in this case. The edge dislocation (right) shows deformation out of the plane of the atoms, parallel to the direction of the Burgers vector. Figures 7.9 and 7.10 in *Turcotte and Schubert* (2014).

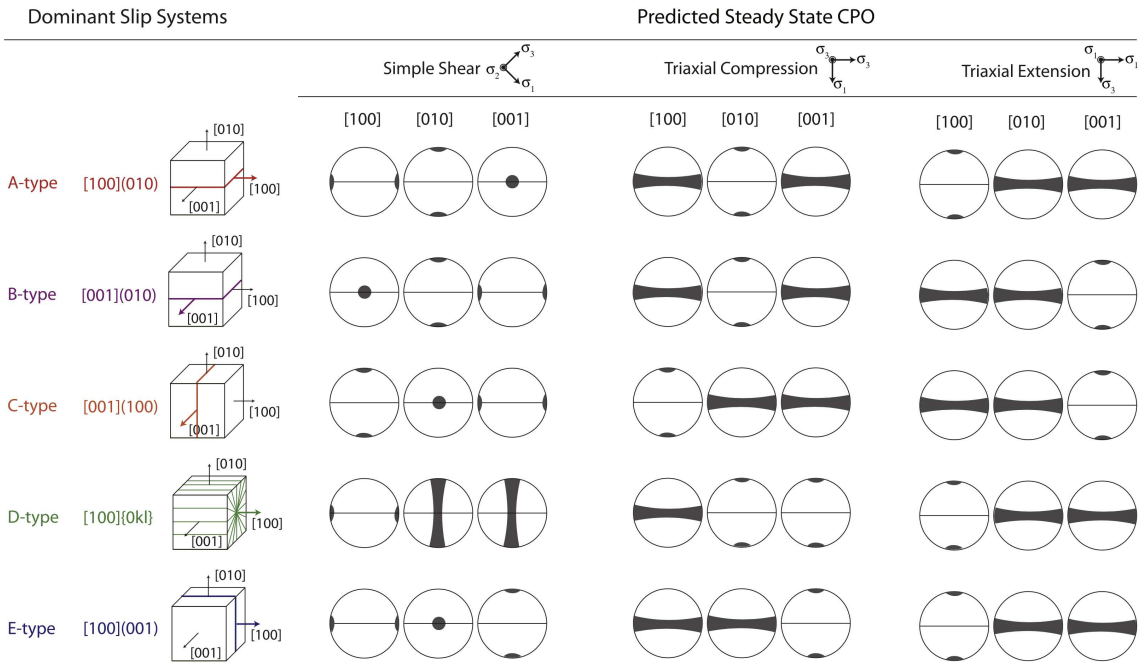

Figure 1.4: Olivine anisotropic slip systems and predicted LPO response. After *Skemer and Hansen* (2016).

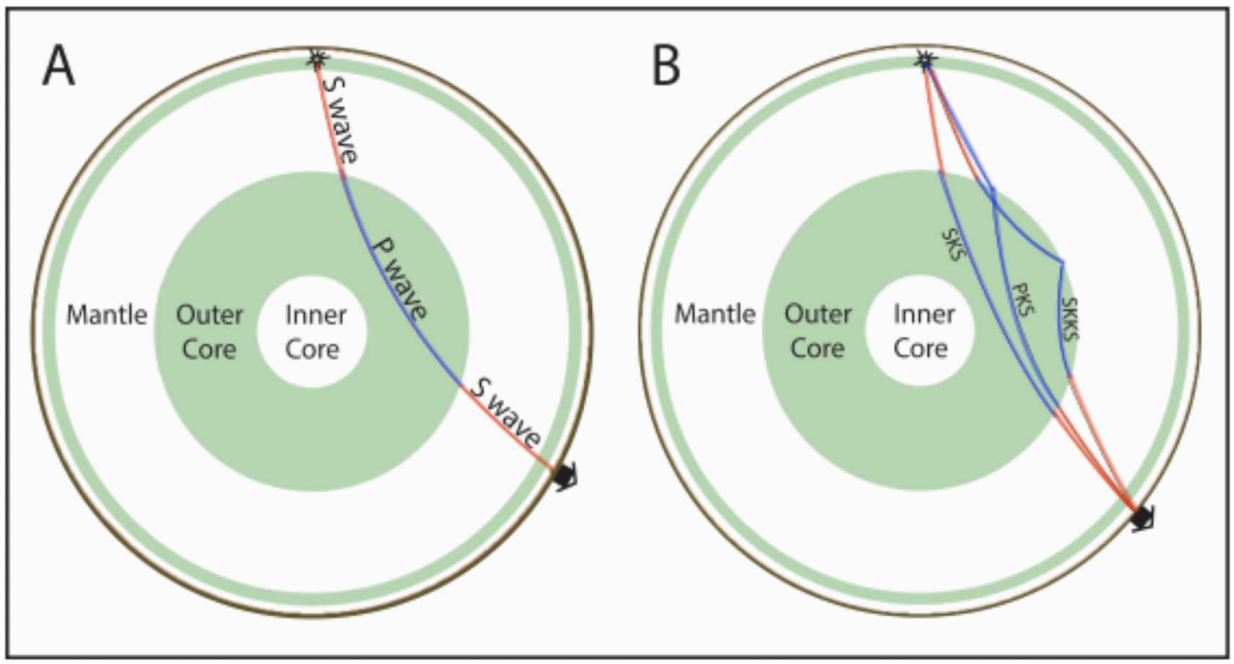

Figure 1.5: (A) An SKS phase traveling from source to receiver. In seismology the *K* denotes a wave traveling through the outer core; this phase must travel as a compressional wave as shear waves cannot propagate through liquid. (B) Raypaths for SKS, SKKS, and PKS phases. Note that they sample different areas of the mantle but arrive at the same station. S-waves are shown as red lines, P-waves as blue. After *Crotwell et al.* (1999).

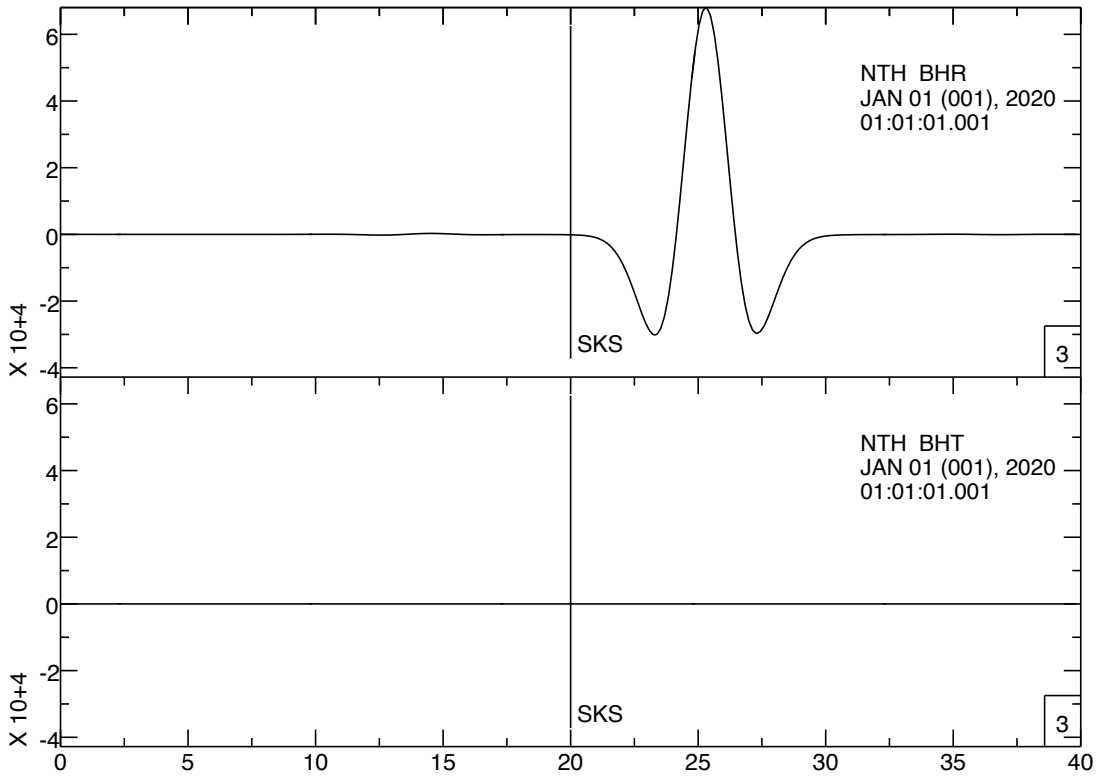

Figure 1.6: A noiseless synthetic null split in which fast-axis orientation is parallel to the backazimuth (i.e. initial polarization) of the incident S_V wave. These data were rotated to radial (top) and transverse (bottom) direction. Note the lack of transverse energy. Synthetics generated by Telewavesim (*Audet et al.*, 2019a).

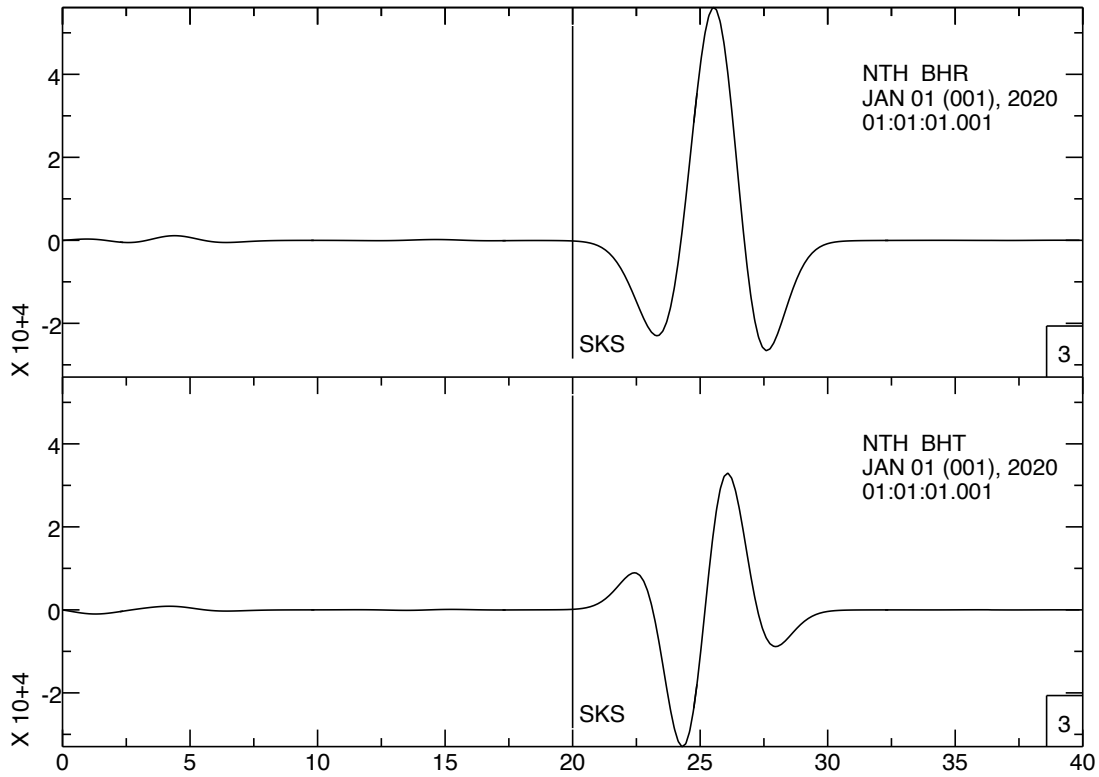

Figure 1.7: A noiseless synthetic shear wave split in which fast-axis orientation is 30° from backazimuth (i.e. initial polarization) of the incident S_V wave in radial (top) and transverse (below). Synthetics generated by Telewavesim (*Audet et al.*, 2019a).

Bibliography

Alsina, D., and R. Snieder (1995), Small-scale sublithospheric continental mantle deformation: constraints from SKS splitting observations, *Geophysical Journal International*, *123*(2), 431–448, doi:10.1111/j.1365-246X.1995.tb06864.x.

Argus, D. F., R. G. Gordon, M. B. Heflin, C. Ma, R. J. Eanes, P. Willis, W. R. Peltier, and S. E. Owen (2010), The angular velocities of the plates and the velocity of Earth's centre from space geodesy, *Geophysical Journal International*, *180*(3), 913–960, doi:10.1111/j.1365-246X.2009.04463.x.

Audet, P., C. Sole, and A. J. Schaeffer (2016), Control of lithospheric inheritance on neotectonic activity in northwestern Canada?, *Geology*, *44*(10), 807–810.

Audet, P., C. J. Thomson, M. G. Bostock, and T. Eulenfeld (2019a), Telewavesim: Python software for teleseismic body wave modeling, doi:10.5281/zenodo.3551258.

Audet, P., C. A. Currie, A. J. Schaeffer, and A. M. Hill (2019b), Seismic Evidence for Lithospheric Thinning and Heat in the northern Canadian Cordillera, *Geophysical Research Letters*, *46*(8), 4249–4257, doi:10.1029/2019GL082406.

Baker, M. G., D. C. Heath, D. L. Schutt, R. C. Aster, J. F. Cubley, and J. T. Freymueller (2020), The Mackenzie Mountains EarthScope Project: Studying Active Deformation in the Northern North American Cordillera from Margin to Craton, *Seismological Research Letters*, *91*(1), 521–532, doi:10.1785/0220190139.

Ben-Ismail, W., and D. Mainprice (1998), An olivine fabric database: an overview of upper mantle fabrics and seismic anisotropy, *Tectonophysics*, *296*, 145–157.

Bernard, R. E., W. M. Behr, T. W. Becker, and D. J. Young (2019), Relationships Between Olivine CPO and Deformation Parameters in Naturally Deformed Rocks and Implications for Mantle

Seismic Anisotropy, *Geochemistry, Geophysics, Geosystems*, *20*(7), 3469–3494, doi:10.1029/2019GC008289.

Bowman, J. R., and M. Ando (1987), Shear-wave splitting in the upper-mantle wedge above the Tonga subduction zone, *Geophysical Journal International*, *88*(1), 25–41, doi:10.1111/j.1365-246X.1987.tb01367.x.

Clowes, R., P. Hammer, G. Fernandez-Viejo, and K. Welford (2005), Lithospheric structure in northwestern Canada from LITHOPROBE seismic refraction and related studies: a synthesis, *Canadian Journal of Earth Sciences*, *42*, 1277–1293, doi:10.1139/e04-069.

Colpron, M., and J. L. Nelson (2011), A digital atlas of terranes for the northern Cordillera, *Yukon Geological Survey*.

Corbalán, A. (2016), A new method to test shear wave splitting: improving statistical assessment of splitting parameters.

Corbalán, A., F. Breidt, D. Witt, and D. Schutt (in revision), Whittle Likelihood Estimation of Shear-wave Splitting Parameters in the Presence of Highly-Corrleted Microseismic Noise.

Cordier, P., T. Ungár, L. Zsoldos, and G. Tichy (2004), Dislocation creep in MgSiO3 perovskite at conditions of the Earth's uppermost lower mantle, *Nature*, *428*, 837–40, doi:10.1038/nature02472.

Courtier, A., J. Gaherty, J. Revenaugh, M. Bostock, and E. Garnero (2010), Seismic anisotropy associated with continental lithosphere accretion beneath the CANOE array, Northwestern Canada, *Geology*, *38*(10), 887–890, doi:10.1130/G31120.1.

Crampin, S. (1981), A review of wave motion in anisotropic and cracked elastic-media, *Wave motion*, *3*(4), 343–391.

Crampin, S. (1984), An introduction to wave propagation in anisotropic media, *Geophysical Journal of the Royal Astronomical Society*, *76*(1), 17–28, doi:10.1111/j.1365-246X.1984.tb05018.x.

Crotwell, H. P., T. J. Owens, and J. Ritsema (1999), The TauP Toolkit: Flexible Seismic Travel-time and Ray-path Utilities, *Seismological Research Letters*, *70*(2), 154–160, doi:10.1785/gssrl.70.2.154.

Debayle, E., and M. Sambridge (2004), Inversion of massive surface wave data sets: Model construction and resolution assessment, *Journal of Geophysical Research: Solid Earth*, *109*(B2), doi:10.1029/2003JB002652.

Eddy, C. L., G. Ekström, M. Nettles, and J. B. Gaherty (2018), Age dependence and anisotropy of surface-wave phase velocities in the Pacific, *Geophysical Journal International*, *216*(1), 640–658, doi:10.1093/gji/ggy438.

Eken, T., and F. Tilmann (2014), The Use of Direct Shear Waves in Quantifying Seismic Anisotropy: Exploiting Regional Arrays, *Bulletin of the Seismological Society of America*, *104*, 2644–2661, doi:10.1785/0120140020.

Enkelmann, E., E. Finzel, and J. Arkle (2019), Deformation at the eastern margin of the Northern Canadian Cordillera: Potentially related to opening of the North Atlantic, *Terra Nova*, *31*(3), 151–158, doi:10.1111/ter.12374.

Estève, C., P. Audet, A. J. Schaeffer, D. L. Schutt, R. C. Aster, and J. F. Cubley (2020), Seismic evidence for craton chiseling and displacement of lithospheric mantle by the Tintina fault in the northern Canadian Cordillera, *Geology*, doi:10.1130/G47688.1.

Finzel, E. S., L. M. Flesch, K. D. Ridgway, W. E. Holt, and A. Ghosh (2015), Surface motions and intraplate continental deformation in Alaska driven by mantle flow, *Geophysical Research Letters*, *42*(11), 4350–4358, doi:10.1002/2015GL063987.

Frederiksen, A., M. Bostock, and J. Cassidy (2001), S-wave velocity structure of the Canadian upper mantle, *Physics of the Earth and Planetary Interiors*, *124*(3), 175 – 191, doi:https://doi.org/10.1016/S0031-9201(01)00194-7.

Frost, D. J. (2008), The upper mantle and transition zone, *Elements*, *4*(3), 171–176.

Gabrielse, H. (1985), Major dextral transcurrent displacements along the Northern Rocky Mountain Trench and related lineaments in north-central British Columbia, *GSA Bulletin*, *96*(1), 1–14, doi:10.1130/0016-7606(1985)96<1:MDTDAT>2.0.CO;2.

Green II, H. W., and S. V. Radcliffe (1972), *Deformation Processes in the Upper Mantle*, pp. 139–156, American Geophysical Union (AGU), doi:10.1029/GM016p0139.

Gueguen, Y. (1977), Dislocations in mantle peridotite nodules, *Tectonophysics*, *39*(1), 231 – 254, doi:https://doi.org/10.1016/0040-1951(77)90098-1, fabrics, microstructures, and microtectonics.

Hanna, J., and M. D. Long (2012), SKS splitting beneath Alaska: Regional variability and implications for subduction processes at a slab edge.

Hayward, N. (2015), Geophysical investigation and reconstruction of lithospheric structure and its control on geology, structure, and mineralization in the Cordillera of northern Canada and eastern Alaska, *Tectonics*, *34*(10), 2165–2189, doi:https://doi.org/10.1002/2015TC003871.

Hess, H. (1964), Seismic anisotropy of the uppermost mantle under oceans, *Nature*, *203*(4945), 629.

Hyndman, R., P. Flueck, S. Mazzotti, T. J Lewis, J. Ristau, and L. Leonard (2005), Current tectonics of the northern Canadian Cordillera, *Canadian Journal of Earth Sciences*, *42*, 1117–1136, doi:10.1139/e05-023.

Jin, Z.-M., H. Green, and R. Borch (1989), Microstructures of olivine and stresses in the upper mantle beneath Eastern China, *Tectonophysics*, *169*(1), 23 – 50, doi:https://doi.org/10.1016/0040-1951(89)90181-9.

Karato, S., and P. Wu (1993), Rheology of the Upper Mantle: A Synthesis, *Science*, *260*(5109), 771–778.

Karato, S., S. Zhang, and H.-R. Wenk (1995), Superplasticity in Earth's Lower Mantle: Evidence from Seismic Anisotropy and Rock Physics, *Science*, *270*(5235), 458–461.

Karato, S.-I. (2013), *Rheological Properties of Minerals and Rocks*, chap. 4, pp. 94–144, John Wiley Sons, Ltd, doi:https://doi.org/10.1002/9781118529492.ch4.

Karato, S.-i., H. Jung, I. Katayama, and P. Skemer (2008), Geodynamic Significance of Seismic Anisotropy of the Upper Mantle: New Insights from Laboratory Studies, *Annu. Rev. Earth Planet. Sci.*, *36*, 59–95, doi:10.1146/annurev.earth.36.031207.124120.

Kendall, M. (2007), *D´´, Anisotropy*, pp. 146–149, Springer Netherlands, Dordrecht, doi:10.1007/978-1-4020-4423-6_61.

Kennett, B. L. N., E. R. Engdahl, and R. Buland (1995), Constraints on seismic velocities in the Earth from traveltimes, *Geophysical Journal International*, *122*(1), 108–124, doi:10.1111/j.1365-246X.1995.tb03540.x.

Langston, C. A. (1977), The effect of planar dipping structure on source and receiver responses for constant ray parameter, *Bulletin of the Seismological Society of America*, *67*(4), 1029–1050.

Leonard, L. J., S. Mazzotti, and R. D. Hyndman (2008), Deformation rates estimated from earthquakes in the northern Cordillera of Canada and eastern Alaska, *Journal of Geophysical Research: Solid Earth*, *113*(B8), doi:10.1029/2007JB005456.

Lev, E. (2009), Elastic and viscous anisotropy in Earth's mantle - observations and implications, Ph.D. thesis, Massachusetts Institute of Technology.

Lewis, T. J., R. D. Hyndman, and P. Flück (2003), Heat flow, heat generation, and crustal temperatures in the northern Canadian Cordillera: Thermal control of tectonics, *Journal of Geophysical Research: Solid Earth*, *108*(B6), doi:https://doi.org/10.1029/2002JB002090.

Long, M. D., and P. G. Silver (2009), Shear Wave Splitting and Mantle Anisotropy: Measurements, Interpretations, and New Directions, *Surveys in Geophysics*, *30*(4), 407–461, doi: 10.1007/s10712-009-9075-1.

Mazzotti, S., and R. Hyndman (2002), Yakutat collision and strain transfer across the northern Canadian Cordillera, *Geology*, *30*, doi:10.1130/0091-7613(2002)030<0495:YCASTA>2.0.CO; 2.

McNamara, D. E., and T. J. Owens (1993), Azimuthal shear wave velocity anisotropy in the Basin and Range Province using moho Ps converted phases, *Journal of Geophysical Research: Solid Earth*, *98*(B7), 12,003–12,017, doi:10.1029/93JB00711.

Menke, W., and V. Levin (2003), The cross-convolution method for interpreting SKS splitting observations, with application to one and two-layer anisotropic earth models, *Geophysical Journal International*, *154*(2), 379–392, doi:10.1046/j.1365-246X.2003.01937.x.

Mizukami, T., S. R. Wallis, and J. Yamamoto (2004), Natural examples of olivine lattice preferred orientation patterns with a flow-normal a-axis maximum, *Nature*, *427*(6973), 432–436.

Monger, J., and R. Price (2002), The Canadian Cordillera: Geology and Tectonic Evolution, *CSEG Recorder*, p. 17.

Montagner, J.-P., and T. Tanimoto (1991), Global upper mantle tomography of seismic velocities and anisotropies, *Journal of Geophysical Research: Solid Earth*, *96*(B12), 20,337–20,351, doi: 10.1029/91JB01890.

Nelson, J. L., M. Colpron, and S. Israel (2013), The Cordillera of British Columbia, Yukon, and Alaska: Tectonics and Metallogeny, in *Tectonics, Metallogeny, and Discovery: The North American Cordillera and Similar Accretionary Settings*, Society of Economic Geologists, doi: 10.5382/SP.17.03.

Oldow, J. S., A. W. Bally, and H. G. Ave Lallemant (1990), Transpression, orogenic float, and lithospheric balance, *Geology*, *18*(10), 991–994, doi:10.1130/0091-7613(1990)018<0991:TOFALB>2.3.CO;2.

Owens, T. J., H. P. Crotwell, C. Groves, and P. Oliver-Paul (2004), SOD: Standing order for data, *Seismological Research Letters - SEISMOL RES LETT*, *75*, 515–520, doi:10.1785/gssrl.75.4.515-a.

Park, J., and V. Levin (2002), Seismic Anisotropy: Tracing Plate Dynamics in the Mantle, *Science*, *296*(5567), 485–489, doi:10.1126/science.1067319.

Peng, X., and E. D. Humphreys (1997), Moho dip and crustal anisotropy in northwestern Nevada from teleseismic receiver functions, *Bulletin of the Seismological Society of America*, *87*(3), 745–754.

Peselnick, L., and A. Nicolas (1978), Seismic anisotropy in an ophiolite peridotite: application to oceanic upper mantle, *Journal of Geophysical Research: Solid Earth*, *83*(B3), 1227–1235.

Plafker, G., T. Hudson, T. Bruns, and M. Rubin (1978), Late Quaternary offsets along the Fairweather fault and crustal plate interactions in southern Alaska, *Canadian Journal of Earth Sciences*, *15*(5), 805–816, doi:10.1139/e78-085.

Powell, J., D. Schneider, D. Stockli, and K. Fallas (2016), Zircon (U-Th)/He thermochronology of Neoproterozoic strata from the Mackenzie Mountains, Canada: Implications for the Phanerozoic exhumation and deformation history of the northern Canadian Cordillera, *Tectonics*, *35*(3), 663–689, doi:10.1002/2015TC003989.

Powell, J. W., D. R. Issler, D. A. Schneider, K. M. Fallas, and D. F. Stockli (2019), Thermal history of the Mackenzie Plain, Northwest Territories, Canada: Insights from low-temperature thermochronology of the Devonian Imperial Formation, *GSA Bulletin*, *132*(3-4), 767–783, doi:10.1130/B35089.1.

Ranalli, G., and B. Fischer (1984), Diffusion creep, dislocation creep, and mantle rheology, *Physics of the Earth and Planetary Interiors*, *34*(1), 77 – 84, doi:https://doi.org/10.1016/0031-9201(84)90086-4.

Rasendra, N., M. Bonnin, S. Mazzotti, and C. Tiberi (2014), Crustal and Upper-Mantle Anisotropy Related to Fossilized Transpression Fabric along the Denali Fault, Northern Canadian Cordillera, *Bulletin of the Seismological Society of America*, *104*, 1964–1975, doi:10.1785/0120130233.

Roddick, J. A. (1967), Tintina Trench, *The Journal of Geology*, *75*(1), 23–33, doi:10.1086/627228.

Saltus, R. W. (2007), Matching magnetic trends and patterns across the Tintina fault, Alaska and Canada–evidence for offset of about 490 kilometers: Chapter C in Recent U.S. Geological Survey studies in the Tintina Gold Province, Alaska, United States, and Yukon, Canada–results of a 5-year project, *Tech. rep.*, Reston, VA, doi:10.3133/sir20075289C, report.

Sandvol, E., and T. Hearn (1994), Bootstrapping Shear-Wave Splitting Errors, *Bull. seism. Soc. Am.*, *84*.

Savage, M. K. (1999), Seismic anisotropy and mantle deformation: What have we learned from shear wave splitting?, *Reviews of Geophysics*, *37*(1), 65–106, doi:10.1029/98RG02075.

Savage, M. K., A. Wessel, N. A. Teanby, and A. W. Hurst (2010), Automatic measurement of shear wave splitting and applications to time varying anisotropy at Mount Ruapehu volcano, New Zealand, *Journal of Geophysical Research: Solid Earth*, *115*(B12), doi:10.1029/2010JB007722.

Schutt, D., E. Humphreys, and K. Dueker (1998), Anisotropy of the Yellowstone hot spot wake, eastern Snake River Plain, Idaho, *Pure and Applied Geophysics*, *151*, 443–462.

Sheaf, M. A., L. Serpa, and T. L. Pavlis (2003), Exhumation rates in the St. Elias Mountains, Alaska, *Tectonophysics*, *367*(1), 1 – 11, doi:https://doi.org/10.1016/S0040-1951(03)00124-0.

Silver, P. G., and W. W. Chan (1991), Shear wave splitting and subcontinental mantle deformation, *Journal of Geophysical Research: Solid Earth*, *96*(B10), 16,429–16,454, doi: 10.1029/91JB00899.

Skemer, P., and L. N. Hansen (2016), Inferring upper-mantle flow from seismic anisotropy: An experimental perspective, *Tectonophysics*, *668-669*, 1 – 14, doi:https://doi.org/10.1016/j.tecto.2015.12.003.

Smith, M. L., and F. A. Dahlen (1973), The azimuthal dependence of Love and Rayleigh wave propagation in a slightly anisotropic medium, *Journal of Geophysical Research (1896-1977)*, *78*(17), 3321–3333, doi:10.1029/JB078i017p03321.

Snyder, D., and M. Bruneton (2007), Seismic Anisotropy of the Slave craton, NW Canada, from joint interpretation of SKS and Rayleigh waves, *Geophysical Journal International*, *169*, 170–188.

Stein, S., and M. Wysession (2003), *An introduction to seismology, earthquakes, and earth structure*, John Wiley & Sons.

Tanimoto, T., and D. L. Anderson (1985), Lateral heterogeneity and azimuthal anisotropy of the upper mantle: Love and Rayleigh waves 100–250 s, *Journal of Geophysical Research: Solid Earth*, *90*(B2), 1842–1858, doi:10.1029/JB090iB02p01842.

Tarayoun, A., P. Audet, S. Mazzotti, and A. Ashoori (2017), Architecture of the crust and uppermost mantle in the northern Canadian Cordillera from receiver functions, *Journal of Geophysical Research: Solid Earth*, *122*(7), 5268–5287, doi:10.1002/2017JB014284.

Turcotte, D., and G. Schubert (2014), *Geodynamics*, Cambridge University Press.

Venereau, C., R. Martin-Short, I. Bastow, R. Allen, and R. Kounoudis (2019), The role of variable slab dip in driving mantle flow at the eastern edge of the Alaskan subduction margin: insights from SKS shear-wave splitting, *Geochemistry, Geophysics, Geosystems*, doi: 10.1029/2018GC008170.

Walsh, E., R. Arnold, and M. K. Savage (2013), Silver and Chan revisited, *Journal of Geophysical Research: Solid Earth*, *118*(10), 5500–5515, doi:https://doi.org/10.1002/jgrb.50386.

Wang, W., and T. W. Becker (2019), Upper mantle seismic anisotropy as a constraint for mantle flow and continental dynamics of the North American plate, *Earth and Planetary Science Letters*, *514*, 143 – 155, doi:https://doi.org/10.1016/j.epsl.2019.03.019.

Whittle, P. (1953), Estimation and information in stationary time series, *Ark. Mat.*, *2*(5), 423–434, doi:10.1007/BF02590998.

Wolfe, C. J., and P. G. Silver (1998), Seismic anisotropy of oceanic upper mantle: Shear wave splitting methodologies and observations, *Journal of Geophysical Research: Solid Earth*, *103*(B1), 749–771, doi:10.1029/97JB02023.

Wuestefeld, A., O. Al-Harrasi, J. P. Verdon, J. Wookey, and J. M. Kendall (2010), A strategy for automated analysis of passive microseismic data to image seismic anisotropy and fracture characteristics, *Geophysical Prospecting*, *58*(5), 755–773, doi:https://doi.org/10.1111/j.1365-2478.2010.00891.x.

Wüstefeld, A., G. Bokelmann, C. Zaroli, and G. Barruol (2008), SplitLab: A shear-wave splitting environment in Matlab, *Computers Geosciences*, *34*(5), 515 – 528, doi:https://doi.org/10.1016/j.cageo.2007.08.002.

Chapter 2

2.1 Introduction

The northern Canadian Cordillera (NCC) roughly extends from northern British Columbia through western Canada to the Beaufort Sea. The NCC is composed of a complexly deformed set of accreted terranes and miogeoclinal rocks formed off the western margin of the Laurentian craton (Figure 2.1) (*Nelson et al.*, 2013). Within our study region, the Tintina fault - a 530 km long fault with approximately 430-490 km of dextral displacement (*Gabrielse*, 1985; *Hayward*, 2015; *Roddick*, 1967; *Saltus*, 2007) - can be used to broadly separate terranes by their paleogeographic affinity. Terranes NE of Tintina are generally paraautochthonous miogeoclines and deformed by the Cordilleran orogen, terranes between the Tintina and Denali faults are pericratonic - accreted island arcs, accretionary complexes, and back-arc basins, on top of rifted North America basment (*Monger and Price*, 2002; *Nelson et al.*, 2013). To the west of the Denali fault are allochtonous exotic terranes (*Colpron and Nelson*, 2011).

Contemporary deformation in the NCC is created in part by the transpressional subduction of the Yakutat indentor beneath Alaska (*Hyndman et al.*, 2005). This transpression has resulted in uplift, shortening, and volcanism of the St. Elias and Chugach mountains, which lie to the southwest in the NCC, abutting the Gulf of Alaska (e.g. *Plafker et al.*, 1978; *Sheaf et al.*, 2003). Little ongoing deformation is observed in the central NCC, an area in which two large lithosphere-scale strike-slip faults, the Tintina fault (TF) and the Denali fault (DF), lie. These faults both show greater than 400 km of dextral offset (*Estève et al.*, 2020; *Leonard et al.*, 2008), but exhibit little seismicity today (*Hyndman et al.*, 2005; *Leonard et al.*, 2008).

The Mackenzie Mountains (MM) are a seismically active fold and thrust belt which is convex to the east and lies ~750 km northeast of the North America-Pacific plate margin, abutting the craton (Figure 2.2). These mountains are shortening at a rate of ~4 mm/yr, and moment tensors show thrust mechanisms with increasing proportions of strike-slip motion approaching the Richardson Mountains (*Hyndman et al.*, 2005). The source for the far-field stresses driving shortening is a

subject of debate. Hypotheses for this deformation include an orogenic float model (*Oldow et al.*, 1990) where deformation is induced by the Yakutat indentor (*Mazzotti and Hyndman*, 2002) or, alternatively, uplift from tractions along the base of the lithosphere (*Finzel et al.*, 2015).

The *Mazzotti and Hyndman* (2002) model of deformation suggests that strain is transferred inboard of the Yakutat indentor via a lower crustal detachment. This model requires a weak zone in the lower crust which creates a décollement, that transmits compressional stress northeast towards the craton. The craton, which is much stronger than the Cordillera (e.g. *Lewis et al.*, 2003), acts as a backstop for this strain transfer. Deformation is then accommodated along imbricated thrust faults in the MM, creating the uplift and deformation recorded in this region (*Mazzotti and Hyndman*, 2002).

An alternate hypothesis proposed by *Finzel et al.* (2015), suggests that the convergence seen in the MM is the result of asthenospheric flow creating convergent tractions along the base of the MM lithosphere. These tractions are suggested to result from large-scale mantle flow being deflected by the subduction of the Yakutat indentor beneath North America. This model is borne out of residuals between observations and models of surface velocity and strain rate, and does not require (or exclude) the lower crustal zone of weakness in the *Mazzotti and Hyndman* (2002) hypothesis. For instance, the lower crust could be weak to the SW of the MM allowing upper crustal movement to the NE, while the stronger lower crust under the MM could transmit basal tractions.

Contemporary uplift is not the first instance of uplift in the MM. Thermochronology studies suggest a first phase uplift occurring as early as the Late Cretaceous (*Enkelmann et al.*, 2019; *Powell et al.*, 2016, 2019), with another phase of cooling and uplift in the Paleocene-Eocene (*Enkelmann et al.*, 2019; *Powell et al.*, 2016). *Enkelmann et al.* (2019) further find strong evidence for uplift from approximately 33-20 Ma and infer 1-3 km of exhumation during this time. These episodes of deformation are generally related to the terrane accretion and deformation during the construction of the Cordillera; however, the 33-20 Ma uplift in *Enkelmann et al.* (2019) is inferred to result from the opening of the north Atlantic rift and subsequent plate reorganization. We note that these phases of uplift were distinguished by exhumation and subsequent cooling of sedimen-

tary formations, which is not observed in the contemporary uplift, suggesting that the modern phase is quite recent.

In this paper we investigate mantle dynamics - specifically anisotropic structure - within the NCC using anisotropy as a proxy for uppermost mantle fabrics. Shear wave splitting is a well-established technique for determining upper mantle anisotropy. Shear waves split into two quasi-S waves upon travel through an anisotropic medium, so long as the polarization direction of the incident wave is not parallel or perpendicular to the anisotropic alignment (e.g. *Menke and Levin*, 2003; *Silver and Chan*, 1991). Of these quasi-S waves, the "fast" wave travels at a higher velocity, and the other at a slower velocity. Shear wave splitting techniques typically characterize the anisotropy by the polarization of the fast wave - the fast-axis orientation, ϕ, and a delay time between the fast and slow arriving waves, δt. SKS waves are typically used in seismic anisotropy studies due to the lack of S_H energy and known radial polarization. Anisotropy in the upper mantle is generally thought to result from the alignment of olivine crystals; in the lithosphere anisotropy is generated from fossilized strain from the most recent tectonic events and in the asthenosphere this alignment is interpreted to be oriented in the direction of contemporary flow. *Audet et al.* (2016) compiles results from *Courtier et al.* (2010) and *Snyder and Bruneton* (2007) and adds new measurements to show a coherent NE-SW trend in anisotropy within the craton, subparallel to North American absolute plate motion (APM) (*Argus et al.*, 2010). However,the authors note a distinct change in the fast directions of anisotropy across the Liard Transfer Zone (LTZ) (Figure 2.2, black lines). The LTZ is a rifted margin that may be controlled by a sharp contrast between adjoining lithospheric fabric types (*Audet et al.*, 2016; *Tarayoun et al.*, 2017). Strong NW-SE alignment of fast axes is observed in the western Yukon, and large variations in splitting orientations are observed in the exotic terranes nearest the Yakutat indentor (*Hanna and Long*, 2012; *Venereau et al.*, 2019). *Estève et al.* (2020) adds splitting measurements from three regions: the northernmost portion of the NCC, about the Tintina fault, and to the northeast deep into the craton. Their results show a clear change in fast axis orientations between the Cordillera and the craton, where cratonic anisotropy is generally aligned NE-SW parallel to North American APM and Cordilleran anisotropy is much

more variable. Fast axes in the Cordillera are generally aligned with tectonic fabrics such as the Tintina and Denali faults, and the terrane boundaries within the NCC (Figure 2.1).

Relevant to the interpretation of any shear wave splitting is the observation that the Cordilleran mantle lithosphere is only ~20 km thick, based on a Moho depth of ~33 km (e.g. *Audet et al.*, 2019b; *Clowes et al.*, 2005; *Tarayoun et al.*, 2017) and a lithosphere-asthenosphere boundary at ~50 km depth (*Audet et al.*, 2019b; *Tarayoun et al.*, 2017). This contrasts with a 250 km thick cratonic lithosphere (*Frederiksen et al.*, 2001). Given that olivine fabrics in the upper mantle are the dominant source of seismic anisotropy observed using SKS splitting data (Figure 2.2, black), the contribution of a thin mantle lithosphere to the observed anisotropy measurements may be small. For a near-vertical ray path, one can estimate the thickness of an anisotropic layer given delay time, assumed percent anisotropy, and average shear velocity (e.g. *Schutt et al.*, 1998) using the relationship

$$L = V_{savg} * \frac{\delta t}{\%_{ani}}. \tag{2.1}$$

If we assume a 4% anisotropic upper mantle (*Savage*, 1999), and an average V_s of 4.5 km/s (ak135 upper mantle model of *Kennett et al.*, 1995), along with the delay times of ~1s that we see in this study region, we estimate an anisotropic layer thickness of about 110 km, which is much greater than the $<$ 20 km estimates of mantle lithospheric thickness in the region. Nevertheless, the stark change in fast axis orientations at the LTZ may indeed be due to a change in lithospheric fabric.

2.2 Data & Method

The MMEP network was deployed as a part of the National Science Foundation-funded Mackenzie Mountain Earthscope Project (MMEP) (*Baker et al.*, 2020). Station deployment began in August of 2015, and the final station retrieval occurred in August of 2019. These 41 seismographs were deployed along a roughly 875 km, approximately linear array extending from Fraser, British Columbia to Great Bear Lake in the Northwest Territories (*Baker et al.*, 2020). Stations are num-

bered sequentially from MM01 furthest to the SW in British Columbia to MM40 on the shore of the Great Bear Lake in Northwest Territories (*Baker et al.*, 2020). We analyzed signals from 44 events of magnitude > 5.8 and a signal-to-noise ratio >2.5 recorded between August 2015 and August 2019. We used SKS phases with angular distance ranges of 80-120°. Stations MM04 and MM06 were not oriented North and East - seismograms at these stations were rotated to this orientation. Data were detrended, demeaned, and resampled to 40 Hz. We used ak135 (*Kennett et al.*, 1995) to estimate SKS arrival time and excluded traces where another phase was predicted to arrive within 20 s of the SKS phase. We performed a visual inspection to eliminate seismograms with errors in the trace, or where the SKS signal was not clearly observed. Figure 2.3 shows the distribution of teleseismic events used in our study.

Data processing was performed using the SplitLab software package (*Wüstefeld et al.*, 2008). Some waveforms were left unfiltered, others were lowpass-filtered with a corner frequency of 0.4 Hz, and most of our waveforms were bandpass-filtered using corner frequencies of 0.01 Hz and either 0.4 or 0.5 Hz.; filter cutoffs were chosen manually depending on the visual characteristics of the waveform. SKS arrivals were manually windowed for at least one full period of the phase. We used both the rotation correlation (*Bowman and Ando*, 1987) and transverse energy minimization (*Silver and Chan*, 1991) methods to find best-fitting splitting parameters. We used these methods together to assign quality factors to each station-event pair based on signal-to-noise ratio within the window, and linearity of corrected particle motions. These quality designations are labeled "Poor" "Fair" and "Good", where higher qualities have higher signal-to-noise ratios (SNR), more linear particle motion, and good agreement between methods. SplitLab computes quality factors quantitatively using the relationship:

$$d_{null} = \sqrt{\Delta^2 + (\Omega - 1)^2}\sqrt{2}$$

$$d_{good} = \sqrt{(\Delta - 1)^2 + \Omega^2}\sqrt{2}$$

$$Q = \begin{cases} -(1 - d_{null}) & for\ d_{null} < d_{good} \\ (1 - d_{good}) & for\ d_{null} \geq d_{good} \end{cases} \tag{2.2}$$

where Δ is the ratio of delay times between the rotation-correlation and *Silver and Chan* (1991) methods, and Ω is the normalized difference in fast axes between these methods (*Wuestefeld et al.*, 2010). Q-values near 1 are typically considered "Good" measurements, while measurements near 0 are "Poor" and negative results signify null events. Many event-station pairs were culled based on disagreement between methods. We also characterized some arrivals as null measurements (Figure 2.4), and we used these results to verify the fast/slow axes determined for non-null measurements. Station-average results were created by stacking the misfit surfaces (e.g. *Schutt et al.*, 1998; *Wolfe and Silver*, 1998). This stacking relies solely on the transverse energy minimization error surface results (*Silver and Chan*, 1991) and does not utilize our rotation-correlation results, but it is likely a more robust estimate of the single-layer average than simple or weighted averages. Transverse energy error surface stacking allows one to utilize non-Gaussian error surfaces and the covariance between delay time and fast orientation uncertainties. We only included "Fair" or "Good" quality results in our average stacks to ensure high quality station-averages.

2.3 Results

Individual results for the MMEP stations are listed in Table A.1, and plotted against backazimuth modulo 180° in Figures A.1 - A.35. In these results we see little evidence for multiple layers of splitting - fast axis orientation does not clearly depend on backazimuth for any of these stations, motivating our look at station averages (Figure 2.2). Event backazimuthal coverage shows gaps from approximately 315° - 115°, and another gap between approximately 135° - 220° (Figure 2.3). The MMEP stations had on average 5 high quality events used to compute best-fitting station averages, and had a total of 180 station-event pairs. Individual station splitting results show a rotation in fast-axes across the MMEP array (Figure 2.5). The southwestern part of the array shows fast axes that generally align NW-SE, subparallel to the strike of the major tectonic fabrics and Pacific

APM (no net rotation) (*Argus et al.*, 2010). Within this region, stations MM02 and MM03 show strikes closer to a 330° azimuth and MM04-MM06 are oriented closer to 300°, though MM05 and MM06 show some splits oriented orthogonally to this general trend. Stations MM07-MM11 are located between the Teslin and Tintina faults; these stations also show general NW-SE trends and recorded more events than those SW of the Teslin. Northeast of the Tintina and southwest of the MM, individual splitting measurements show a gradual rotation in fast axes from NW-SE to NE-SW. The best fitting splitting parameters for stations located between the MM and Tintina are quite consistent with each other. Within the Mackenzie Mountains themselves, splits are not so consistent. We see large variations in fast axis orientations, and some minor variation in δt. These individual split results show rough trends -SW. The results within the undeformed craton show somewhat less scatter in splitting parameters and are oriented NE-SW.

Our station-average results (Figure 2.2, red; Table 2.1) show fast axes in the southwest that range from NW-SE to approximately E-W. Moving to the northeast, fast orientations stay relatively consistent across the Tintina fault. Northeast of the Tintina, station averages begin to show a rotation to NE-SW, similar to the direction of North American APM (*Argus et al.*, 2010). Splitting measurements northeast of the deformation front generally show alignment in this direction. We categorize the MMEP splitting measurements into three domains that show patterns of fast axis orientation along the strike of the array (Figures 2.2, 2.6). The furthest southwest group (green, Figures 2.2, 2.6), shows anisotropy oriented NW-SE, subparallel to the major faults and terrane boundaries in the NCC (Figure 2.1). The northeast group (violet) encompasses those measurements oriented NE-SW. The intervening group (yellow) demarks the transition between the two major fabric orientations.

Cratonic stations and those south of the LTZ show a general NE-SW alignment (violet circles, Figure 2.2. However, along the MMEP array as well as other measurements in the western portion of Figure 2.2 (blue circles), many of the averages show alignment with the terrane boundaries and major faults (Figure 2.1). To the southwest, fast axis orientations vary over shorter distances than elsewhere. Within the MM, splitting measurements are less consistent than in other areas. Near

the Teslin fault, large delay times are observed in the MMEP array stations, but very small times are observed to the SE along the fault (e.g. *Courtier et al.* (2010), near Watson Lake).

2.4 Discussion

SKS splitting measurements near and northeast of the deformation front are interpreted (Figures 2.2, 2.6 violet circles) as asthenospheric flow in the direction of APM (*Argus et al.*, 2010), echoing the interpretations of other anisotropy studies in this region (e.g. *Courtier et al.*, 2010; *Snyder and Bruneton*, 2007), although multiple lithospheric fabric layers may also exist here (e.g. *Snyder and Bruneton*, 2007). Despite variation in the splitting measurements within the MM - probably due to scattering off of topography or near-surface structure - these broadly align with APM. As one approaches the Tintina Fault from the NE, a rotation is observed over about 200 km, at which point the fast axes begin to match the strike of the fault.

While there is some significant crustal anisotropy aligned with the fault (*Rasendra et al.*, 2014), this is insufficient to create the observed ~1 s split times, and much of the anisotropy must reside below 50 km depth, in asthenospheric mantle. Additionally, the gradual transition suggest a deeper source (*Alsina and Snieder*, 1995). We suggest three possible causes for the rotation of fast axes from APM to fault strike (near the Pacific APM).

The first is that the dextral shear associated with the Tintina and Denali faults extends into the mantle lithosphere (*Estève et al.*, 2020) and splays out in the asthenosphere, perhaps as the result of a shear hardening process (e.g. *Karato*, 2013). A second possibility is that these fault-parallel orientations are the result of asthenospheric flow that is diverted by the subducting slab to the east, as modeled by *Finzel et al.* (2015). Their predicted asthenospheric tractions in this area match the fast axis orientations. Our third is that current and past subduction of the Pacific plate has caused asthenospheric flow in the direction of subduction. The model of *Wang and Becker* (2019), while based on global tomography, and therefore being somewhat low resolution, shows that near the subduction zone asthenospheric flow is aligned with subduction throughout the upper ~200 km of the mantle (Figure 2.8). Then as one moves to the NE, such as along the strike of the MMEP

array, the uppermost part of the asthenosphere starts to show flow along APM, and the portion of the asthenosphere that flows along APM increases with distance away from the subduction zone. Hence, in Figure 2.6 the "subduction-related" regime is showing subduction-induced flow, the "transition" is where an increasing wedge of the uppermost asthenosphere is flowing along APM, and the APM zone is where the whole asthenosphere is flowing in the direction of APM. We note that this would imply two layer splitting in the transition (MM17 - MM27), and while we see no conclusive evidence for this we cannot rule it out.

The ~220 km wide "transition" in Figure 2.6 may offer some clues to the process producing the rotation. This transition is too wide to be produced from the Fresnel zone of two regimes of fast axis orientation that bound each other (*Alsina and Snieder*, 1995). It could be due to a graduate rotation between two regimes, or due to a depth-dependant flow field. We do not favor shear associated with the large dextral faults as a possibility, because the lithosphere here is quite thin, and it seems implausible that ~90 km of asthenosphere are sheared. This leaves either the flow field associated with basal tractions (*Finzel et al.*, 2015), or that associated with subduction-induced flow (*Wang and Becker*, 2019). Differentiating between the two models is difficult, as the *Finzel et al.* (2015) model does not extend beyond the MM, and the *Wang and Becker* (2019) model is based on global tomography, and thus is missing many of the local tomographic (and thus density) nuances. However, based on the current evidence, the shear wave splits seem to match the *Wang and Becker* (2019) depth-dependant flow field better.

Furthest to the southwest, inconsistency within shear wave splits may result from the complex mantle flow and highly imbricated lithosphere associated with the subduction of the Yakutat indentor beneath North America (Figure 2.6; green).

Shear wave splitting measurements may further provide insight into the discussion of contemporary MM uplift. If the orogenic float hypothesis (*Mazzotti and Hyndman*, 2002) proves true, then crustal anisotropy would be decoupled from underlying mantle anisotropy (e.g. *Hyndman et al.*, 2005; *Mazzotti and Hyndman*, 2002). Conversely, the mantle traction model of uplift (*Finzel et al.*, 2015) predicts that these fabrics would be coupled, and splitting results would be aligned with their

predicted tractions. Our results show general agreement with predicted tractions (Figure 2.9), but the source of the anisotropy is unclear. The shear wave splitting results seem to be the result of subduction in the southwest, but whether this fabric was created from the more-recent subduction of the Yakutat microplate beneath Alaska or from longer-lived subduction of the Pacific plate is unclear. Of the models discussed above, only the shear hardening model requires crust-mantle coupling that would effectively rule out the orogenic float.

2.5 Conclusions

We present new results for shear wave splitting across the MM using the new MMEP seismograph network. Our results, coupled with previous splitting studies, show a net rotation of anisotropic fast axis orientations across this study region. Nearest to and inboard of the Cordilleran deformation front, fast axes are generally aligned with North American APM and are inferred to result from asthenosphere flow in this direction. As distance from the plate margin decreases, fast axes rotate to be subparallel to large-scale lithospheric fabrics, though we do not interpret splits to represent lithospheric anisotropy. Instead we note that both lithospheric fabric (such as the strike of the Denali and Tintina faults) and asthenospheric flow are both modulated by subduction. The flow pattern producing the observed splits may be either an asthenospheric shear zone splaying off below the large dextral faults, southward flow under Alaska that is redirected by the slab (*Finzel et al.* (2015)), or depth variable flow induced by the subducting plate (*Wang and Becker* (2019)). We currently favor the depth variable flow model, but new geodesy data and new studies that update the (*Finzel et al.* (2015)) tractions may produce distinctive testable hypotheses.

2.6 Figures

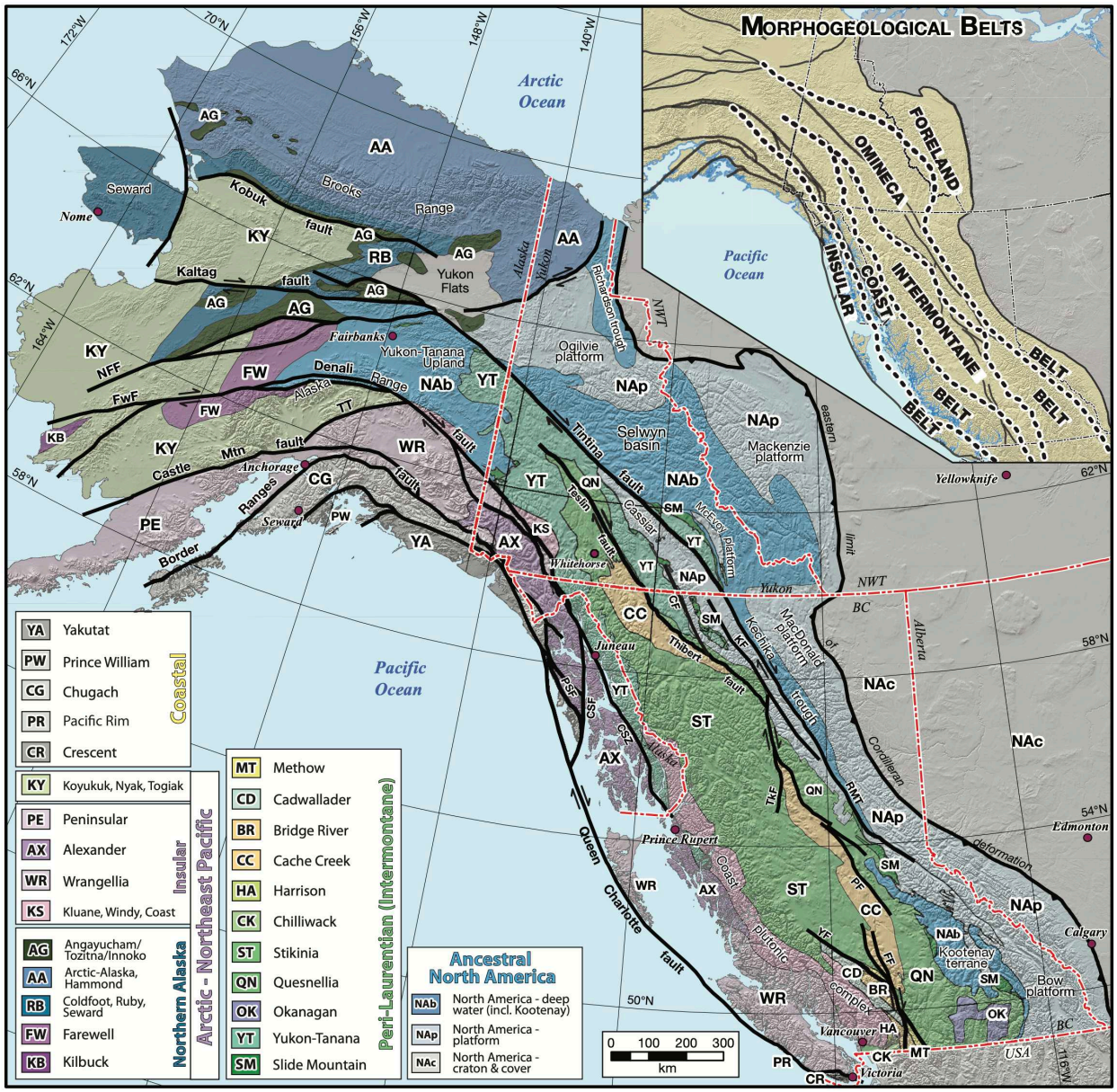

Figure 2.1: Terrane map of the NCC and Alaska, colored by terrane heritage. After *Nelson et al.* (2013).

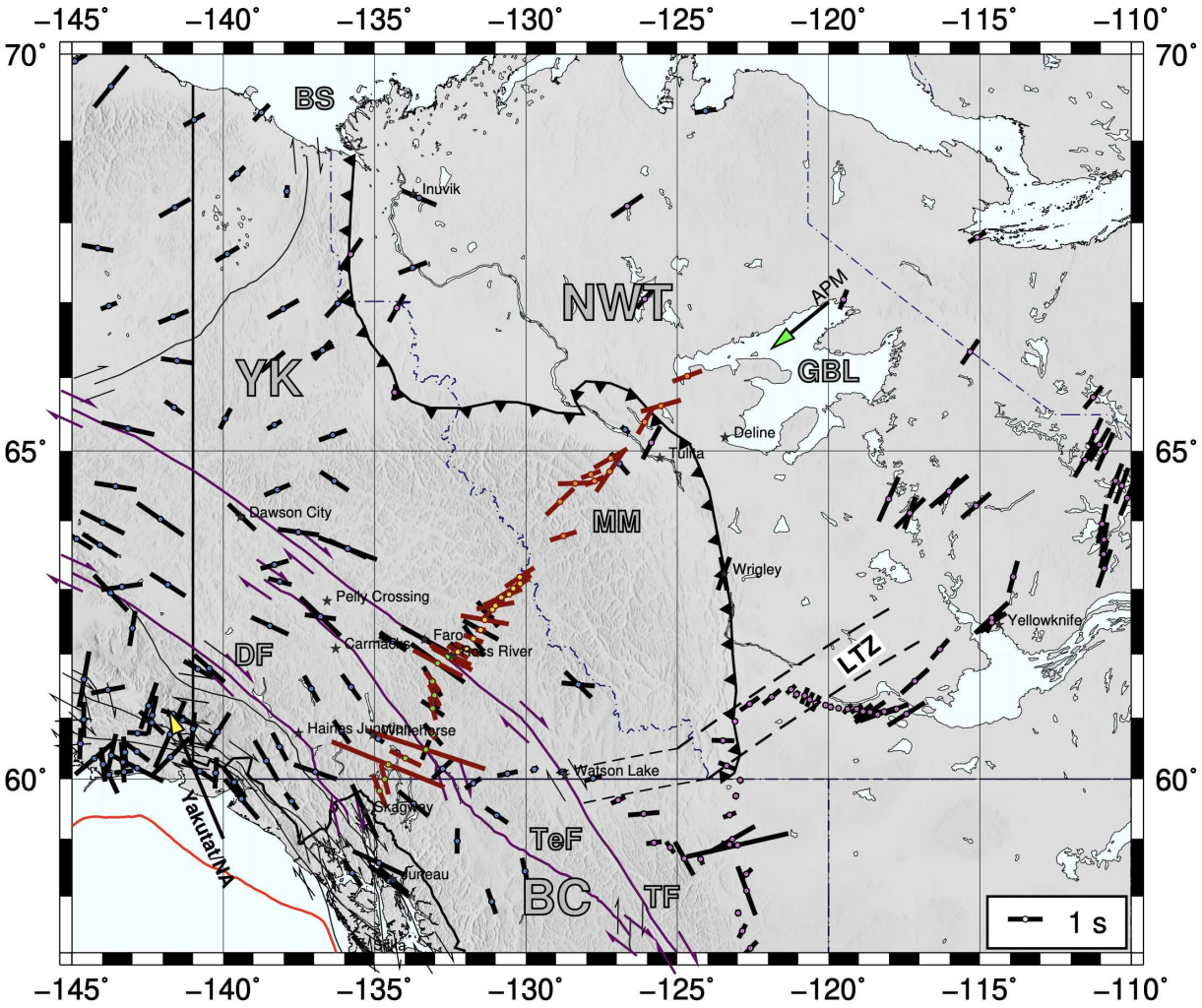

Figure 2.2: Compilation of shear wave splits within our study area. Shear wave splitting measurements shown as colored lines above the station in which they are averaged. Station-averaged fast axis orientation is the orientation of the lines, and length is proportional to the delay time. Red lines denote measurements introduced in this study, Colors along the MMEP array denote perceived mantle fabric affinity noted in Figure 2.6. Splitting measurements from other studies are shown as black lines with violet or blue circles, denoting the general affinity of the split (blue circles denote splits aligned with the major tectonic fabrics, violet circles are aligned with North American APM (*Argus et al.*, 2010)). Yakutat subduction direction shown as yellow arrow, North American absolute plate motion shown as green arrow. Solid black line denotes the eastern limit of deformation between Canadian Cordillera and craton. Major faults show in purple, minor faults are dark gray. Dashed line is the extent of the Liard Transfer Zone. YK=Yukon, NWT=Northwest Territories, BC=British Columbia, BS=Beaufort Sea, GBL=Great Bear Lake, LTZ=Liard Transfer Zone. Previous splitting measurements after *Audet et al.* (2016); *Courtier et al.* (2010); *Estève et al.* (2020); *Snyder and Bruneton* (2007); *Venereau et al.* (2019).

Figure 2.3: Event distribution of SKS phases used in this study.

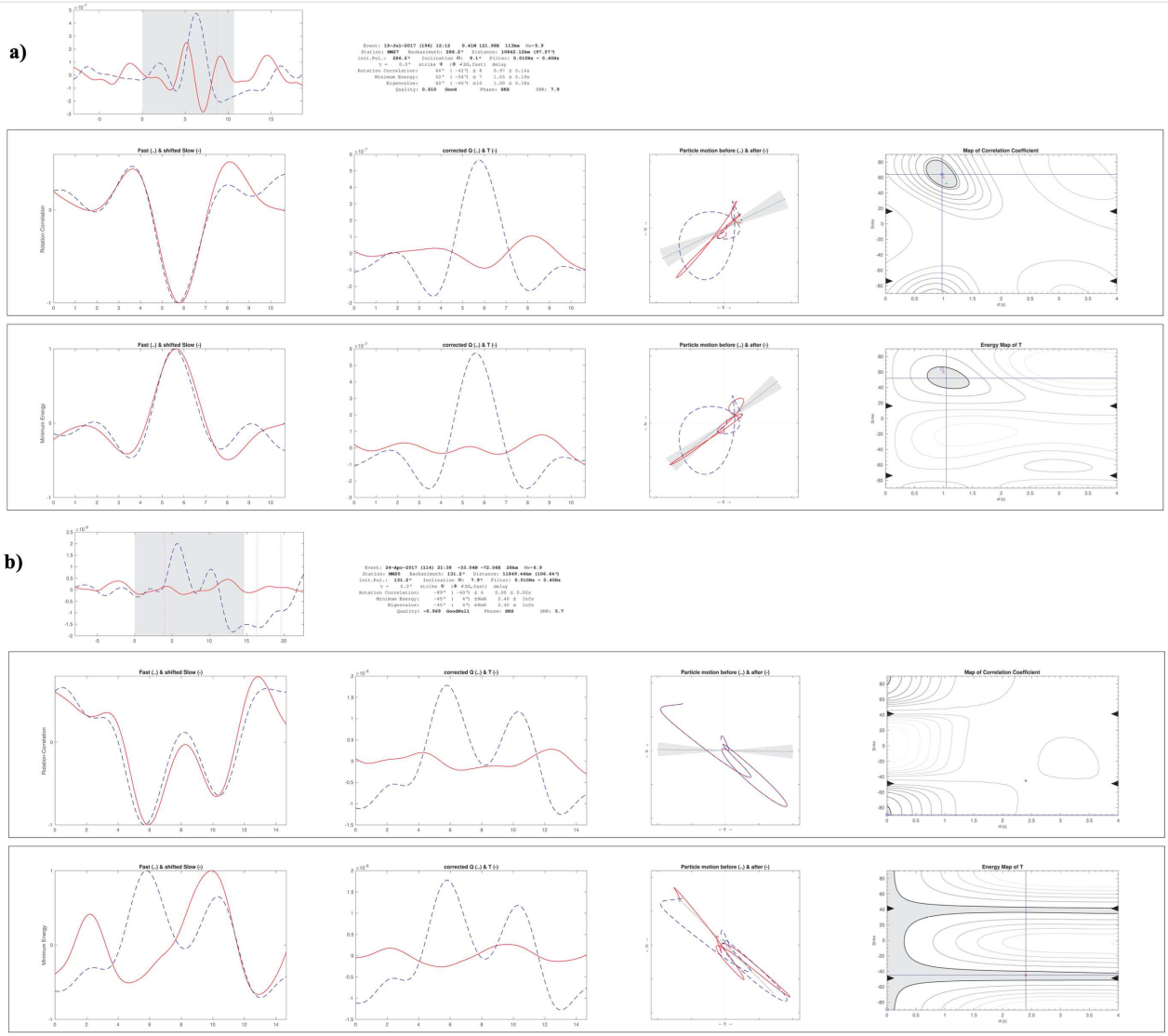

Figure 2.4: Example results for a 'good' quality (a) and null event (b).

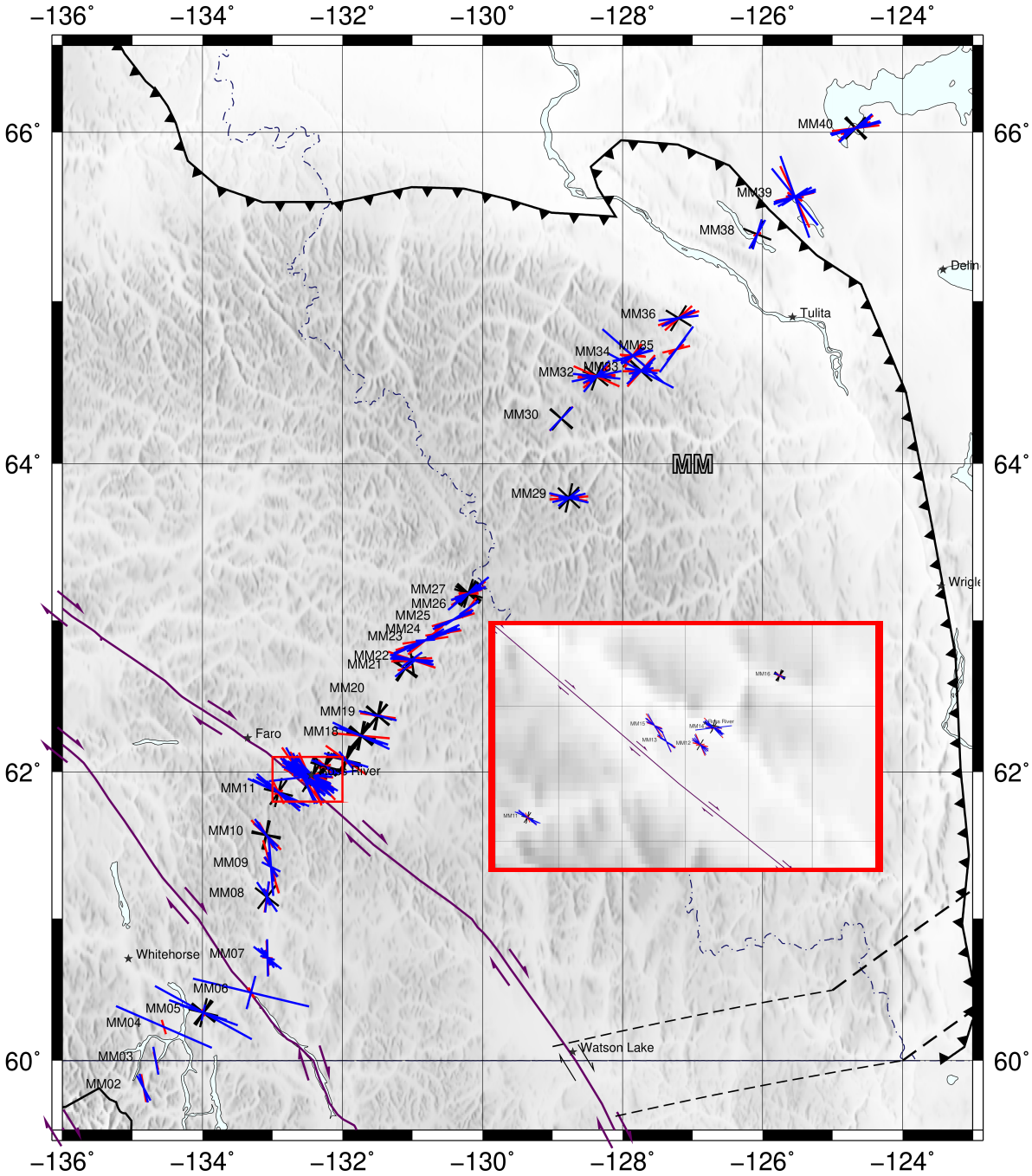

Figure 2.5: Individual event best-fitting splitting parameters at each MMEP station. Sticks are oriented parallel to the determined fast axis direction, and the length of the stick is proportional to the delay time. Red sticks show the rotation correlation (*Bowman and Ando*, 1987) method, blue sticks show the transverse energy minimization (*Silver and Chan*, 1991) method. Null backazimuths are plotted as crosses beneath the splitting measurements. Inset provides a better view of the stations situated about Ross River, NE of the Tintina fault.

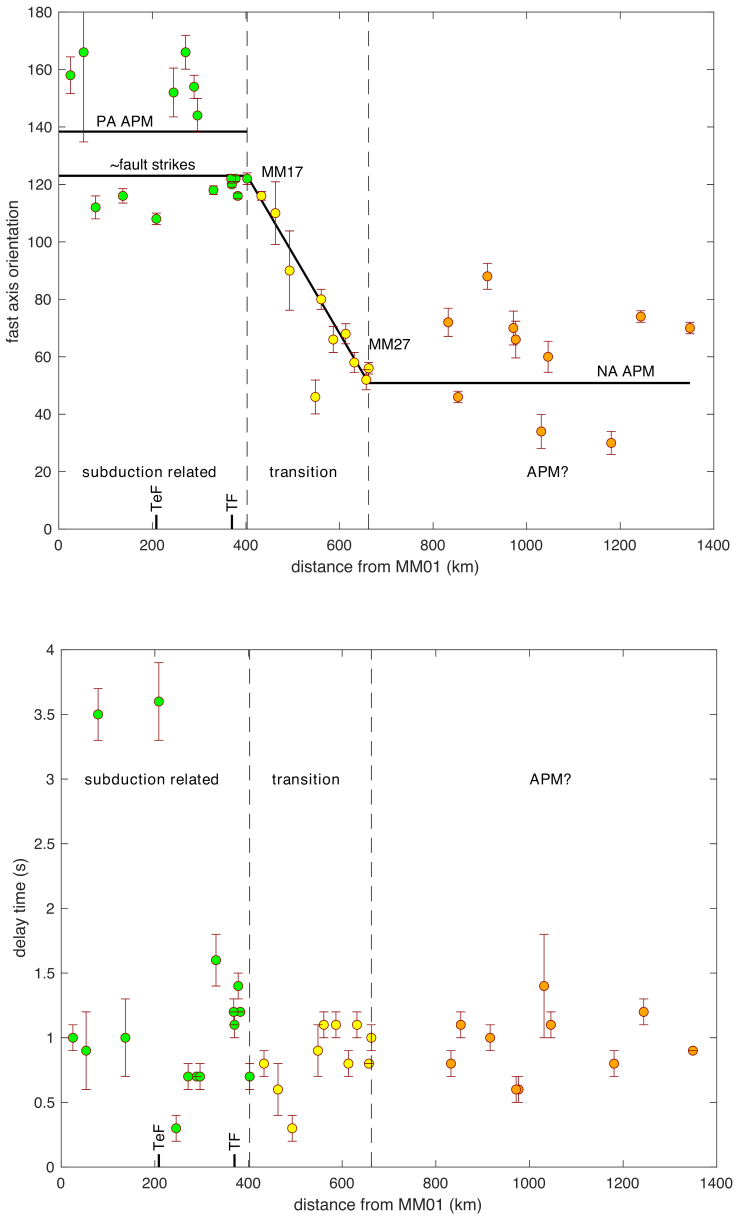

Figure 2.6: (Top) Fast axis orientation of station-averaged results against distance from MM01 (furthest southwest station). We categorize splitting averages into three fabric affinities: those aligned ~parallel to major faults (green), those aligned ~parallel to NA absolute plate motion (orange), and the rotation between those two fabrics (yellow). Note the highly linear nature of the yellow mantle fabrics. (Bottom) Average delay time of against distance from MM01. The delay times in this study are lie around 1 s (with the exception of MM04 and MM06, which have few recorded events) and do not have an obvious relationship with distance. Uncertainties were constructed using the 95% confidence intervals in the ϕ and δt measurements as expressed in *Silver and Chan* (1991).

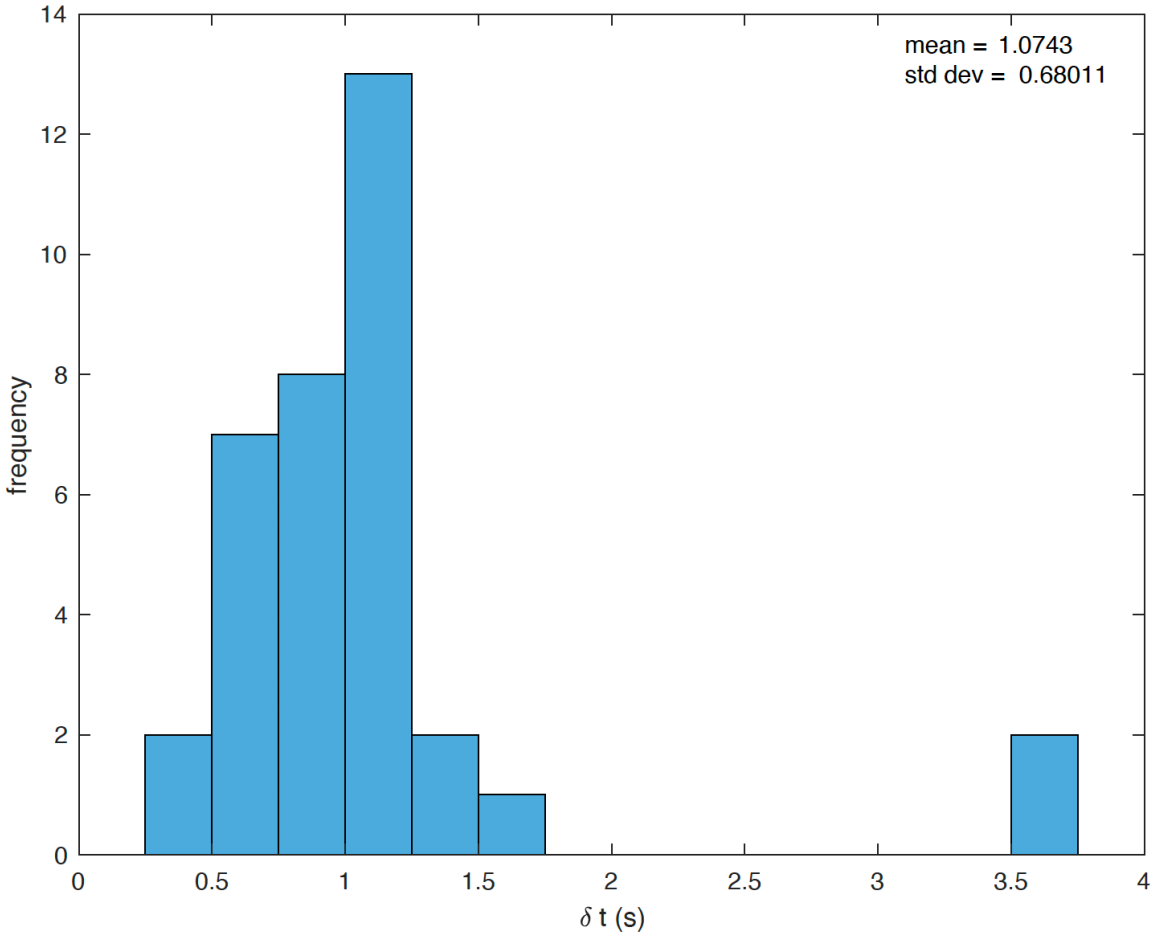

Figure 2.7: Histogram of station-average delay times along the MMEP network, binned at 0.25 s intervals. Mean delay times are greater than 1 s with a large standard deviation. Two splitting results (MM04 and MM06) give anomalously large delay times, and those stations have only few recorded events used in this study (Table A.1).

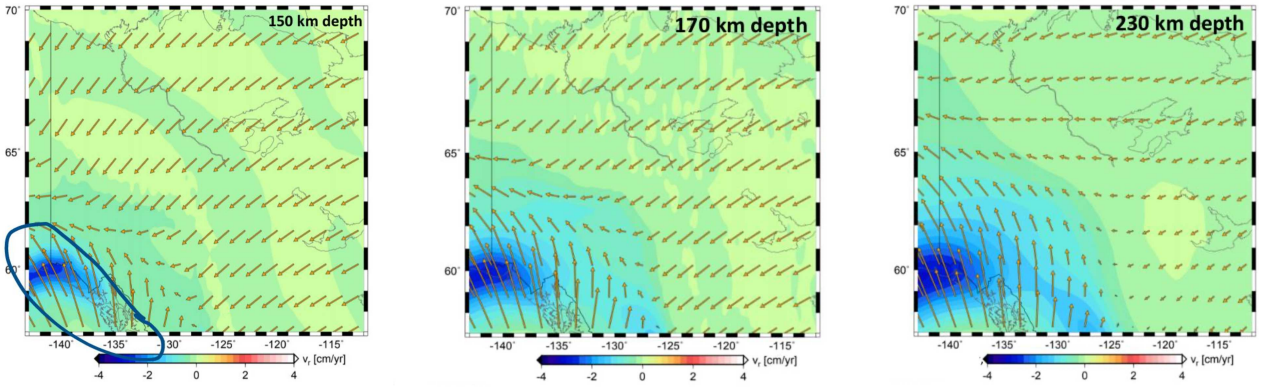

Figure 2.8: Modeled asthenospheric flow patterns beneath the NCC at depths of 150, 170, and 230 km. Blue circle denotes the perceived extent of the Yakutat slab on the 150 km depth slice. Note that modeled flow paths tend to align with NA-APM (NE-SW) but are diverted about the slab as depth increases. Data from (*Wang and Becker*, 2019), figure after Wanying Wang, pers. comm.

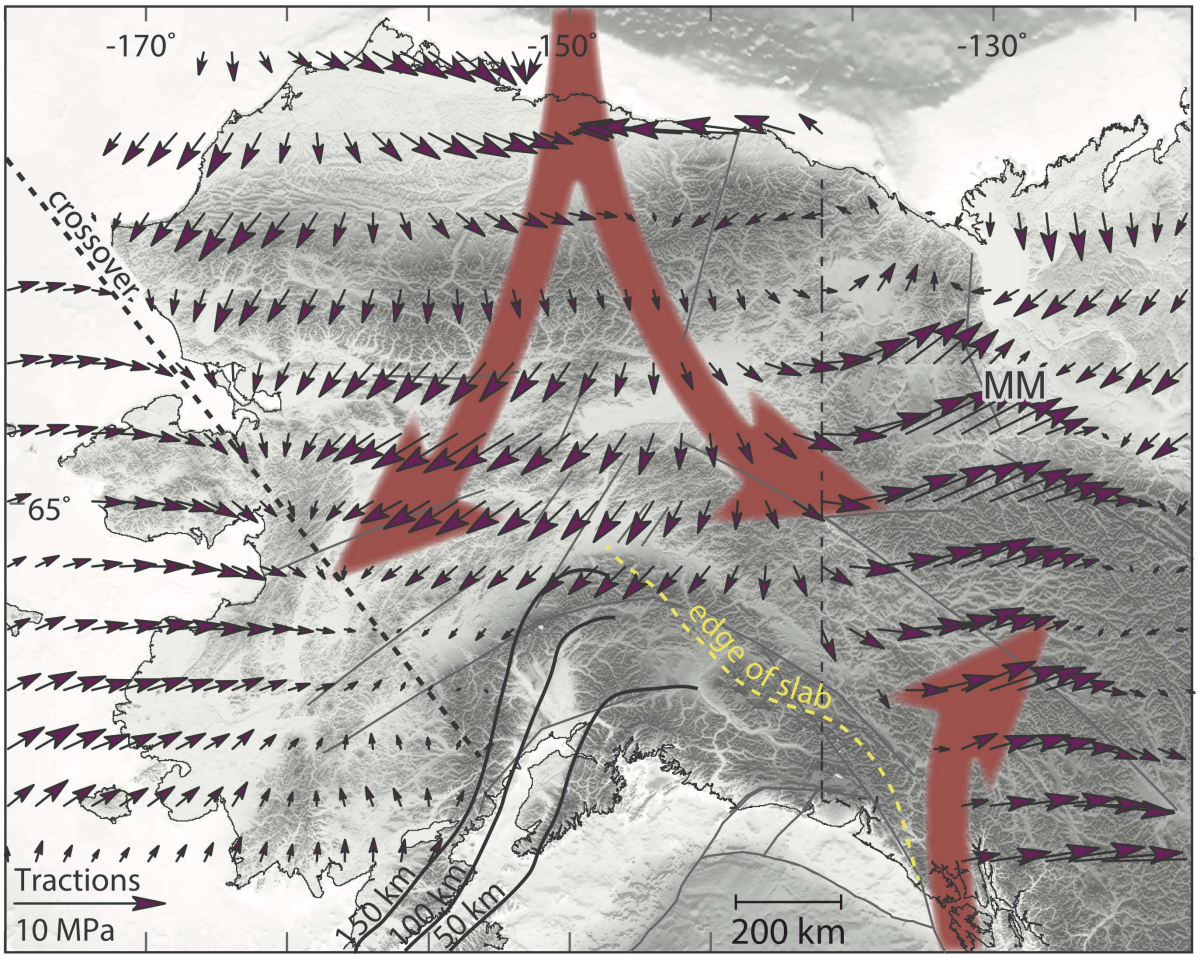

Figure 2.9: Modeled tractions inferred to be created by asthenosphere flow in *Finzel et al.* (2015). To the furthest east, the NCC can be seen. The large-scale flow thought to create these tractions could explain the change in anisotropy seen in our results.

2.7 Tables

Table 2.1: Station-average results for the MMEP shear wave splitting measurements taken in this study.

Station Name	Longitude (°)	Latitude (°)	fast axis (°)	σ_{fast}	delay time (s)	$\sigma_{\delta t}$
MM01	-135.051	59.7153	-22.0	6.4	1.0	0.1
MM02	-134.8387	59.8029	-14.0	31.2	0.9	0.3
MM03	-134.6654	59.9992	-68.0	4.0	3.5	0.2
MM04	-134.5509	60.24	-64.0	2.5	1.0	0.3
MM05	-133.9864	60.3412	-72.0	2.0	3.6	0.3
MM06	-133.306	60.4834	-28.0	8.5	0.3	0.1
MM07	-133.0708	60.7272	-14.0	5.9	0.7	0.1
MM08	-133.0788	61.1496	-26.0	4.0	0.7	0.0
MM09	-133.021	61.3568	-36.0	5.9	0.7	0.1
MM10	-133.0906	61.5744	-62.0	1.5	1.6	0.2
MM11	-132.9147	61.8624	-58.0	1.0	1.4	0.1
MM12	-132.4607	61.9525	-60.0	1.0	1.1	0.1
MM13	-132.5498	61.9564	-64.0	1.0	1.2	0.0
MM14	-132.4257	61.9733	-58.0	1.5	1.2	0.1
MM15	-132.5815	61.9764	-58.0	2.0	0.7	0.1
MM16	-132.2521	62.0378	-64.0	1.5	0.8	0.1
MM17	-131.9483	62.0789	-70.0	10.9	0.6	0.2
MM18	-131.734	62.2424	-90.0	13.8	0.3	0.1
MM19	-131.4946	62.3754	-80.0	3.0	1.4	0.4
MM21	-131.1073	62.6859	46.0	5.9	0.9	0.2
MM22	-131.0108	62.744	80.0	3.5	1.1	0.1
MM23	-130.8161	62.8713	66.0	4.5	1.1	0.1
MM24	-130.5585	62.9184	68.0	3.5	0.8	0.1
MM25	-130.419	63.0049	58.0	3.5	1.1	0.1
MM26	-130.1928	63.081	52.0	3.5	0.8	0.0
MM27	-130.2005	63.1749	56.0	2.0	1.0	0.1
MM29	-128.7663	63.7846	72.0	4.9	0.8	0.1
MM30	-128.8747	64.2803	46.0	2.0	1.1	0.1
MM32	-128.3708	64.5422	88.0	4.5	1.0	0.1
MM33	-127.7338	64.5754	66.0	6.4	0.6	0.1
MM34	-127.8535	64.6682	70.0	5.9	0.6	0.1
MM35	-127.2314	64.7072	34.0	5.9	1.4	0.4
MM36	-127.201	64.8969	60.0	5.4	1.1	0.1
MM38	-126.0765	65.4005	30.0	4.0	0.8	0.1
MM39	-125.5396	65.6226	74.0	2.0	1.2	0.1
MM40	-124.6709	66.0246	70.0	2.0	0.9	0.0

Bibliography

Alsina, D., and R. Snieder (1995), Small-scale sublithospheric continental mantle deformation: constraints from SKS splitting observations, *Geophysical Journal International*, *123*(2), 431–448, doi:10.1111/j.1365-246X.1995.tb06864.x.

Argus, D. F., R. G. Gordon, M. B. Heflin, C. Ma, R. J. Eanes, P. Willis, W. R. Peltier, and S. E. Owen (2010), The angular velocities of the plates and the velocity of Earth's centre from space geodesy, *Geophysical Journal International*, *180*(3), 913–960, doi:10.1111/j.1365-246X.2009.04463.x.

Audet, P., C. Sole, and A. J. Schaeffer (2016), Control of lithospheric inheritance on neotectonic activity in northwestern Canada?, *Geology*, *44*(10), 807–810.

Audet, P., C. J. Thomson, M. G. Bostock, and T. Eulenfeld (2019a), Telewavesim: Python software for teleseismic body wave modeling, doi:10.5281/zenodo.3551258.

Audet, P., C. A. Currie, A. J. Schaeffer, and A. M. Hill (2019b), Seismic Evidence for Lithospheric Thinning and Heat in the northern Canadian Cordillera, *Geophysical Research Letters*, *46*(8), 4249–4257, doi:10.1029/2019GL082406.

Baker, M. G., D. C. Heath, D. L. Schutt, R. C. Aster, J. F. Cubley, and J. T. Freymueller (2020), The Mackenzie Mountains EarthScope Project: Studying Active Deformation in the Northern North American Cordillera from Margin to Craton, *Seismological Research Letters*, *91*(1), 521–532, doi:10.1785/0220190139.

Ben-Ismail, W., and D. Mainprice (1998), An olivine fabric database: an overview of upper mantle fabrics and seismic anisotropy, *Tectonophysics*, *296*, 145–157.

Bernard, R. E., W. M. Behr, T. W. Becker, and D. J. Young (2019), Relationships Between Olivine CPO and Deformation Parameters in Naturally Deformed Rocks and Implications for Mantle

Seismic Anisotropy, *Geochemistry, Geophysics, Geosystems*, *20*(7), 3469–3494, doi:10.1029/2019GC008289.

Bowman, J. R., and M. Ando (1987), Shear-wave splitting in the upper-mantle wedge above the Tonga subduction zone, *Geophysical Journal International*, *88*(1), 25–41, doi:10.1111/j.1365-246X.1987.tb01367.x.

Clowes, R., P. Hammer, G. Fernandez-Viejo, and K. Welford (2005), Lithospheric structure in northwestern Canada from LITHOPROBE seismic refraction and related studies: a synthesis, *Canadian Journal of Earth Sciences*, *42*, 1277–1293, doi:10.1139/e04-069.

Colpron, M., and J. L. Nelson (2011), A digital atlas of terranes for the northern Cordillera, *Yukon Geological Survey*.

Corbalán, A. (2016), A new method to test shear wave splitting: improving statistical assessment of splitting parameters.

Corbalán, A., F. Breidt, D. Witt, and D. Schutt (in revision), Whittle Likelihood Estimation of Shear-wave Splitting Parameters in the Presence of Highly-Corrleted Microseismic Noise.

Cordier, P., T. Ungár, L. Zsoldos, and G. Tichy (2004), Dislocation creep in MgSiO3 perovskite at conditions of the Earth's uppermost lower mantle, *Nature*, *428*, 837–40, doi:10.1038/nature02472.

Courtier, A., J. Gaherty, J. Revenaugh, M. Bostock, and E. Garnero (2010), Seismic anisotropy associated with continental lithosphere accretion beneath the CANOE array, Northwestern Canada, *Geology*, *38*(10), 887–890, doi:10.1130/G31120.1.

Crampin, S. (1981), A review of wave motion in anisotropic and cracked elastic-media, *Wave motion*, *3*(4), 343–391.

Crampin, S. (1984), An introduction to wave propagation in anisotropic media, *Geophysical Journal of the Royal Astronomical Society*, *76*(1), 17–28, doi:10.1111/j.1365-246X.1984.tb05018.x.

Crotwell, H. P., T. J. Owens, and J. Ritsema (1999), The TauP Toolkit: Flexible Seismic Travel-time and Ray-path Utilities, *Seismological Research Letters*, *70*(2), 154–160, doi:10.1785/gssrl.70.2.154.

Debayle, E., and M. Sambridge (2004), Inversion of massive surface wave data sets: Model construction and resolution assessment, *Journal of Geophysical Research: Solid Earth*, *109*(B2), doi:10.1029/2003JB002652.

Eddy, C. L., G. Ekström, M. Nettles, and J. B. Gaherty (2018), Age dependence and anisotropy of surface-wave phase velocities in the Pacific, *Geophysical Journal International*, *216*(1), 640–658, doi:10.1093/gji/ggy438.

Eken, T., and F. Tilmann (2014), The Use of Direct Shear Waves in Quantifying Seismic Anisotropy: Exploiting Regional Arrays, *Bulletin of the Seismological Society of America*, *104*, 2644–2661, doi:10.1785/0120140020.

Enkelmann, E., E. Finzel, and J. Arkle (2019), Deformation at the eastern margin of the Northern Canadian Cordillera: Potentially related to opening of the North Atlantic, *Terra Nova*, *31*(3), 151–158, doi:10.1111/ter.12374.

Estève, C., P. Audet, A. J. Schaeffer, D. L. Schutt, R. C. Aster, and J. F. Cubley (2020), Seismic evidence for craton chiseling and displacement of lithospheric mantle by the Tintina fault in the northern Canadian Cordillera, *Geology*, doi:10.1130/G47688.1.

Finzel, E. S., L. M. Flesch, K. D. Ridgway, W. E. Holt, and A. Ghosh (2015), Surface motions and intraplate continental deformation in Alaska driven by mantle flow, *Geophysical Research Letters*, *42*(11), 4350–4358, doi:10.1002/2015GL063987.

Frederiksen, A., M. Bostock, and J. Cassidy (2001), S-wave velocity structure of the Canadian upper mantle, *Physics of the Earth and Planetary Interiors*, *124*(3), 175 – 191, doi:https://doi.org/10.1016/S0031-9201(01)00194-7.

Frost, D. J. (2008), The upper mantle and transition zone, *Elements*, *4*(3), 171–176.

Gabrielse, H. (1985), Major dextral transcurrent displacements along the Northern Rocky Mountain Trench and related lineaments in north-central British Columbia, *GSA Bulletin*, *96*(1), 1–14, doi:10.1130/0016-7606(1985)96<1:MDTDAT>2.0.CO;2.

Green II, H. W., and S. V. Radcliffe (1972), *Deformation Processes in the Upper Mantle*, pp. 139–156, American Geophysical Union (AGU), doi:10.1029/GM016p0139.

Gueguen, Y. (1977), Dislocations in mantle peridotite nodules, *Tectonophysics*, *39*(1), 231 – 254, doi:https://doi.org/10.1016/0040-1951(77)90098-1, fabrics, microstructures, and microtectonics.

Hanna, J., and M. D. Long (2012), SKS splitting beneath Alaska: Regional variability and implications for subduction processes at a slab edge.

Hayward, N. (2015), Geophysical investigation and reconstruction of lithospheric structure and its control on geology, structure, and mineralization in the Cordillera of northern Canada and eastern Alaska, *Tectonics*, *34*(10), 2165–2189, doi:https://doi.org/10.1002/2015TC003871.

Hess, H. (1964), Seismic anisotropy of the uppermost mantle under oceans, *Nature*, *203*(4945), 629.

Hyndman, R., P. Flueck, S. Mazzotti, T. J Lewis, J. Ristau, and L. Leonard (2005), Current tectonics of the northern Canadian Cordillera, *Canadian Journal of Earth Sciences*, *42*, 1117–1136, doi:10.1139/e05-023.

Jin, Z.-M., H. Green, and R. Borch (1989), Microstructures of olivine and stresses in the upper mantle beneath Eastern China, *Tectonophysics*, *169*(1), 23 – 50, doi:https://doi.org/10.1016/0040-1951(89)90181-9.

Karato, S., and P. Wu (1993), Rheology of the Upper Mantle: A Synthesis, *Science*, *260*(5109), 771–778.

Karato, S., S. Zhang, and H.-R. Wenk (1995), Superplasticity in Earth's Lower Mantle: Evidence from Seismic Anisotropy and Rock Physics, *Science*, *270*(5235), 458–461.

Karato, S.-I. (2013), *Rheological Properties of Minerals and Rocks*, chap. 4, pp. 94–144, John Wiley Sons, Ltd, doi:https://doi.org/10.1002/9781118529492.ch4.

Karato, S.-i., H. Jung, I. Katayama, and P. Skemer (2008), Geodynamic Significance of Seismic Anisotropy of the Upper Mantle: New Insights from Laboratory Studies, *Annu. Rev. Earth Planet. Sci.*, *36*, 59–95, doi:10.1146/annurev.earth.36.031207.124120.

Kendall, M. (2007), *D´´, Anisotropy*, pp. 146–149, Springer Netherlands, Dordrecht, doi:10.1007/978-1-4020-4423-6_61.

Kennett, B. L. N., E. R. Engdahl, and R. Buland (1995), Constraints on seismic velocities in the Earth from traveltimes, *Geophysical Journal International*, *122*(1), 108–124, doi:10.1111/j.1365-246X.1995.tb03540.x.

Langston, C. A. (1977), The effect of planar dipping structure on source and receiver responses for constant ray parameter, *Bulletin of the Seismological Society of America*, *67*(4), 1029–1050.

Leonard, L. J., S. Mazzotti, and R. D. Hyndman (2008), Deformation rates estimated from earthquakes in the northern Cordillera of Canada and eastern Alaska, *Journal of Geophysical Research: Solid Earth*, *113*(B8), doi:10.1029/2007JB005456.

Lev, E. (2009), Elastic and viscous anisotropy in Earth's mantle - observations and implications, Ph.D. thesis, Massachusetts Institute of Technology.

Lewis, T. J., R. D. Hyndman, and P. Flück (2003), Heat flow, heat generation, and crustal temperatures in the northern Canadian Cordillera: Thermal control of tectonics, *Journal of Geophysical Research: Solid Earth*, *108*(B6), doi:https://doi.org/10.1029/2002JB002090.

Long, M. D., and P. G. Silver (2009), Shear Wave Splitting and Mantle Anisotropy: Measurements, Interpretations, and New Directions, *Surveys in Geophysics*, *30*(4), 407–461, doi: 10.1007/s10712-009-9075-1.

Mazzotti, S., and R. Hyndman (2002), Yakutat collision and strain transfer across the northern Canadian Cordillera, *Geology*, *30*, doi:10.1130/0091-7613(2002)030<0495:YCASTA>2.0.CO; 2.

McNamara, D. E., and T. J. Owens (1993), Azimuthal shear wave velocity anisotropy in the Basin and Range Province using moho Ps converted phases, *Journal of Geophysical Research: Solid Earth*, *98*(B7), 12,003–12,017, doi:10.1029/93JB00711.

Menke, W., and V. Levin (2003), The cross-convolution method for interpreting SKS splitting observations, with application to one and two-layer anisotropic earth models, *Geophysical Journal International*, *154*(2), 379–392, doi:10.1046/j.1365-246X.2003.01937.x.

Mizukami, T., S. R. Wallis, and J. Yamamoto (2004), Natural examples of olivine lattice preferred orientation patterns with a flow-normal a-axis maximum, *Nature*, *427*(6973), 432–436.

Monger, J., and R. Price (2002), The Canadian Cordillera: Geology and Tectonic Evolution, *CSEG Recorder*, p. 17.

Montagner, J.-P., and T. Tanimoto (1991), Global upper mantle tomography of seismic velocities and anisotropies, *Journal of Geophysical Research: Solid Earth*, *96*(B12), 20,337–20,351, doi: 10.1029/91JB01890.

Nelson, J. L., M. Colpron, and S. Israel (2013), The Cordillera of British Columbia, Yukon, and Alaska: Tectonics and Metallogeny, in *Tectonics, Metallogeny, and Discovery: The North American Cordillera and Similar Accretionary Settings*, Society of Economic Geologists, doi: 10.5382/SP.17.03.

Oldow, J. S., A. W. Bally, and H. G. Ave Lallemant (1990), Transpression, orogenic float, and lithospheric balance, *Geology*, *18*(10), 991–994, doi:10.1130/0091-7613(1990)018<0991:TOFALB>2.3.CO;2.

Owens, T. J., H. P. Crotwell, C. Groves, and P. Oliver-Paul (2004), SOD: Standing order for data, *Seismological Research Letters - SEISMOL RES LETT*, *75*, 515–520, doi:10.1785/gssrl.75.4.515-a.

Park, J., and V. Levin (2002), Seismic Anisotropy: Tracing Plate Dynamics in the Mantle, *Science*, *296*(5567), 485–489, doi:10.1126/science.1067319.

Peng, X., and E. D. Humphreys (1997), Moho dip and crustal anisotropy in northwestern Nevada from teleseismic receiver functions, *Bulletin of the Seismological Society of America*, *87*(3), 745–754.

Peselnick, L., and A. Nicolas (1978), Seismic anisotropy in an ophiolite peridotite: application to oceanic upper mantle, *Journal of Geophysical Research: Solid Earth*, *83*(B3), 1227–1235.

Plafker, G., T. Hudson, T. Bruns, and M. Rubin (1978), Late Quaternary offsets along the Fairweather fault and crustal plate interactions in southern Alaska, *Canadian Journal of Earth Sciences*, *15*(5), 805–816, doi:10.1139/e78-085.

Powell, J., D. Schneider, D. Stockli, and K. Fallas (2016), Zircon (U-Th)/He thermochronology of Neoproterozoic strata from the Mackenzie Mountains, Canada: Implications for the Phanerozoic exhumation and deformation history of the northern Canadian Cordillera, *Tectonics*, *35*(3), 663–689, doi:10.1002/2015TC003989.

Powell, J. W., D. R. Issler, D. A. Schneider, K. M. Fallas, and D. F. Stockli (2019), Thermal history of the Mackenzie Plain, Northwest Territories, Canada: Insights from low-temperature thermochronology of the Devonian Imperial Formation, *GSA Bulletin*, *132*(3-4), 767–783, doi:10.1130/B35089.1.

Ranalli, G., and B. Fischer (1984), Diffusion creep, dislocation creep, and mantle rheology, *Physics of the Earth and Planetary Interiors*, *34*(1), 77 – 84, doi:https://doi.org/10.1016/0031-9201(84)90086-4.

Rasendra, N., M. Bonnin, S. Mazzotti, and C. Tiberi (2014), Crustal and Upper-Mantle Anisotropy Related to Fossilized Transpression Fabric along the Denali Fault, Northern Canadian Cordillera, *Bulletin of the Seismological Society of America*, *104*, 1964–1975, doi:10.1785/0120130233.

Roddick, J. A. (1967), Tintina Trench, *The Journal of Geology*, *75*(1), 23–33, doi:10.1086/627228.

Saltus, R. W. (2007), Matching magnetic trends and patterns across the Tintina fault, Alaska and Canada–evidence for offset of about 490 kilometers: Chapter C in Recent U.S. Geological Survey studies in the Tintina Gold Province, Alaska, United States, and Yukon, Canada–results of a 5-year project, *Tech. rep.*, Reston, VA, doi:10.3133/sir20075289C, report.

Sandvol, E., and T. Hearn (1994), Bootstrapping Shear-Wave Splitting Errors, *Bull. seism. Soc. Am.*, *84*.

Savage, M. K. (1999), Seismic anisotropy and mantle deformation: What have we learned from shear wave splitting?, *Reviews of Geophysics*, *37*(1), 65–106, doi:10.1029/98RG02075.

Savage, M. K., A. Wessel, N. A. Teanby, and A. W. Hurst (2010), Automatic measurement of shear wave splitting and applications to time varying anisotropy at Mount Ruapehu volcano, New Zealand, *Journal of Geophysical Research: Solid Earth*, *115*(B12), doi:10.1029/2010JB007722.

Schutt, D., E. Humphreys, and K. Dueker (1998), Anisotropy of the Yellowstone hot spot wake, eastern Snake River Plain, Idaho, *Pure and Applied Geophysics*, *151*, 443–462.

Sheaf, M. A., L. Serpa, and T. L. Pavlis (2003), Exhumation rates in the St. Elias Mountains, Alaska, *Tectonophysics*, *367*(1), 1 – 11, doi:https://doi.org/10.1016/S0040-1951(03)00124-0.

Silver, P. G., and W. W. Chan (1991), Shear wave splitting and subcontinental mantle deformation, *Journal of Geophysical Research: Solid Earth*, *96*(B10), 16,429–16,454, doi: 10.1029/91JB00899.

Skemer, P., and L. N. Hansen (2016), Inferring upper-mantle flow from seismic anisotropy: An experimental perspective, *Tectonophysics*, *668-669*, 1 – 14, doi:https://doi.org/10.1016/j.tecto. 2015.12.003.

Smith, M. L., and F. A. Dahlen (1973), The azimuthal dependence of Love and Rayleigh wave propagation in a slightly anisotropic medium, *Journal of Geophysical Research (1896-1977)*, *78*(17), 3321–3333, doi:10.1029/JB078i017p03321.

Snyder, D., and M. Bruneton (2007), Seismic Anisotropy of the Slave craton, NW Canada, from joint interpretation of SKS and Rayleigh waves, *Geophysical Journal International*, *169*, 170–188.

Stein, S., and M. Wysession (2003), *An introduction to seismology, earthquakes, and earth structure*, John Wiley & Sons.

Tanimoto, T., and D. L. Anderson (1985), Lateral heterogeneity and azimuthal anisotropy of the upper mantle: Love and Rayleigh waves 100–250 s, *Journal of Geophysical Research: Solid Earth*, *90*(B2), 1842–1858, doi:10.1029/JB090iB02p01842.

Tarayoun, A., P. Audet, S. Mazzotti, and A. Ashoori (2017), Architecture of the crust and uppermost mantle in the northern Canadian Cordillera from receiver functions, *Journal of Geophysical Research: Solid Earth*, *122*(7), 5268–5287, doi:10.1002/2017JB014284.

Turcotte, D., and G. Schubert (2014), *Geodynamics*, Cambridge University Press.

Venereau, C., R. Martin-Short, I. Bastow, R. Allen, and R. Kounoudis (2019), The role of variable slab dip in driving mantle flow at the eastern edge of the Alaskan subduction margin: insights from SKS shear-wave splitting, *Geochemistry, Geophysics, Geosystems*, doi: 10.1029/2018GC008170.

Walsh, E., R. Arnold, and M. K. Savage (2013), Silver and Chan revisited, *Journal of Geophysical Research: Solid Earth*, *118*(10), 5500–5515, doi:https://doi.org/10.1002/jgrb.50386.

Wang, W., and T. W. Becker (2019), Upper mantle seismic anisotropy as a constraint for mantle flow and continental dynamics of the North American plate, *Earth and Planetary Science Letters*, *514*, 143 – 155, doi:https://doi.org/10.1016/j.epsl.2019.03.019.

Whittle, P. (1953), Estimation and information in stationary time series, *Ark. Mat.*, *2*(5), 423–434, doi:10.1007/BF02590998.

Wolfe, C. J., and P. G. Silver (1998), Seismic anisotropy of oceanic upper mantle: Shear wave splitting methodologies and observations, *Journal of Geophysical Research: Solid Earth*, *103*(B1), 749–771, doi:10.1029/97JB02023.

Wuestefeld, A., O. Al-Harrasi, J. P. Verdon, J. Wookey, and J. M. Kendall (2010), A strategy for automated analysis of passive microseismic data to image seismic anisotropy and fracture characteristics, *Geophysical Prospecting*, *58*(5), 755–773, doi:https://doi.org/10.1111/j.1365-2478.2010.00891.x.

Wüstefeld, A., G. Bokelmann, C. Zaroli, and G. Barruol (2008), SplitLab: A shear-wave splitting environment in Matlab, *Computers Geosciences*, *34*(5), 515 – 528, doi:https://doi.org/10.1016/j.cageo.2007.08.002.

Chapter 3

3.1 Future Work

The availability of seismic data in the northern Canadian Cordillera is increasing, and with it the prospect of better understanding the deep Earth within this region. Arrays such as the Mackenzie Mountain array (7C), Transportable Array (TA), and others provide the opportunity to better constrain both shallow and deep Earth structures and better understand the dynamics of modern Cordilleran deformation. Prospective studies in the NCC are outlined within this section.

Getting the Whittle Likelihood Estimation method code working is foremost of the work to be done after this study. This code package needs to be able to better resolve synthetic tests of various backazimuths for low SNR tests, such that the input splitting parameters are within the distribution of bootstrap realizations. We were not able to pinpoint the exact cause of the code's discrepancies, but we suspect it is related to the ψ term that indicates the angle between the fast axis orientation ϕ and the backazimuth θ. This suspicion is based on the observation that the maximum likelihood surface for events of backazimuth varying by 10 degrees showed great periodicity in the best-fitting fast axis orientations. For synthetic tests with a SNR of 5, vertical ray incidence, and a single-layer of horizontal, hexagonally anisotropic mantle, we observed that best-fitting splitting parameters were exactly dependent on the backazimuthl; for example, an event with backazimuth of 0 degrees was able to resolve the input anisotropy perfectly, but an event with backazimuth equal to 20 degrees would give a fast axis orientation of $\phi_{input} + 20°$. Delay times did not seem to be periodic in this fashion, though they did vary much as the backazimuth changed. This could be expected for null and near-null events, but should be roughly uniform for all other backazimuths. Note that the backazimuth here (and in Telewavesim) is interpreted to be the input polarization of the incidence XKS phase before splitting.

After fixing the code, the Whittle Likelihood Estimation method may be augmented to better resolve multiple layers of anisotropy and/or dipping anisotropy, as the impulse response functions computed in the *Menke and Levin* (2003) cross-convolution method are readily adapted for these

scenarios. The two-layer splitting augmentation may involve a second grid search over additional best-fitting splitting parameters, maximizing the likelihood that both layers represent the true earth model, compared to a single layer of anisotropy. Previous studies within the NCC attribute components from the lithosphere and asthenosphere to the true anisotropy (e.g. *Audet et al.*, 2016; *Courtier et al.*, 2010; *Rasendra et al.*, 2014). The WLEM may also be augmented so that the formulation of the pre-event noise spectral characteristics does not assume a single-layer of hexagonal anisotropy and a vertically incident XKS phase. Additionally, one simple but possibly useful adaptation of the WLEM code is an adaptation to a different coding language. The current version of the code provided in Appendices A and B is written in *R*, but could be adapted to *MATLAB* or *Python* so that it is more familiar to a broader scientific audience.

Given the receiver-side anisotropy computed from the XKS phases, one could use S-wave splitting techniques to determine source-side anisotropy, such as that suggested in *Eken and Tilmann* (2014). The *Menke and Levin* (2003) method's impulse response functions could be modified in a similar manner to two-layer splitting to account for source- and receiver-side anisotropy, and the receiver-side anisotropy can be fit to the apparent splitting parameters computed from this or other XKS splitting studies.

Local S-phases may be used to better constrain crustal anisotropy and can be computed using MFAST (*Savage et al.*, 2010). Constraints on crustal anisotropy may assist in understanding the overall structure of the lithosphere and perhaps provide evidence for or against the *Mazzotti and Hyndman* (2002) hypothesis of a lower crustal décollement. This lower crustal décollement would have a highly sheared fabric that should be visible in local shear wave splitting studies if depth can be constrained.

This study region may be well suited for Rayleigh wave anisotropy studies which would assist in determining depth-dependent anisotropy. *Snyder and Bruneton* (2007) utilized Rayleigh wave anisotropy to compound their shear wave splitting results determined by SKS and SKKS waves. They note that Rayleigh waves are sensitive to changes in vertical velocity gradients which could be used to augment the determination of dipping or vertical anisotropic fabrics. I note here that the

lithosphere in the region around the MMEP network is anomalously thin (e.g. *Audet et al.*, 2019b), so these Rayleigh waves could be used to examine a greater thickness of asthenosphere. To do this, one could first compute backazimuth and mean phase velocity of Rayleigh waves across an array, then calculate the overall mean phase velocity and determine the azimuthal variation of that phase velocity (*Snyder and Bruneton*, 2007).

Shear wave velocity structures can also be determined using Rayleigh and Love wave tomography. Variations in phase and group velocities in surface waves have long been used to estimate lithospheric seismic anisotropy *Eddy et al.* (e.g. 2018); *Montagner and Tanimoto* (e.g. 1991); *Smith and Dahlen* (e.g. 1973); *Tanimoto and Anderson* (e.g. 1985). Often these studies characterize azimuthal anisotropy within the lithosphere, as the phase and group velocities of these surface waves are azimuthally dependent. *Smith and Dahlen* (1973) provides a mathematical framework for the dependence of Rayleigh and Love wave phase velocities on azimuth. These studies often utilize hundreds to thousands of Rayleigh and Love wave paths (e.g. *Eddy et al.*, 2018; *Montagner and Tanimoto*, 1991). Anisotropy is often determined from velocity variations based on the azimuth of the surface wave. One interested in performing a surface wave anisotropy study could use the code developed for the *Debayle and Sambridge* (2004) method, which may be able to process thousands of ray paths in a few hours. This method not only able to assess anisotropy, but also allows for the user to perform surface wave tomography. Documentation for this software package and information on retrieval can be found here. Tangential receiver functions also allow for the determination of dipping anisotropy (e.g. *McNamara and Owens*, 1993; *Peng and Humphreys*, 1997). These studies can use Ps phases and involve assessing the shear wave splitting of the s-leg of the phase after conversion at the Moho. One could perform a simple shear wave splitting analysis on this phase, but waveform modeling (i.e. receiver function analysis) provides the opportunity to also resolve dipping anisotropy (e.g. *Peng and Humphreys*, 1997). *Peng and Humphreys* (1997) utilizes the ray tracing code of *Langston* (1977) to calculate the incidence angle of the incoming sphase, as well as the dip direction. Anisotropic parameters are determined using typical splitting methods (e.g. *Corbalán et al.*, in revision; *Menke and Levin*, 2003; *Silver and Chan*, 1991).

3.2 Data Acquisition

The data used for this project was acquired using Standing Order for Data (SOD) (*Owens et al.*, 2004). SOD is a software package that allows an easy query to the Incorporated Research Institutions for Seismology (IRIS) Data Management Center (DMC). Using SOD, one can readily create XML 'recipes' containing the necessary event, station, and seismogram information to be requested. The SOD recipe can be augmented to request data with specified date interval, event-station distance, signaltonoise ratio, gain code, band code, orientation code, as well as to remove data mean and trend, among others. One can also rotate the data to radial and transverse components, remove overlapping phases interfering with XKS arrivals, and mark the phase arrivals using a velocity model, all of which are particularly useful in shear wave splitting studies, which require much data screening before any analysis can begin.

3.3 Data Pre-processing

The Whittle Likelihood Estimation Method (*Corbalán*, 2016; *Corbalán et al.*, in revision) requires seismograms centered around the XKS arrival with an equal number of sample points before the arrival (pre-event noise) and after the arrival (signal + noise). This method also requires equally-spaced samples, although this is not typically an issue in seismic studies. The procedure we adopted for this analysis is as follows:

1. Download seismogram files for each seismic station to be included in the study and organize them into event folders. We do this in order to print record sections of each event, which are used to determine whether the event is a 'good' event (i.e. that the XKS arrival appears clear on many radial and transverse channels). This is done to cut down on the amount of time spent on Step 2 of this procedure, but this is optional.

2. Loop through the 'good events' data and examine individual radial and transverse traces to determine whether a specific station-event pair shows a clean XKS arrival with little phase interference and a high enough SNR to warrant analysis. These data are organized by station.

Clean arrivals are further organized by quality: quality 1 events show very clean arrivals with high SNR and little coda, while quality 2 events have less SNR and more coda than q1 events. Quality 2 events typically have more data which may be useful in solidifying our understanding of the study region. We also categorize null splits in which no transverse energy is recorded; isolating the nulls allows one to compare their input polarization to the station averages. This comparison serves as a check to ensure that the results are realistic.

3. Manually choose the XKS arrival to mark the true arrival, rather than an arrival predicted by velocity model. This step is done to better estimate the pre-event noise in the XKS seismogram; if the velocity model misplaces the arrival later than the true arrival, some of the signal will be assessed as pre-event noise and can alter the results given in the final output.

4. After choosing the XKS arrival manually, cut the seismogram to an equal length before and after the arrival. We cut to 20 s before and after the arrival, but any length of trace should be useable so long as there are no interfering phases within the time range specified.

5. Create a list of events for each station, named "<station>_events.txt". The WLEM code uses these files to loop over the seismograms being processed. A list of stations within a file called "stations.txt" must also be generated in order for the code to loop over each station directory holding all the RT traces. Station names within "stations.txt" must match the name of the station directories.

Shell scripts that perform all of these pre-processing steps can be found on at Colorado State University's Warner College of Natural Resources Network: */data/seismo/Bolton/scripts*.

3.4 Running the WLEM Code

The WLEM code used in this study is written in *R*, an open-source coding language that is quite popular due to its numerous statistical functions. This code requires version 3+ of *R*. The code can be run solely from Mac or Linux command line, or via a GUI such as *RStudio*, which may be useful

for debugging. This code consists of two scripts, titled "Step_1_Setup.R" and "Step_2_Data.R". Step_1_Setup.R should be run first as it creates a number of functions to be utilized in the analysis. For example, Step_1_Setup.R contains functions to be able to read SAC files containing the data to be analyzed, read their headers and use the header information in the analysis, setup the Whittle Likelihood approximation, etc. Step_2_Data.R performs the actual analysis. After pre-processing according to section 3.3 is completed, the code can be run as follows:

1. Source Step_1_Setup.R to import the necessary functions

2. In Step_2_Data.R, change the variable "pathname" to the path of the master directory containing station-event directories, the stations text file, and station-event list text files. One could create a script that passes a global variable into the "pathname" variable in order to loop through multiple master directories, such as the quality directories we created in this analysis. You may also need to change the variable "cut" depending on the data's sampling rate. The default "cut" value is based off a 50 Hz sampling rate.

3. Source Step_2_Data.R to run the analysis. Outputs are:

   (a) Splitting results text file containing δt and ϕ

   (b) Splitting containing δt, ϕ, $\sigma\delta t$, and $\sigma\phi$

   (c) A pdf of the log likelihood surface with chosen splitting parameters highlighted at the global maximum of the station average.

   (d) A text file containing the likelihood values used to generate the log likelihood surface

   (e) A list for each event in the station directory comparing the event backazimuth to the highest likelihood fast axis orientation (NET.STA_baz_vs_fast_axis.txt)

   (f) A list for each event in the station directory comparing the event backazimuth to the highest likelihood split time (NET.STA_baz_vs_split_time.txt)

   (g) A list of each bootstrapping iteration for the station average showing the fast-axis orientation and split time for those consecutive iterations

(h) A list of each bootstrap iteration of all station-events showing fast-axis orientation and split time for all bootstraps.

Bibliography

Alsina, D., and R. Snieder (1995), Small-scale sublithospheric continental mantle deformation: constraints from SKS splitting observations, *Geophysical Journal International*, *123*(2), 431–448, doi:10.1111/j.1365-246X.1995.tb06864.x.

Argus, D. F., R. G. Gordon, M. B. Heflin, C. Ma, R. J. Eanes, P. Willis, W. R. Peltier, and S. E. Owen (2010), The angular velocities of the plates and the velocity of Earth's centre from space geodesy, *Geophysical Journal International*, *180*(3), 913–960, doi:10.1111/j.1365-246X.2009.04463.x.

Audet, P., C. Sole, and A. J. Schaeffer (2016), Control of lithospheric inheritance on neotectonic activity in northwestern Canada?, *Geology*, *44*(10), 807–810.

Audet, P., C. J. Thomson, M. G. Bostock, and T. Eulenfeld (2019a), Telewavesim: Python software for teleseismic body wave modeling, doi:10.5281/zenodo.3551258.

Audet, P., C. A. Currie, A. J. Schaeffer, and A. M. Hill (2019b), Seismic Evidence for Lithospheric Thinning and Heat in the northern Canadian Cordillera, *Geophysical Research Letters*, *46*(8), 4249–4257, doi:10.1029/2019GL082406.

Baker, M. G., D. C. Heath, D. L. Schutt, R. C. Aster, J. F. Cubley, and J. T. Freymueller (2020), The Mackenzie Mountains EarthScope Project: Studying Active Deformation in the Northern North American Cordillera from Margin to Craton, *Seismological Research Letters*, *91*(1), 521–532, doi:10.1785/0220190139.

Ben-Ismail, W., and D. Mainprice (1998), An olivine fabric database: an overview of upper mantle fabrics and seismic anisotropy, *Tectonophysics*, *296*, 145–157.

Bernard, R. E., W. M. Behr, T. W. Becker, and D. J. Young (2019), Relationships Between Olivine CPO and Deformation Parameters in Naturally Deformed Rocks and Implications for Mantle

Seismic Anisotropy, *Geochemistry, Geophysics, Geosystems*, *20*(7), 3469–3494, doi:10.1029/2019GC008289.

Bowman, J. R., and M. Ando (1987), Shear-wave splitting in the upper-mantle wedge above the Tonga subduction zone, *Geophysical Journal International*, *88*(1), 25–41, doi:10.1111/j.1365-246X.1987.tb01367.x.

Clowes, R., P. Hammer, G. Fernandez-Viejo, and K. Welford (2005), Lithospheric structure in northwestern Canada from LITHOPROBE seismic refraction and related studies: a synthesis, *Canadian Journal of Earth Sciences*, *42*, 1277–1293, doi:10.1139/e04-069.

Colpron, M., and J. L. Nelson (2011), A digital atlas of terranes for the northern Cordillera, *Yukon Geological Survey*.

Corbalán, A. (2016), A new method to test shear wave splitting: improving statistical assessment of splitting parameters.

Corbalán, A., F. Breidt, D. Witt, and D. Schutt (in revision), Whittle Likelihood Estimation of Shear-wave Splitting Parameters in the Presence of Highly-Corrleted Microseismic Noise.

Cordier, P., T. Ungár, L. Zsoldos, and G. Tichy (2004), Dislocation creep in MgSiO3 perovskite at conditions of the Earth's uppermost lower mantle, *Nature*, *428*, 837–40, doi:10.1038/nature02472.

Courtier, A., J. Gaherty, J. Revenaugh, M. Bostock, and E. Garnero (2010), Seismic anisotropy associated with continental lithosphere accretion beneath the CANOE array, Northwestern Canada, *Geology*, *38*(10), 887–890, doi:10.1130/G31120.1.

Crampin, S. (1981), A review of wave motion in anisotropic and cracked elastic-media, *Wave motion*, *3*(4), 343–391.

Crampin, S. (1984), An introduction to wave propagation in anisotropic media, *Geophysical Journal of the Royal Astronomical Society*, *76*(1), 17–28, doi:10.1111/j.1365-246X.1984.tb05018.x.

Crotwell, H. P., T. J. Owens, and J. Ritsema (1999), The TauP Toolkit: Flexible Seismic Travel-time and Ray-path Utilities, *Seismological Research Letters*, *70*(2), 154–160, doi:10.1785/gssrl.70.2.154.

Debayle, E., and M. Sambridge (2004), Inversion of massive surface wave data sets: Model construction and resolution assessment, *Journal of Geophysical Research: Solid Earth*, *109*(B2), doi:10.1029/2003JB002652.

Eddy, C. L., G. Ekström, M. Nettles, and J. B. Gaherty (2018), Age dependence and anisotropy of surface-wave phase velocities in the Pacific, *Geophysical Journal International*, *216*(1), 640–658, doi:10.1093/gji/ggy438.

Eken, T., and F. Tilmann (2014), The Use of Direct Shear Waves in Quantifying Seismic Anisotropy: Exploiting Regional Arrays, *Bulletin of the Seismological Society of America*, *104*, 2644–2661, doi:10.1785/0120140020.

Enkelmann, E., E. Finzel, and J. Arkle (2019), Deformation at the eastern margin of the Northern Canadian Cordillera: Potentially related to opening of the North Atlantic, *Terra Nova*, *31*(3), 151–158, doi:10.1111/ter.12374.

Estève, C., P. Audet, A. J. Schaeffer, D. L. Schutt, R. C. Aster, and J. F. Cubley (2020), Seismic evidence for craton chiseling and displacement of lithospheric mantle by the Tintina fault in the northern Canadian Cordillera, *Geology*, doi:10.1130/G47688.1.

Finzel, E. S., L. M. Flesch, K. D. Ridgway, W. E. Holt, and A. Ghosh (2015), Surface motions and intraplate continental deformation in Alaska driven by mantle flow, *Geophysical Research Letters*, *42*(11), 4350–4358, doi:10.1002/2015GL063987.

Frederiksen, A., M. Bostock, and J. Cassidy (2001), S-wave velocity structure of the Canadian upper mantle, *Physics of the Earth and Planetary Interiors*, *124*(3), 175 – 191, doi:https://doi.org/10.1016/S0031-9201(01)00194-7.

Frost, D. J. (2008), The upper mantle and transition zone, *Elements*, *4*(3), 171–176.

Gabrielse, H. (1985), Major dextral transcurrent displacements along the Northern Rocky Mountain Trench and related lineaments in north-central British Columbia, *GSA Bulletin*, *96*(1), 1–14, doi:10.1130/0016-7606(1985)96<1:MDTDAT>2.0.CO;2.

Green II, H. W., and S. V. Radcliffe (1972), *Deformation Processes in the Upper Mantle*, pp. 139–156, American Geophysical Union (AGU), doi:10.1029/GM016p0139.

Gueguen, Y. (1977), Dislocations in mantle peridotite nodules, *Tectonophysics*, *39*(1), 231 – 254, doi:https://doi.org/10.1016/0040-1951(77)90098-1, fabrics, microstructures, and microtectonics.

Hanna, J., and M. D. Long (2012), SKS splitting beneath Alaska: Regional variability and implications for subduction processes at a slab edge.

Hayward, N. (2015), Geophysical investigation and reconstruction of lithospheric structure and its control on geology, structure, and mineralization in the Cordillera of northern Canada and eastern Alaska, *Tectonics*, *34*(10), 2165–2189, doi:https://doi.org/10.1002/2015TC003871.

Hess, H. (1964), Seismic anisotropy of the uppermost mantle under oceans, *Nature*, *203*(4945), 629.

Hyndman, R., P. Flueck, S. Mazzotti, T. J Lewis, J. Ristau, and L. Leonard (2005), Current tectonics of the northern Canadian Cordillera, *Canadian Journal of Earth Sciences*, *42*, 1117–1136, doi:10.1139/e05-023.

Jin, Z.-M., H. Green, and R. Borch (1989), Microstructures of olivine and stresses in the upper mantle beneath Eastern China, *Tectonophysics*, *169*(1), 23 – 50, doi:https://doi.org/10.1016/0040-1951(89)90181-9.

Karato, S., and P. Wu (1993), Rheology of the Upper Mantle: A Synthesis, *Science*, *260*(5109), 771–778.

Karato, S., S. Zhang, and H.-R. Wenk (1995), Superplasticity in Earth's Lower Mantle: Evidence from Seismic Anisotropy and Rock Physics, *Science*, *270*(5235), 458–461.

Karato, S.-I. (2013), *Rheological Properties of Minerals and Rocks*, chap. 4, pp. 94–144, John Wiley Sons, Ltd, doi:https://doi.org/10.1002/9781118529492.ch4.

Karato, S.-i., H. Jung, I. Katayama, and P. Skemer (2008), Geodynamic Significance of Seismic Anisotropy of the Upper Mantle: New Insights from Laboratory Studies, *Annu. Rev. Earth Planet. Sci.*, *36*, 59–95, doi:10.1146/annurev.earth.36.031207.124120.

Kendall, M. (2007), *D´´, Anisotropy*, pp. 146–149, Springer Netherlands, Dordrecht, doi:10.1007/978-1-4020-4423-6_61.

Kennett, B. L. N., E. R. Engdahl, and R. Buland (1995), Constraints on seismic velocities in the Earth from traveltimes, *Geophysical Journal International*, *122*(1), 108–124, doi:10.1111/j.1365-246X.1995.tb03540.x.

Langston, C. A. (1977), The effect of planar dipping structure on source and receiver responses for constant ray parameter, *Bulletin of the Seismological Society of America*, *67*(4), 1029–1050.

Leonard, L. J., S. Mazzotti, and R. D. Hyndman (2008), Deformation rates estimated from earthquakes in the northern Cordillera of Canada and eastern Alaska, *Journal of Geophysical Research: Solid Earth*, *113*(B8), doi:10.1029/2007JB005456.

Lev, E. (2009), Elastic and viscous anisotropy in Earth's mantle - observations and implications, Ph.D. thesis, Massachusetts Institute of Technology.

Lewis, T. J., R. D. Hyndman, and P. Flück (2003), Heat flow, heat generation, and crustal temperatures in the northern Canadian Cordillera: Thermal control of tectonics, *Journal of Geophysical Research: Solid Earth*, *108*(B6), doi:https://doi.org/10.1029/2002JB002090.

Long, M. D., and P. G. Silver (2009), Shear Wave Splitting and Mantle Anisotropy: Measurements, Interpretations, and New Directions, *Surveys in Geophysics*, *30*(4), 407–461, doi: 10.1007/s10712-009-9075-1.

Mazzotti, S., and R. Hyndman (2002), Yakutat collision and strain transfer across the northern Canadian Cordillera, *Geology*, *30*, doi:10.1130/0091-7613(2002)030<0495:YCASTA>2.0.CO; 2.

McNamara, D. E., and T. J. Owens (1993), Azimuthal shear wave velocity anisotropy in the Basin and Range Province using moho Ps converted phases, *Journal of Geophysical Research: Solid Earth*, *98*(B7), 12,003–12,017, doi:10.1029/93JB00711.

Menke, W., and V. Levin (2003), The cross-convolution method for interpreting SKS splitting observations, with application to one and two-layer anisotropic earth models, *Geophysical Journal International*, *154*(2), 379–392, doi:10.1046/j.1365-246X.2003.01937.x.

Mizukami, T., S. R. Wallis, and J. Yamamoto (2004), Natural examples of olivine lattice preferred orientation patterns with a flow-normal a-axis maximum, *Nature*, *427*(6973), 432–436.

Monger, J., and R. Price (2002), The Canadian Cordillera: Geology and Tectonic Evolution, *CSEG Recorder*, p. 17.

Montagner, J.-P., and T. Tanimoto (1991), Global upper mantle tomography of seismic velocities and anisotropies, *Journal of Geophysical Research: Solid Earth*, *96*(B12), 20,337–20,351, doi: 10.1029/91JB01890.

Nelson, J. L., M. Colpron, and S. Israel (2013), The Cordillera of British Columbia, Yukon, and Alaska: Tectonics and Metallogeny, in *Tectonics, Metallogeny, and Discovery: The North American Cordillera and Similar Accretionary Settings*, Society of Economic Geologists, doi: 10.5382/SP.17.03.

Oldow, J. S., A. W. Bally, and H. G. Ave Lallemant (1990), Transpression, orogenic float, and lithospheric balance, *Geology*, *18*(10), 991–994, doi:10.1130/0091-7613(1990)018<0991:TOFALB>2.3.CO;2.

Owens, T. J., H. P. Crotwell, C. Groves, and P. Oliver-Paul (2004), SOD: Standing order for data, *Seismological Research Letters - SEISMOL RES LETT*, *75*, 515–520, doi:10.1785/gssrl.75.4.515-a.

Park, J., and V. Levin (2002), Seismic Anisotropy: Tracing Plate Dynamics in the Mantle, *Science*, *296*(5567), 485–489, doi:10.1126/science.1067319.

Peng, X., and E. D. Humphreys (1997), Moho dip and crustal anisotropy in northwestern Nevada from teleseismic receiver functions, *Bulletin of the Seismological Society of America*, *87*(3), 745–754.

Peselnick, L., and A. Nicolas (1978), Seismic anisotropy in an ophiolite peridotite: application to oceanic upper mantle, *Journal of Geophysical Research: Solid Earth*, *83*(B3), 1227–1235.

Plafker, G., T. Hudson, T. Bruns, and M. Rubin (1978), Late Quaternary offsets along the Fairweather fault and crustal plate interactions in southern Alaska, *Canadian Journal of Earth Sciences*, *15*(5), 805–816, doi:10.1139/e78-085.

Powell, J., D. Schneider, D. Stockli, and K. Fallas (2016), Zircon (U-Th)/He thermochronology of Neoproterozoic strata from the Mackenzie Mountains, Canada: Implications for the Phanerozoic exhumation and deformation history of the northern Canadian Cordillera, *Tectonics*, *35*(3), 663–689, doi:10.1002/2015TC003989.

Powell, J. W., D. R. Issler, D. A. Schneider, K. M. Fallas, and D. F. Stockli (2019), Thermal history of the Mackenzie Plain, Northwest Territories, Canada: Insights from low-temperature thermochronology of the Devonian Imperial Formation, *GSA Bulletin*, *132*(3-4), 767–783, doi:10.1130/B35089.1.

Ranalli, G., and B. Fischer (1984), Diffusion creep, dislocation creep, and mantle rheology, *Physics of the Earth and Planetary Interiors*, *34*(1), 77 – 84, doi:https://doi.org/10.1016/0031-9201(84)90086-4.

Rasendra, N., M. Bonnin, S. Mazzotti, and C. Tiberi (2014), Crustal and Upper-Mantle Anisotropy Related to Fossilized Transpression Fabric along the Denali Fault, Northern Canadian Cordillera, *Bulletin of the Seismological Society of America*, *104*, 1964–1975, doi:10.1785/0120130233.

Roddick, J. A. (1967), Tintina Trench, *The Journal of Geology*, *75*(1), 23–33, doi:10.1086/627228.

Saltus, R. W. (2007), Matching magnetic trends and patterns across the Tintina fault, Alaska and Canada–evidence for offset of about 490 kilometers: Chapter C in Recent U.S. Geological Survey studies in the Tintina Gold Province, Alaska, United States, and Yukon, Canada–results of a 5-year project, *Tech. rep.*, Reston, VA, doi:10.3133/sir20075289C, report.

Sandvol, E., and T. Hearn (1994), Bootstrapping Shear-Wave Splitting Errors, *Bull. seism. Soc. Am.*, *84*.

Savage, M. K. (1999), Seismic anisotropy and mantle deformation: What have we learned from shear wave splitting?, *Reviews of Geophysics*, *37*(1), 65–106, doi:10.1029/98RG02075.

Savage, M. K., A. Wessel, N. A. Teanby, and A. W. Hurst (2010), Automatic measurement of shear wave splitting and applications to time varying anisotropy at Mount Ruapehu volcano, New Zealand, *Journal of Geophysical Research: Solid Earth*, *115*(B12), doi:10.1029/2010JB007722.

Schutt, D., E. Humphreys, and K. Dueker (1998), Anisotropy of the Yellowstone hot spot wake, eastern Snake River Plain, Idaho, *Pure and Applied Geophysics*, *151*, 443–462.

Sheaf, M. A., L. Serpa, and T. L. Pavlis (2003), Exhumation rates in the St. Elias Mountains, Alaska, *Tectonophysics*, *367*(1), 1 – 11, doi:https://doi.org/10.1016/S0040-1951(03)00124-0.

Silver, P. G., and W. W. Chan (1991), Shear wave splitting and subcontinental mantle deformation, *Journal of Geophysical Research: Solid Earth*, *96*(B10), 16,429–16,454, doi:10.1029/91JB00899.

Skemer, P., and L. N. Hansen (2016), Inferring upper-mantle flow from seismic anisotropy: An experimental perspective, *Tectonophysics*, *668-669*, 1 – 14, doi:https://doi.org/10.1016/j.tecto.2015.12.003.

Smith, M. L., and F. A. Dahlen (1973), The azimuthal dependence of Love and Rayleigh wave propagation in a slightly anisotropic medium, *Journal of Geophysical Research (1896-1977)*, *78*(17), 3321–3333, doi:10.1029/JB078i017p03321.

Snyder, D., and M. Bruneton (2007), Seismic Anisotropy of the Slave craton, NW Canada, from joint interpretation of SKS and Rayleigh waves, *Geophysical Journal International*, *169*, 170–188.

Stein, S., and M. Wysession (2003), *An introduction to seismology, earthquakes, and earth structure*, John Wiley & Sons.

Tanimoto, T., and D. L. Anderson (1985), Lateral heterogeneity and azimuthal anisotropy of the upper mantle: Love and Rayleigh waves 100–250 s, *Journal of Geophysical Research: Solid Earth*, *90*(B2), 1842–1858, doi:10.1029/JB090iB02p01842.

Tarayoun, A., P. Audet, S. Mazzotti, and A. Ashoori (2017), Architecture of the crust and uppermost mantle in the northern Canadian Cordillera from receiver functions, *Journal of Geophysical Research: Solid Earth*, *122*(7), 5268–5287, doi:10.1002/2017JB014284.

Turcotte, D., and G. Schubert (2014), *Geodynamics*, Cambridge University Press.

Venereau, C., R. Martin-Short, I. Bastow, R. Allen, and R. Kounoudis (2019), The role of variable slab dip in driving mantle flow at the eastern edge of the Alaskan subduction margin: insights from SKS shear-wave splitting, *Geochemistry, Geophysics, Geosystems*, doi:10.1029/2018GC008170.

Walsh, E., R. Arnold, and M. K. Savage (2013), Silver and Chan revisited, *Journal of Geophysical Research: Solid Earth*, *118*(10), 5500–5515, doi:https://doi.org/10.1002/jgrb.50386.

Wang, W., and T. W. Becker (2019), Upper mantle seismic anisotropy as a constraint for mantle flow and continental dynamics of the North American plate, *Earth and Planetary Science Letters*, *514*, 143 – 155, doi:https://doi.org/10.1016/j.epsl.2019.03.019.

Whittle, P. (1953), Estimation and information in stationary time series, *Ark. Mat.*, *2*(5), 423–434, doi:10.1007/BF02590998.

Wolfe, C. J., and P. G. Silver (1998), Seismic anisotropy of oceanic upper mantle: Shear wave splitting methodologies and observations, *Journal of Geophysical Research: Solid Earth*, *103*(B1), 749–771, doi:10.1029/97JB02023.

Wuestefeld, A., O. Al-Harrasi, J. P. Verdon, J. Wookey, and J. M. Kendall (2010), A strategy for automated analysis of passive microseismic data to image seismic anisotropy and fracture characteristics, *Geophysical Prospecting*, *58*(5), 755–773, doi:https://doi.org/10.1111/j.1365-2478.2010.00891.x.

Wüstefeld, A., G. Bokelmann, C. Zaroli, and G. Barruol (2008), SplitLab: A shear-wave splitting environment in Matlab, *Computers Geosciences*, *34*(5), 515 – 528, doi:https://doi.org/10.1016/j.cageo.2007.08.002.

Appendix A

Individual results

A.1 Tables

Table A.1: Individual station-event results for the MMEP network.

Station	**Event Info**					**SplitLab Results**							
	date	evlo	evla	baz	Mw	fastRC	σ_{fastRC}	δtRC	$\sigma_{\delta tRC}$	fastSC	σ_{fastSC}	δtSC	$\sigma_{\delta tSC}$
MM02	02-Apr-2018	-63.01	-20.66	115.79	6.8	-12.47	9.50	0.78	0.17	-28.47	8.50	0.95	0.16
MM02	13-Aug-2017	101.62	-3.77	298.06	6.4	-10.14	13.00	0.95	0.29	-16.14	14.00	1.00	0.28
MM03	02-Apr-2018	-63.01	-20.66	115.91	6.8	-14.36	15.50	0.62	0.46	-10.36	13.50	0.95	0.29
MM04	23-Aug-2016	122.43	-7.29	277.72	6	-16.36	7.50	0.50	0.09	-66.36	4.00	3.50	0.20
MM05	15-Dec-2017	108.17	-7.49	291.07	6.5	-11.09	14.50	0.25	0.17	-61.09	3.00	3.70	0.68
MM05	15-Jul-2017	121.98	0.41	282.45	5.9	-21.71	9.50	0.25	0.12	-69.71	1.50	2.45	0.31
MM05	21-Feb-2017	-63.90	-19.28	116.52	6.5	-17.76	5.50	0.15	0.08	12.24	22.00	0.55	0.82
MM05	23-Aug-2016	122.54	-7.21	278.18	5.8	72.10	7.50	0.00	0.04	-71.90	4.00	1.65	0.55
MM05	23-Aug-2016	122.43	-7.29	278.24	6	70.16	8.00	0.00	0.03	-71.84	2.00	1.60	0.28
MM06	15-Dec-2017	108.17	-7.49	291.76	6.5	-34.41	10.00	0.40	0.20	-76.41	3.50	4.00	0.35

Continued on next page

Continued from previous page

MM06	21-Feb-2017	-63.90	-19.28	117.08	6.5	-25.21	13.00	0.35	0.15	14.79	19.50	1.15	0.78
MM07	23-Aug-2016	122.54	-7.21	279.09	5.8	-28.01	11.00	0.25	0.14	-33.01	90.00	0.20	2
MM07	23-Aug-2016	122.43	-7.29	279.14	6	-28.95	9.00	0.25	0.11	-32.95	90.00	0.20	2
MM07	28-Jul-2018	122.73	-7.10	278.97	6	-36.12	6.25	0.17	0.05	-37.12	90.00	0.15	2
MM07	04-Aug-2016	-66.01	-22.33	120.42	6.2	-10.88	15.25	0.50	0.18	-22.88	17.00	0.55	0.31
MM07	21-Jan-2018	-69.44	-18.88	121.76	6.3	-6.60	7.75	0.57	0.12	-33.60	12.00	0.80	0.31
MM07	20-Nov-2016	-68.63	-31.62	126.90	6.4	-3.36	14.75	1.15	0.35	-1.36	12.75	1.25	0.36
MM07	15-Dec-2017	108.17	-7.49	292.06	6.5	-17.10	8.25	0.07	0.06	-53.10	21.75	0.30	0.29
MM07	21-Feb-2017	-63.90	-19.28	117.25	6.5	-6.05	11.50	0.38	0.11	-47.05	11.75	0.90	0.38
MM07	31-Oct-2017	169.15	-21.70	232.06	6.7	-83.55	6.25	0.35	0.10	-74.55	13.75	0.50	0.17
MM07	02-Apr-2018	-63.01	-20.66	117.13	6.8	-9.14	10.25	0.33	0.09	-51.14	9.00	1.20	0.42
MM08	24-Apr-2017	-72.06	-33.04	130.16	6.9	-8.11	14.00	0.50	0.32	-34.11	6.00	1.20	0.31
MM08	21-Feb-2017	-63.90	-19.28	117.19	6.5	-27.10	6.50	0.62	0.05	-19.10	5.50	0.60	0.06
MM08	20-Nov-2016	-68.63	-31.62	126.80	6.4	8.53	10.00	1.05	0.23	6.53	4.50	1.05	0.14
MM09	02-Apr-2018	-63.01	-20.66	117.09	6.8	-17.18	8.50	0.65	0.08	-31.18	2.00	0.80	0.04
MM09	21-Feb-2017	-63.90	-19.28	117.22	6.5	-35.07	6.50	0.80	0.10	-33.07	3.00	0.80	0.07
MM09	20-Nov-2016	-68.63	-31.62	126.79	6.4	-17.47	11.50	0.95	0.19	-11.47	5.50	1.00	0.09

Continued on next page

Continued from previous page

MM09	23-Aug-2016	122.54	-7.21	279.28	5.8	-36.82	12.00	0.35	0.11	-62.82	4.50	0.70	0.15
MM09	23-Aug-2016	122.43	-7.29	279.33	6	-38.76	12.50	0.35	0.11	-62.76	4.50	0.65	0.12
MM09	25-Jul-2016	-70.51	-26.11	125.81	6.1	-16.50	6.00	1.85	0.24	-4.50	7.00	1.95	0.36
MM10	20-Nov-2016	-68.63	-31.62	126.68	6.4	-29.57	13.00	0.97	0.33	-33.57	8.00	1.10	0.29
MM10	21-Feb-2017	-63.90	-19.28	117.13	6.5	-45.15	3.00	1.40	0.06	-35.15	3.00	1.30	0.12
MM10	02-Apr-2018	-63.01	-20.66	117.00	6.8	-47.27	4.00	1.15	0.16	-45.27	3.00	1.10	0.16
MM11	28-Jul-2018	122.73	-7.10	279.37	6	-14.72	8.00	0.10	0.09	-64.72	2.00	1.85	0.15
MM11	17-Jun-2017	179.60	-24.09	222.41	6.1	64.81	12.00	0.33	0.19	-65.19	5.50	1.55	0.35
MM11	28-Jul-2018	116.51	-8.24	284.47	6.4	-19.66	12.00	0.17	0.14	-65.66	3.00	2.25	0.57
MM11	31-Oct-2017	169.15	-21.70	232.27	6.7	-53.35	19.50	1.73	0.68	-55.35	3.00	1.80	0.24
MM11	02-Apr-2018	-63.01	-20.66	117.11	6.8	-1.17	7.50	0.15	0.09	-49.17	1.50	1.90	0.19
MM11	05-Aug-2018	116.44	-8.26	284.53	6.9	-25.60	13.00	0.85	0.24	-45.60	13.50	1.10	0.39
MM11	10-Jan-2017	122.62	4.48	284.88	7.3	-11.33	90.00	0.25	2.00	-63.33	90.00	1.95	2
MM12	23-Aug-2016	122.54	-7.21	279.92	5.8	-76.18	22.00	1.27	0.35	-60.18	7.00	0.95	0.26
MM12	23-Aug-2016	122.43	-7.29	279.98	6	-74.12	20.50	1.25	0.36	-60.12	7.00	0.95	0.26
MM12	28-Jul-2018	122.73	-7.10	279.80	6	-58.30	4.50	1.02	0.08	-54.30	3.50	1.00	0.10
MM12	17-Jun-2017	179.60	-24.09	222.81	6.1	-70.80	26.00	0.95	0.34	-60.80	2.50	1.45	0.20

Continued on next page

Continued from previous page

MM12	20-Nov-2016	-68.63	-31.62	127.10	6.4	-23.16	13.50	1.93	0.85	-29.16	90.00	1.85	2
MM12	21-Feb-2017	-63.90	-19.28	117.63	6.5	-52.67	3.50	1.60	0.07	-40.67	4.50	1.50	0.23
MM12	31-Oct-2017	169.15	-21.70	232.66	6.7	81.04	14.50	0.70	0.27	-60.96	2.50	1.50	0.12
MM12	02-Apr-2018	-63.01	-20.66	117.48	6.8	-50.80	3.50	1.62	0.17	-50.80	2.50	1.65	0.21
MM13	23-Aug-2016	122.54	-7.21	279.84	5.8	-60.26	3.50	1.20	0.11	-60.26	2.00	1.20	0.10
MM13	15-Jul-2017	121.98	0.41	283.91	5.9	-38.26	14.00	0.42	0.22	-50.26	17.50	0.55	0.30
MM13	23-Aug-2016	122.43	-7.29	279.90	6	-60.20	3.50	1.20	0.11	-60.20	2.00	1.20	0.10
MM13	28-Jul-2018	122.73	-7.10	279.72	6	-60.37	6.50	1.05	0.16	-58.37	4.50	1.00	0.16
MM13	20-Nov-2016	-68.63	-31.62	127.02	6.4	-25.23	9.50	1.82	0.34	-23.23	9.50	1.85	0.44
MM13	21-Feb-2017	-63.90	-19.28	117.55	6.5	-58.74	40.00	1.73	0.11	-50.74	4.00	1.65	0.31
MM13	02-Apr-2018	-63.01	-20.66	117.40	6.8	-4.87	11.50	0.10	0.09	-52.87	1.50	1.80	0.16
MM13	10-Jan-2017	122.62	4.48	285.21	7.3	-17.00	90.00	0.40	2.00	-43.00	90.00	0.55	2
MM14	19-May-2019	169.58	-21.73	232.31	6	-43.30	9.50	2.20	0.18	-59.30	3.50	1.95	0.24
MM14	19-May-2019	169.78	-21.66	232.17	6.3	-65.44	20.00	1.35	0.32	-65.44	6.00	1.35	0.25
MM14	16-Oct-2018	169.49	-21.92	232.31	6.3	-67.31	10.00	1.27	0.23	-65.31	5.50	1.35	0.20
MM14	16-Sep-2018	178.20	-25.41	223.56	6.5	-64.06	4.50	1.27	0.16	-64.06	2.00	1.25	0.12
MM14	10-Sep-2018	-179.37	-31.74	219.28	6.9	-60.40	15.00	1.57	0.43	-64.40	2.50	1.30	0.21

Continued on next page

Continued from previous page

MM14	28-Jul-2018	122.73	-7.10	279.84	6	-46.26	9.50	0.80	0.15	-52.26	4.50	0.90	0.12
MM14	12-Jun-2018	98.59	-2.02	304.73	5.9	-85.51	8.50	1.38	0.27	-87.51	90.00	1.30	2
MM14	02-Apr-2018	-63.01	-20.66	117.51	6.8	-2.77	9.00	0.12	0.10	-50.77	3.50	1.85	0.31
MM14	15-Dec-2017	108.17	-7.49	293.10	6.5	-51.08	3.00	1.73	0.14	-55.08	15.50	1.75	0.65
MM14	17-Jun-2017	179.60	-24.09	222.84	6.1	65.23	8.50	0.45	0.10	-66.77	5.00	1.30	0.26
MM14	21-Feb-2017	-63.90	-19.28	117.65	6.5	-50.64	4.00	1.77	0.08	-42.64	6.00	1.80	0.25
MM14	05-Dec-2016	123.38	-7.32	279.15	6.3	-72.94	38.00	0.97	0.11	83.06	5.50	2.95	0.39
MM14	23-Aug-2016	122.54	-7.21	279.96	5.8	-58.14	15.00	0.93	0.22	-62.14	2.50	1.00	0.12
MM14	23-Aug-2016	122.43	-7.29	280.01	6	-58.09	16.50	0.93	0.24	-62.09	2.50	1.00	0.12
MM15	02-Apr-2018	-63.01	-20.66	117.50	6.8	1.23	8.50	0.07	0.06	-50.77	1.50	1.85	0.14
MM15	17-Jun-2017	179.60	-24.09	222.84	6.1	-70.77	18.00	1.27	0.37	-64.77	3.00	1.45	0.17
MM15	21-Feb-2017	-63.90	-19.28	117.65	6.5	-52.64	40.00	1.68	0.12	-48.64	4.50	1.65	0.29
MM15	10-Jan-2017	122.62	4.48	285.32	7.3	-22.89	23.00	0.47	0.49	-52.89	90.00	0.75	2
MM15	20-Nov-2016	-68.63	-31.62	127.12	6.4	-35.14	33.00	2.30	0.33	-29.14	10.00	2.15	0.64
MM15	23-Aug-2016	122.54	-7.21	279.96	5.8	-14.14	11.50	0.28	0.11	-62.14	2.50	1.25	0.15
MM15	23-Aug-2016	122.43	-7.29	280.01	6	-14.08	22.50	0.28	0.39	-62.08	3.00	1.25	0.19
MM15	04-Aug-2016	-66.01	-22.33	120.79	6.2	-13.51	90.00	0.05	2.00	-47.51	90.00	1.70	2

Continued on next page

Continued from previous page

MM16	15-Jul-2017	121.98	0.41	284.19	5.9	-31.99	10.50	0.25	0.14	-55.99	90.00	0.40	2
MM16	17-Jun-2017	179.60	-24.09	222.99	6.1	75.39	11.50	0.42	0.18	-64.61	90.00	1.00	2
MM16	23-Aug-2016	122.54	-7.21	280.13	5.8	-43.97	10.00	0.60	0.12	-57.97	5.00	0.80	0.14
MM16	23-Aug-2016	122.43	-7.29	280.19	6	-43.91	12.50	0.60	0.16	-57.91	5.00	0.80	0.14
MM17	23-Aug-2016	122.54	-7.21	280.41	5.8	-69.69	5.00	1.10	0.14	-65.69	4.00	1.00	0.20
MM17	23-Aug-2016	122.43	-7.29	280.47	6	-69.63	4.00	1.10	0.12	-65.63	4.00	1.00	0.21
MM17	28-Jul-2018	122.73	-7.10	280.30	6	-23.81	8.00	0.15	0.09	-69.81	24.50	1.10	0.99
MM17	17-Jun-2017	179.60	-24.09	223.25	6.1	-54.35	9.50	1.68	0.16	-72.35	11.00	1.55	0.53
MM17	20-Nov-2016	-68.63	-31.62	127.48	6.4	-14.79	11.50	0.28	0.19	-38.79	90.00	0.75	2
MM18	17-Jun-2017	179.60	-24.09	223.44	6.1	-70.16	24.50	1.48	0.47	-66.16	4.00	1.55	0.26
MM18	29-Dec-2016	118.66	-9.03	283.31	6.3	-84.81	28.00	1.93	0.14	-64.81	3.00	2.10	0.29
MM18	23-Aug-2016	122.54	-7.21	280.64	5.8	68.54	7.00	0.07	0.06	-71.46	3.50	1.90	0.76
MM18	23-Aug-2016	122.43	-7.29	280.70	6	68.60	8.00	0.07	0.06	-71.40	3.00	1.90	0.38
MM19	17-Jun-2017	179.60	-24.09	223.66	6.1	-81.95	5.50	1.20	0.11	-75.95	4.00	1.30	0.14
MM19	04-Aug-2016	-66.01	-22.33	121.52	6.2	87.22	7.00	0.28	0.09	-80.78	21.50	0.40	0.28
MM21	02-Apr-2018	-63.01	-20.66	118.53	6.8	76.24	11.00	0.50	0.14	50.24	11.50	0.85	0.30
MM22	19-May-2019	169.78	-21.66	233.45	6.3	-86.19	12.00	1.43	0.14	-84.19	5.50	1.40	0.17

Continued on next page

Continued from previous page

MM22	16-Oct-2018	169.49	-21.92	233.59	6.3	-80.05	11.00	1.32	0.22	-76.05	5.00	1.40	0.14
MM22	16-Sep-2018	178.20	-25.41	224.82	6.5	85.19	6.50	1.38	0.12	-86.81	4.00	1.45	0.14
MM22	10-Sep-2018	-179.37	-31.74	220.53	6.9	-71.16	11.00	1.68	0.36	-77.16	4.50	1.50	0.20
MM22	02-Apr-2018	-63.01	-20.66	118.60	6.8	74.32	11.00	0.55	0.15	54.32	8.50	0.85	0.19
MM23	28-Jul-2018	116.51	-8.24	286.71	6.4	50.57	10.50	1.50	0.21	58.57	10.50	1.45	0.33
MM23	28-Jul-2018	122.73	-7.10	281.51	6	81.40	6.00	1.55	0.12	71.40	5.50	1.50	0.25
MM23	02-Apr-2018	-63.01	-20.66	118.75	6.8	84.47	9.50	0.62	0.15	86.47	12.50	0.65	0.20
MM23	10-Jan-2017	122.62	4.48	286.81	7.3	68.58	5.50	1.15	0.11	60.58	10.50	1.10	0.24
MM23	23-Aug-2016	122.54	-7.21	281.63	5.8	67.52	8.00	2.25	0.29	65.52	8.00	2.50	0.54
MM23	23-Aug-2016	122.43	-7.29	281.69	6	71.58	9.50	2.10	0.33	67.58	11.00	2.30	0.68
MM24	28-Jul-2018	122.73	-7.10	281.76	6	81.64	5.00	1.23	0.12	75.64	4.00	1.15	0.15
MM24	15-Dec-2017	108.17	-7.49	295.20	6.5	69.02	4.50	0.68	0.06	61.02	7.00	0.70	0.11
MM24	20-Nov-2016	-68.63	-31.62	128.39	6.4	88.13	8.50	0.40	0.12	68.13	18.00	0.50	0.35
MM25	05-Aug-2018	116.44	-8.26	287.18	6.9	61.04	7.50	1.45	0.19	65.04	6.00	1.50	0.21
MM25	28-Jul-2018	116.51	-8.24	287.13	6.4	72.98	8.50	1.50	0.19	68.98	6.00	1.35	0.17
MM25	28-Jul-2018	122.73	-7.10	281.91	6	63.79	3.50	1.23	0.06	63.79	2.50	1.20	0.09
MM25	02-Apr-2018	-63.01	-20.66	119.08	6.8	68.78	9.00	0.53	0.11	56.78	8.00	0.65	0.12

Continued on next page

Continued from previous page

MM26	05-Dec-2016	123.38	-7.32	281.44	6.3	35.32	11.50	0.82	0.12	55.32	12.50	0.75	0.19
MM26	23-Aug-2016	122.54	-7.21	282.25	5.8	52.13	9.00	0.80	0.10	52.13	8.00	0.80	0.12
MM26	23-Aug-2016	122.43	-7.29	282.31	6	52.20	9.00	0.80	0.10	52.20	9.00	0.80	0.15
MM27	16-Sep-2018	178.20	-25.41	225.55	6.5	-88.09	13.50	0.68	0.19	71.91	7.00	0.95	0.20
MM27	28-Jul-2018	122.73	-7.10	282.15	6	72.03	6.50	0.93	0.08	58.03	8.00	0.95	0.16
MM27	12-Aug-2017	-72.16	-30.24	130.92	5.8	84.63	7.50	0.65	0.19	64.63	10.50	1.00	0.34
MM27	15-Jul-2017	121.98	0.41	286.18	5.9	61.99	8.50	0.97	0.13	51.99	6.00	1.05	0.15
MM27	17-Jun-2017	179.60	-24.09	224.82	6.1	67.20	10.50	1.20	0.24	69.20	5.00	1.25	0.24
MM27	21-Feb-2017	-63.90	-19.28	119.43	6.5	51.12	16.00	1.23	0.35	53.12	4.00	1.25	0.16
MM27	23-Aug-2016	122.54	-7.21	282.27	5.8	70.15	9.00	0.95	0.07	56.15	5.50	1.00	0.12
MM27	23-Aug-2016	122.43	-7.29	282.33	6	74.21	7.50	0.95	0.06	56.21	5.00	1.00	0.11
MM27	07-Jun-2016	126.37	1.28	282.59	6.3	62.42	9.50	0.95	0.14	56.42	13.00	0.95	0.25
MM27	05-Jun-2016	125.63	-4.59	280.65	6.3	48.53	10.00	0.78	0.13	42.53	9.00	0.85	0.19
MM27	01-Jun-2016	100.67	-2.10	305.18	6.6	54.94	4.00	1.40	0.20	50.94	3.50	1.75	0.25
MM29	28-Jul-2018	122.73	-7.10	283.62	6	85.49	7.50	1.30	0.19	75.49	7.50	1.15	0.26
MM29	13-Jul-2018	169.05	-18.93	237.20	6.4	-80.45	16.50	1.25	0.49	-76.45	15.50	1.35	0.46
MM29	15-Dec-2017	108.17	-7.49	297.23	6.5	81.04	6.00	0.82	0.11	75.04	4.50	0.85	0.07

Continued on next page

Continued from previous page

MM29	02-Apr-2018	-63.01	-20.66	120.40	6.8	-77.90	8.00	0.97	0.20	-87.90	13.00	0.70	0.24
MM29	10-Jan-2017	122.62	4.48	288.71	7.3	74.47	11.00	0.80	0.17	52.47	16.00	0.90	0.40
MM30	23-Aug-2016	122.54	-7.21	283.77	5.8	43.64	5.50	1.12	0.11	43.64	3.50	1.10	0.12
MM30	23-Aug-2016	122.43	-7.29	283.83	6	43.70	4.50	1.10	0.09	43.70	3.00	1.10	0.11
MM32	17-Jun-2017	179.60	-24.09	226.51	6.1	48.87	28.50	1.18	0.57	-89.13	90.00	1.00	2
MM32	28-Jul-2018	116.51	-8.24	289.52	6.4	55.36	10.50	0.85	0.22	39.36	10.00	1.35	0.49
MM32	26-Sep-2017	-176.84	-23.58	223.59	6.4	-66.02	9.00	1.68	0.12	-84.02	7.00	1.60	0.28
MM32	13-Jul-2018	169.05	-18.93	237.61	6.4	-88.05	8.50	1.25	0.21	-84.05	9.50	1.25	0.20
MM32	20-Sep-2017	169.09	-18.79	237.62	6.4	85.97	8.00	1.27	0.26	77.97	9.50	1.70	0.50
MM32	05-Aug-2018	116.44	-8.26	289.58	6.9	67.42	13.50	0.53	0.21	53.42	16.50	0.60	0.25
MM32	10-Jan-2017	122.62	4.48	289.12	7.3	60.88	11.00	1.02	0.24	62.88	9.00	1.00	0.17
MM33	17-Aug-2018	119.80	-7.37	287.40	6.5	41.25	12.00	1.40	0.31	47.25	9.00	1.30	0.31
MM33	28-Jul-2018	122.73	-7.10	284.78	6	62.64	12.00	0.68	0.16	76.64	9.00	0.85	0.21
MM33	13-Jul-2018	169.05	-18.93	238.17	6.4	88.51	8.50	1.23	0.18	-81.49	10.00	1.10	0.19
MM33	12-Jun-2018	98.59	-2.02	310.08	5.9	79.83	11.00	0.53	0.32	-62.17	6.00	2.45	0.75
MM33	02-Apr-2018	-63.01	-20.66	121.19	6.8	70.88	9.50	0.57	0.11	56.88	7.50	0.75	0.15
MM33	24-Oct-2017	123.07	-7.22	284.40	6.7	62.27	14.50	0.55	0.29	60.27	90.00	0.65	2

Continued on next page

Continued from previous page

MM33	20-Nov-2016	-68.63	-31.62	130.31	6.4	-85.95	12.50	0.23	0.14	52.05	16.50	0.95	0.50
MM34	02-Apr-2018	-63.01	-20.66	121.07	6.8	74.77	15.00	0.33	0.19	50.77	18.50	0.55	0.31
MM34	15-Dec-2017	108.17	-7.49	298.42	6.5	78.22	12.00	0.57	0.17	56.22	17.00	0.70	0.47
MM34	24-Apr-2017	-72.06	-33.04	133.56	6.9	89.29	10.00	0.00	0.03	-48.71	90.00	2.70	2
MM34	24-Feb-2017	-178.80	-23.26	225.87	6.9	-87.76	12.50	0.80	0.19	72.24	2.50	1.20	0.11
MM34	10-Jan-2017	122.62	4.48	289.60	7.3	55.35	16.50	0.75	0.40	51.35	90.00	0.80	2
MM34	24-Sep-2016	-178.24	-19.78	226.54	6.9	-85.05	12.50	0.88	0.23	74.95	11.50	1.40	0.56
MM34	23-Aug-2016	122.54	-7.21	284.81	5.8	36.68	14.50	0.97	0.15	54.68	14.50	0.95	0.29
MM34	23-Aug-2016	122.43	-7.29	284.88	6	34.74	15.50	0.97	0.15	58.74	12.00	0.95	0.23
MM35	10-Jan-2017	122.62	4.48	290.18	7.3	57.92	12.50	0.60	0.22	39.92	13.50	0.95	0.41
MM35	21-Dec-2016	127.92	-7.51	280.28	6.7	76.18	30.00	0.95	0.25	36.18	7.50	1.90	0.50
MM36	17-Aug-2018	119.80	-7.37	287.99	6.5	47.83	90.00	1.23	2.00	63.83	8.00	1.25	0.19
MM36	02-Apr-2018	-176.89	-24.72	224.31	6.1	70.68	25.50	1.45	0.32	82.68	9.50	1.35	0.26
MM36	15-Dec-2017	108.17	-7.49	299.14	6.5	60.94	11.00	1.02	0.19	66.94	11.00	1.00	0.25
MM38	07-Apr-2018	142.53	-5.84	268.83	6.3	16.84	13.50	1.05	0.25	16.84	3.00	1.05	0.12
MM38	10-Jan-2017	122.62	4.48	291.29	7.3	69.03	7.50	0.28	0.11	29.03	90.00	1.10	2
MM39	12-Jun-2018	98.59	-2.02	312.56	5.9	-87.69	7.50	0.60	0.14	60.31	12.50	1.30	0.55

Continued on next page

Continued from previous page

MM39	24-Oct-2017	123.07	-7.22	286.73	6.7	-25.42	7.50	2.27	0.21	-19.42	4.50	2.90	0.29
MM39	15-Jul-2017	121.98	0.41	290.81	5.9	72.57	7.50	0.85	0.18	56.57	16.50	1.05	0.41
MM39	09-May-2017	167.38	-14.59	243.36	6.8	77.68	2.00	1.32	0.15	75.68	1.00	1.45	0.11
MM39	24-Apr-2017	-72.06	-33.04	135.24	6.9	-77.03	16.50	0.50	0.34	-79.03	22.00	0.50	0.57
MM39	24-Feb-2017	-178.80	-23.26	227.97	6.9	-59.67	11.50	0.57	0.10	70.33	3.50	1.50	0.20
MM39	18-Feb-2017	-66.66	-23.86	127.35	6.4	15.02	7.00	0.05	0.08	-38.98	3.00	2.45	0.28
MM40	28-Jul-2018	116.51	-8.24	293.54	6.4	69.35	5.00	0.95	0.12	79.35	13.50	1.05	0.36
MM40	02-Apr-2018	-63.01	-20.66	123.69	6.8	69.37	10.50	0.60	0.12	67.37	4.50	0.65	0.07
MM40	25-Mar-2018	129.82	-6.63	281.56	6.4	53.44	18.50	1.45	0.34	49.44	10.50	1.45	0.36
MM40	15-Dec-2017	108.17	-7.49	302.02	6.5	61.81	4.50	0.88	0.06	67.81	3.50	0.85	0.06
MM40	26-Sep-2017	-176.84	-23.58	226.95	6.4	49.31	40.00	0.10	0.07	73.31	5.00	1.70	0.21
MM40	19-Aug-2017	-178.84	-17.96	230.57	6.4	82.97	5.00	1.60	0.14	76.97	2.00	1.75	0.09
MM40	15-Jul-2017	121.98	0.41	291.68	5.9	67.44	7.50	1.07	0.12	55.44	5.50	1.20	0.17
MM40	09-May-2017	167.38	-14.59	244.17	6.8	-55.52	7.50	0.15	0.07	76.48	1.00	1.70	0.11
MM40	05-Dec-2016	123.38	-7.32	287.33	6.3	61.17	4.50	0.95	0.06	55.17	3.00	1.00	0.06
MM40	23-Aug-2016	122.54	-7.21	288.17	5.8	58.01	6.50	0.90	0.07	58.01	5.00	0.90	0.10
MM40	23-Aug-2016	122.43	-7.29	288.24	6	60.08	5.00	0.88	0.06	58.08	6.00	0.90	0.12

A.2 Figures

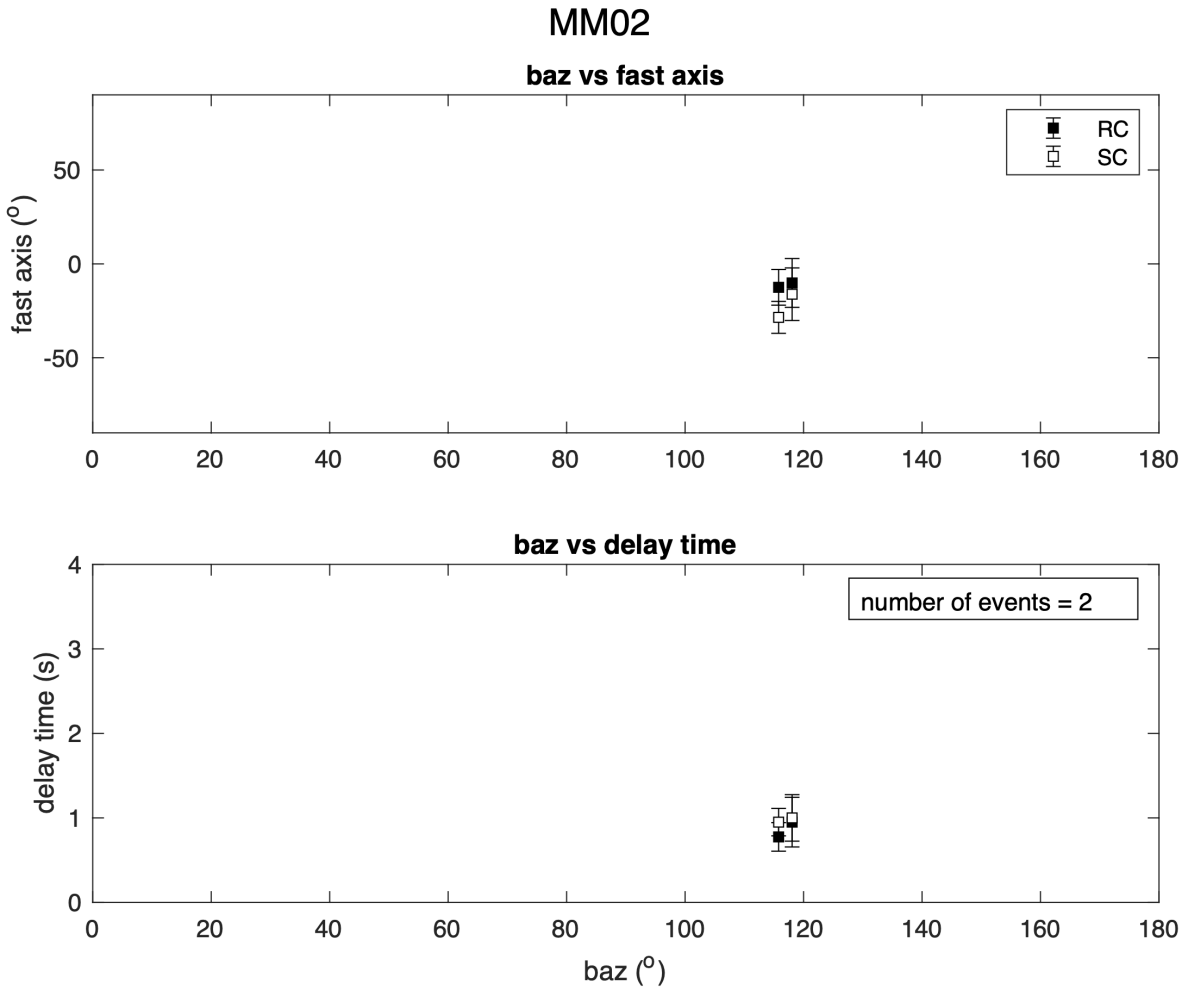

Figure A.1: Individual station results for MM02. Black squares denote results computed for the rotation correlation method (*Bowman and Ando*, 1987), white squares denote results computed from the transverse energy minimization method (*Silver and Chan*, 1991).

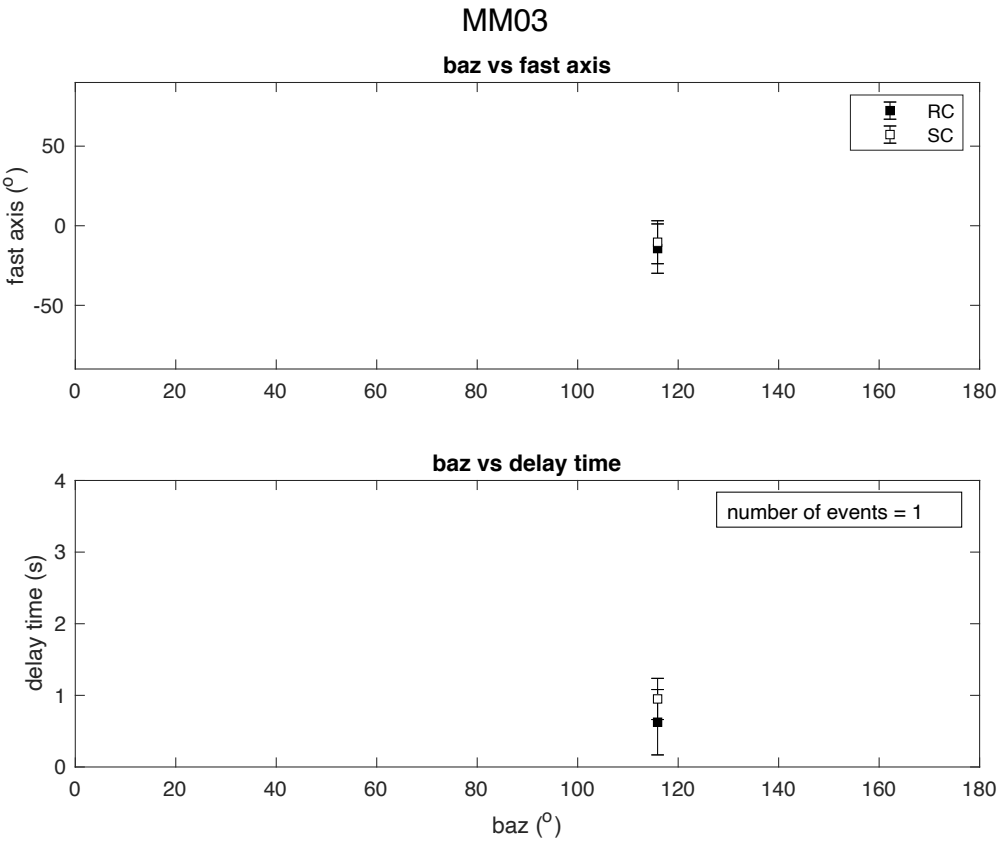

Figure A.2: Individual station results for MM03. Same notation as Figure A.1.

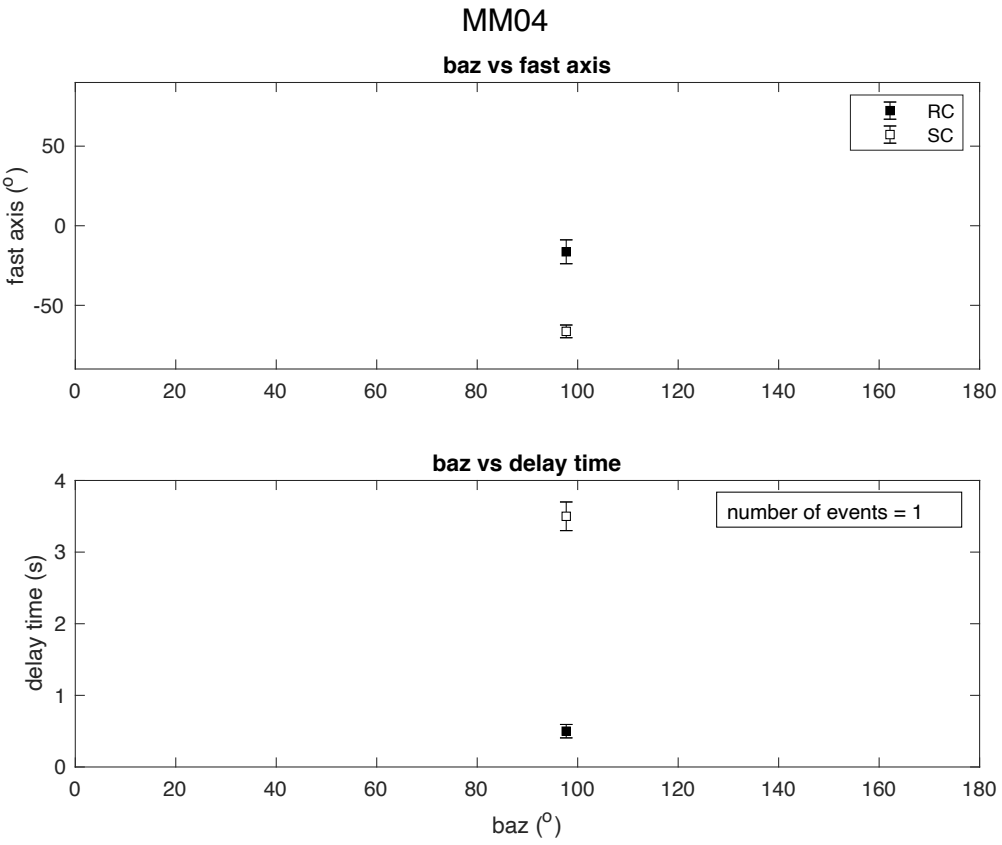

Figure A.3: Individual station results for MM04. Same notation as Figure A.1.

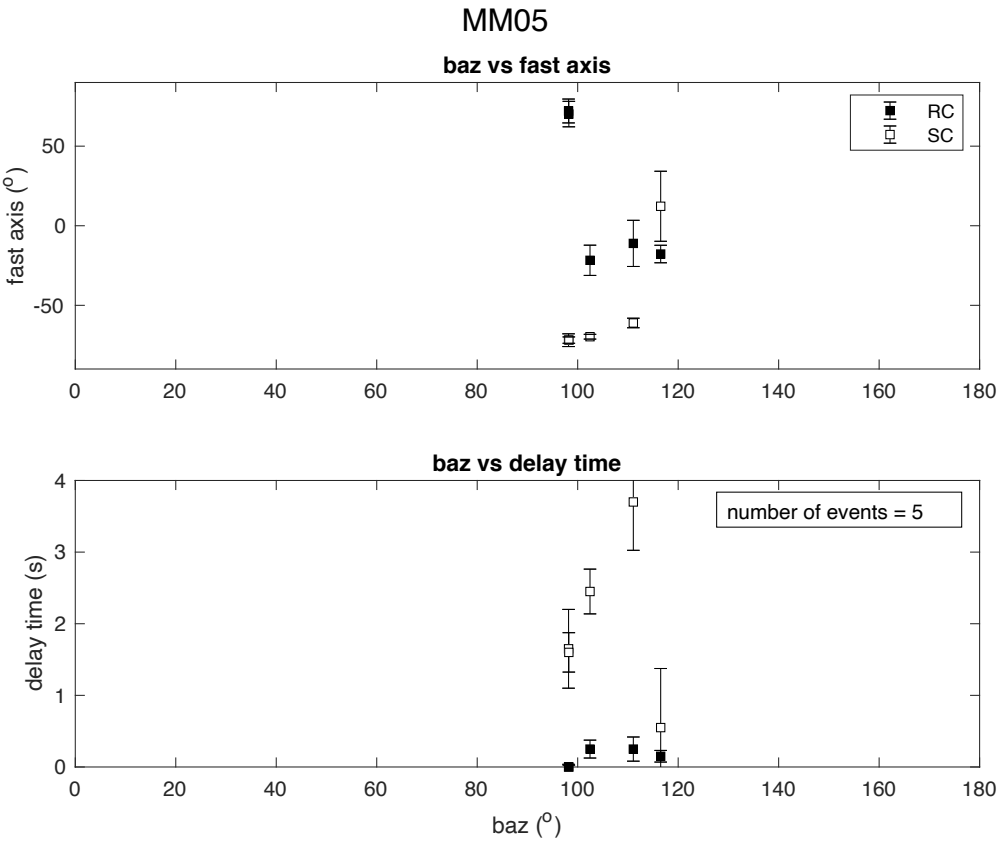

Figure A.4: Individual station results for MM05. Same notation as Figure A.1.

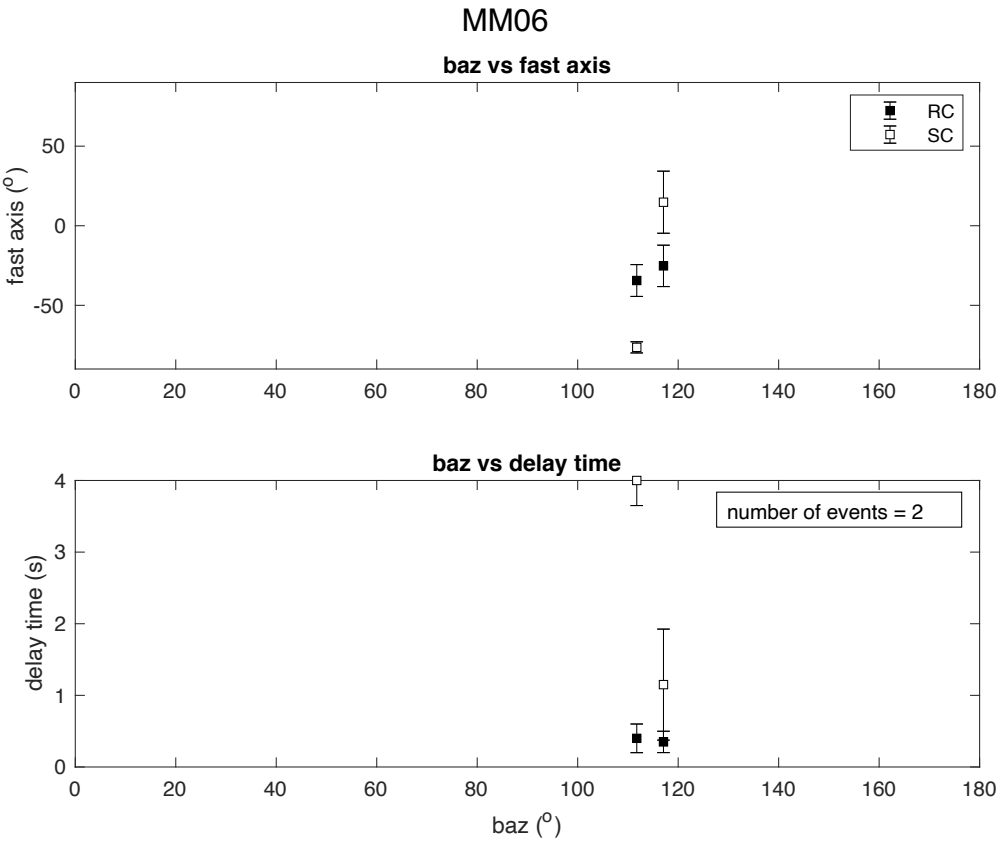

Figure A.5: Individual station results for MM06. Same notation as Figure A.1.

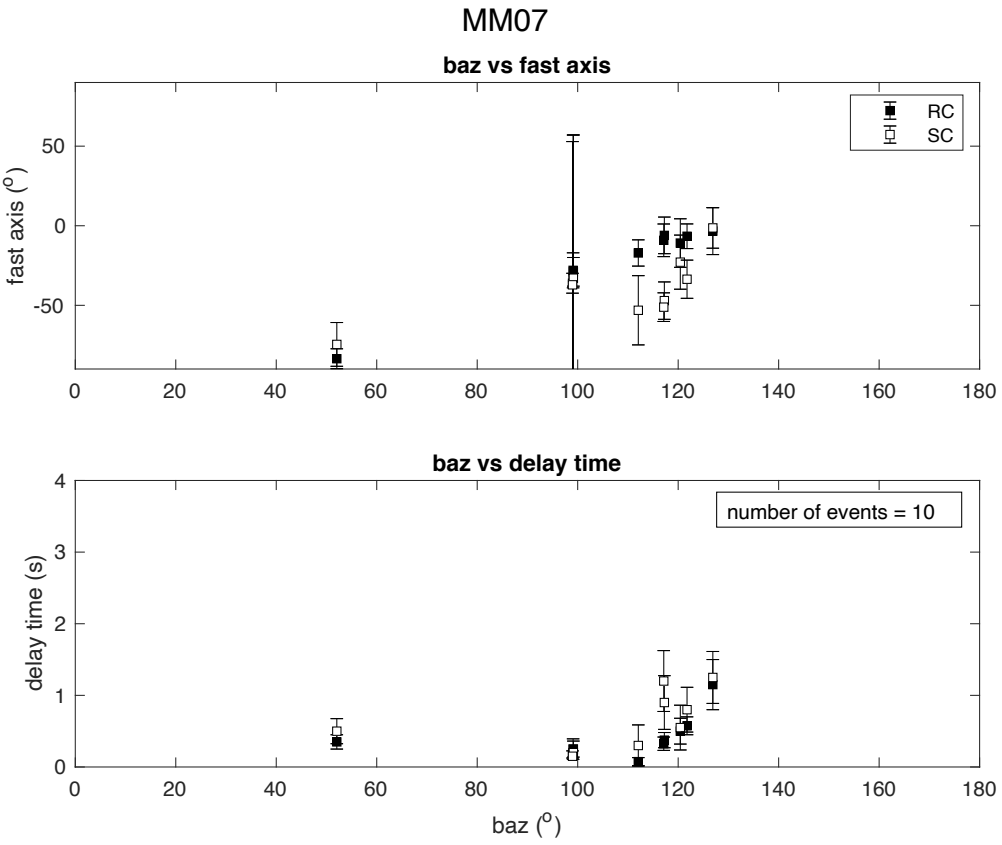

Figure A.6: Individual station results for MM07. Same notation as Figure A.1.

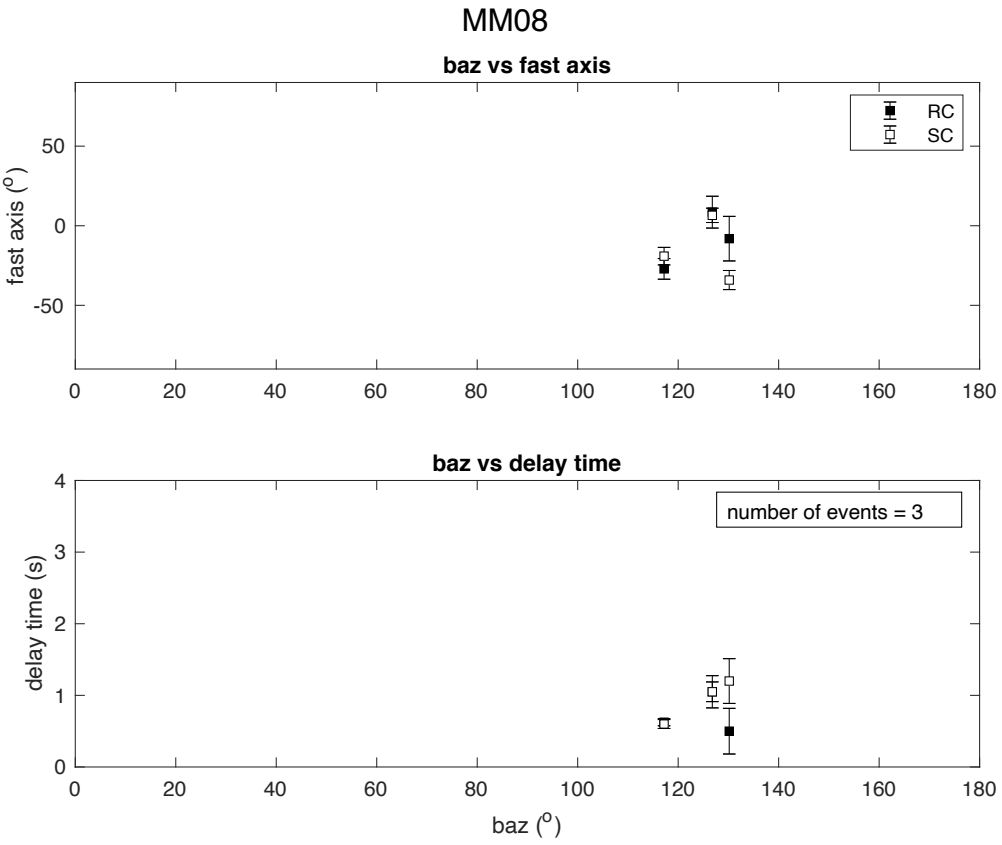

Figure A.7: Individual station results for MM08. Same notation as Figure A.1.

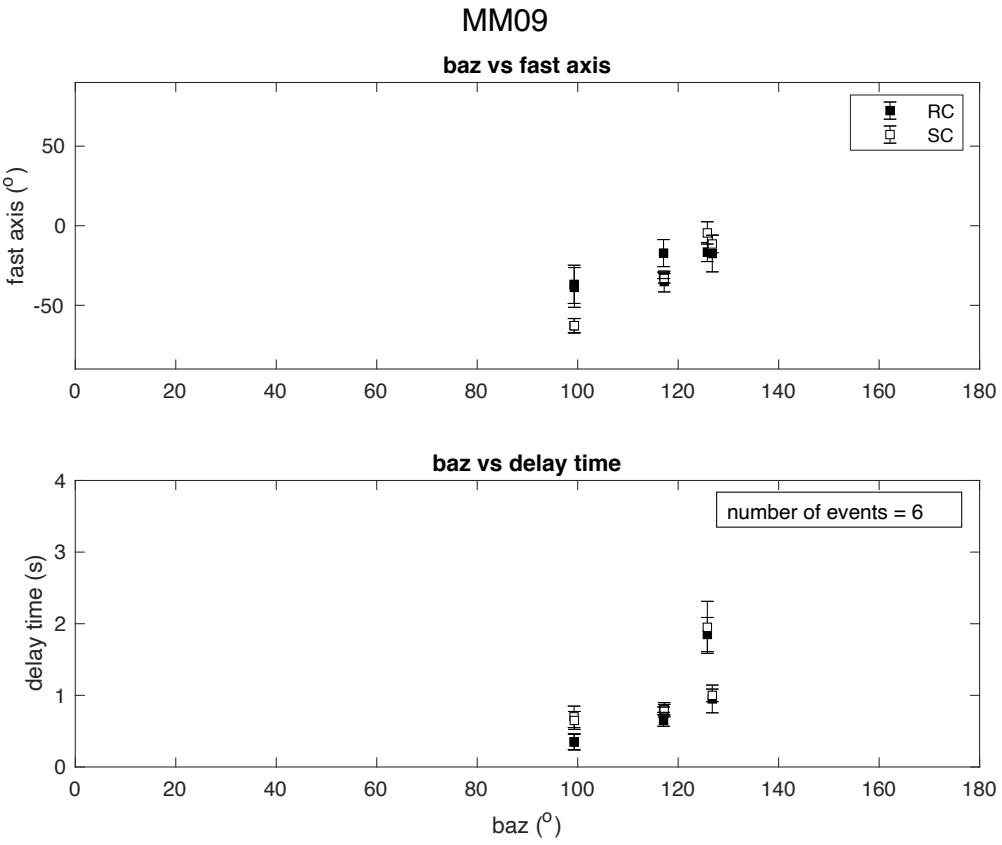

Figure A.8: Individual station results for MM09. Same notation as Figure A.1.

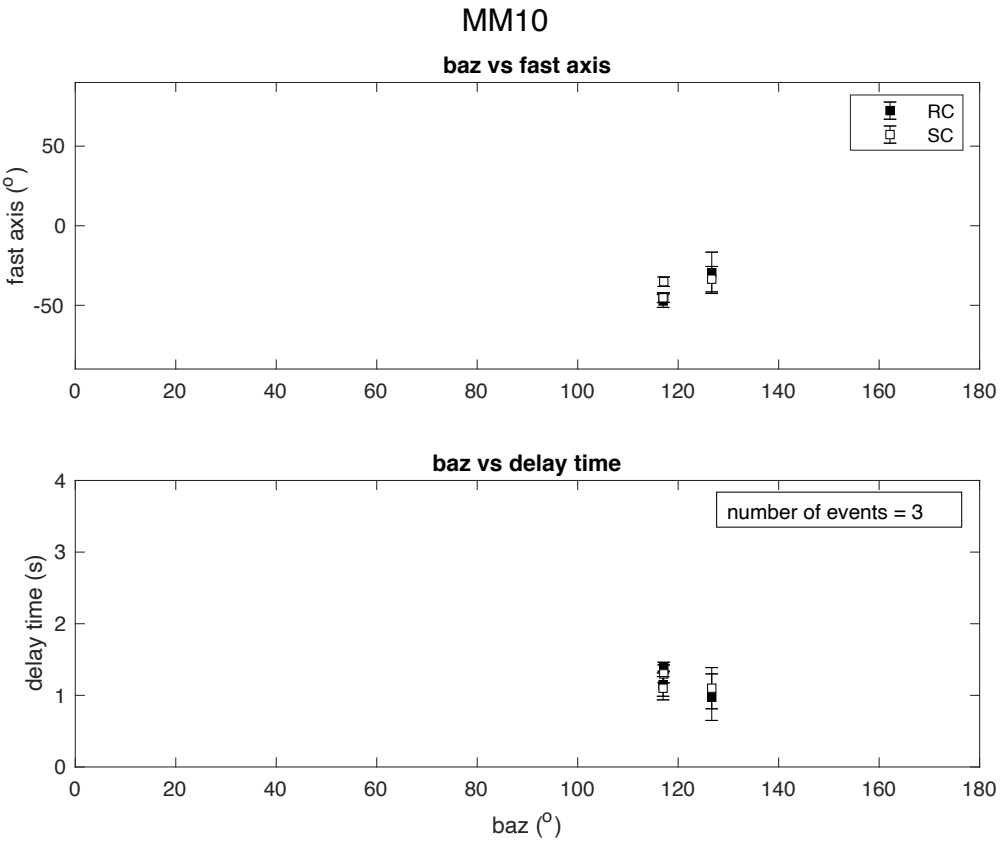

Figure A.9: Individual station results for MM10. Same notation as Figure A.1.

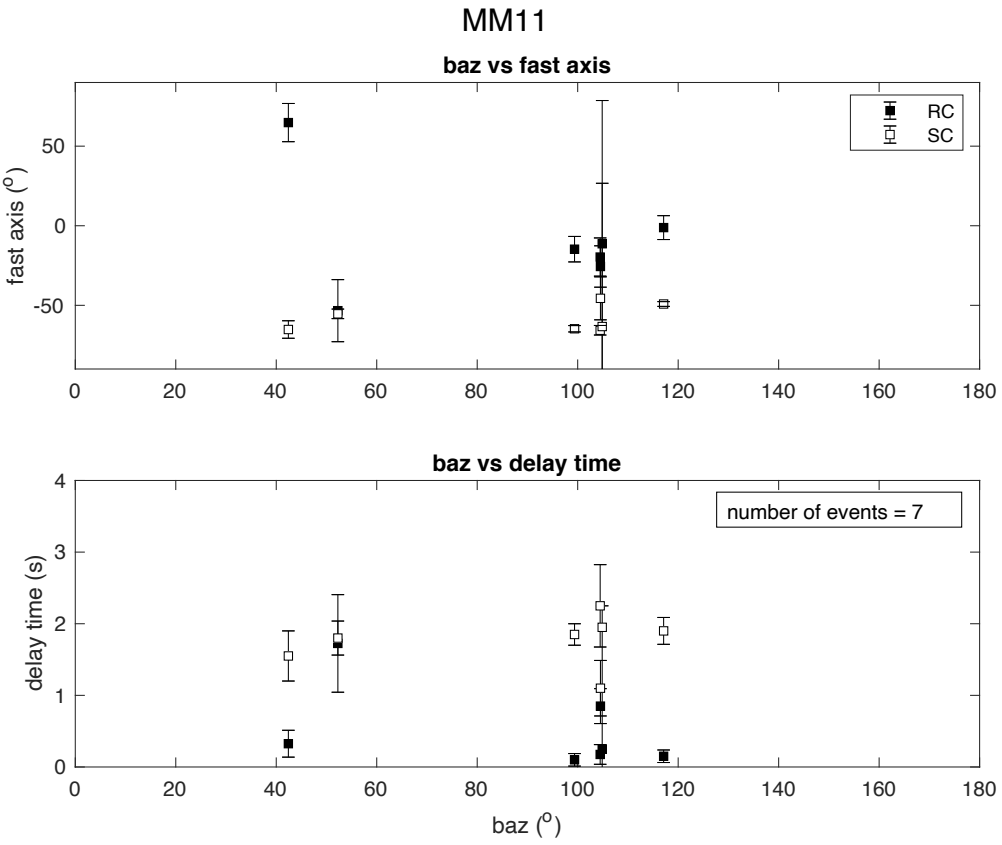

Figure A.10: Individual station results for MM11. Same notation as Figure A.1.

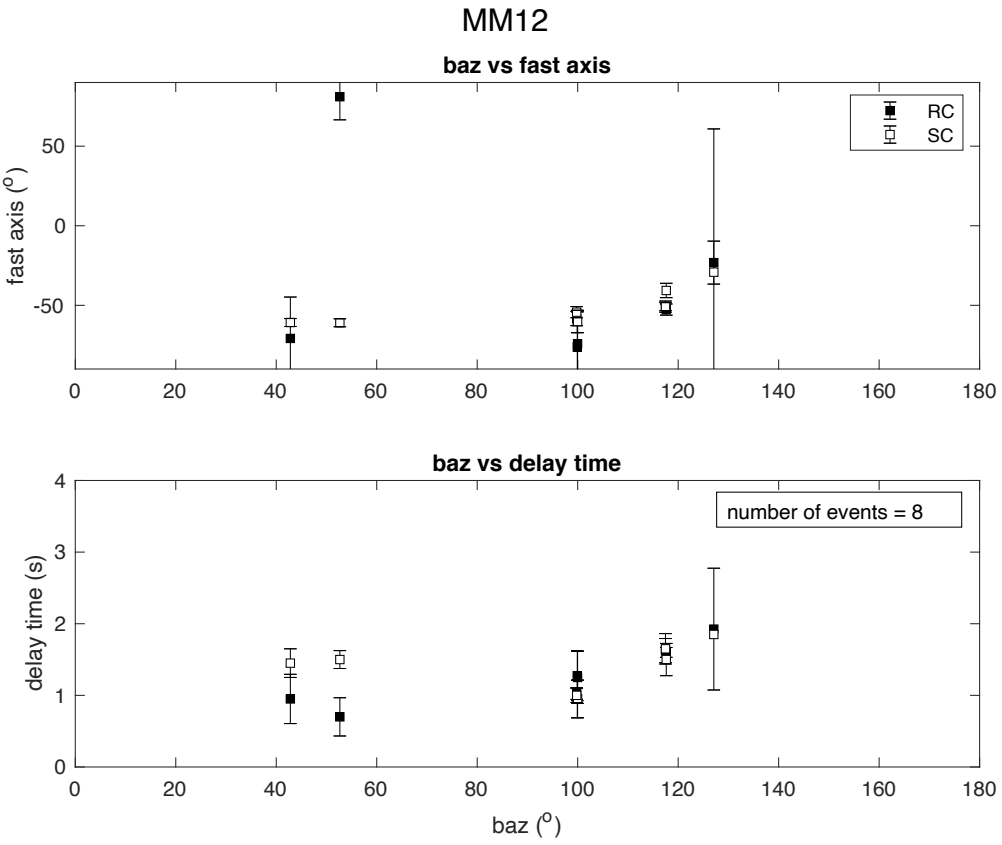

Figure A.11: Individual station results for MM12. Same notation as Figure A.1.

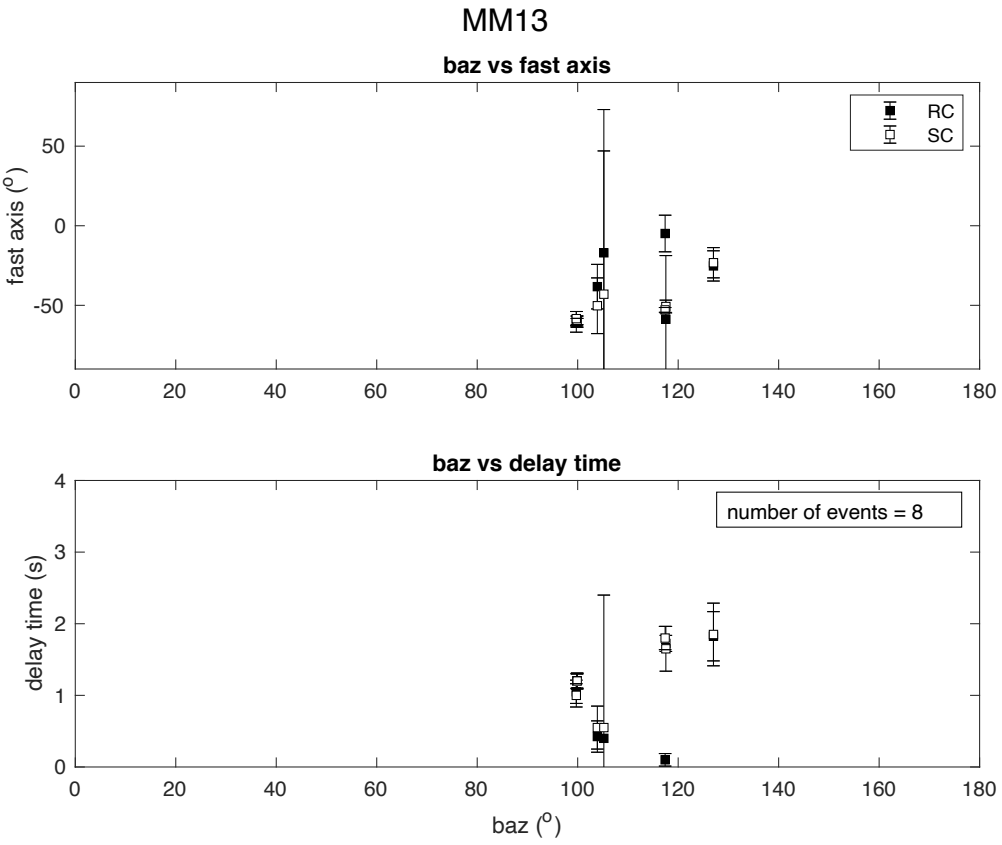

Figure A.12: Individual station results for MM13. Same notation as Figure A.1.

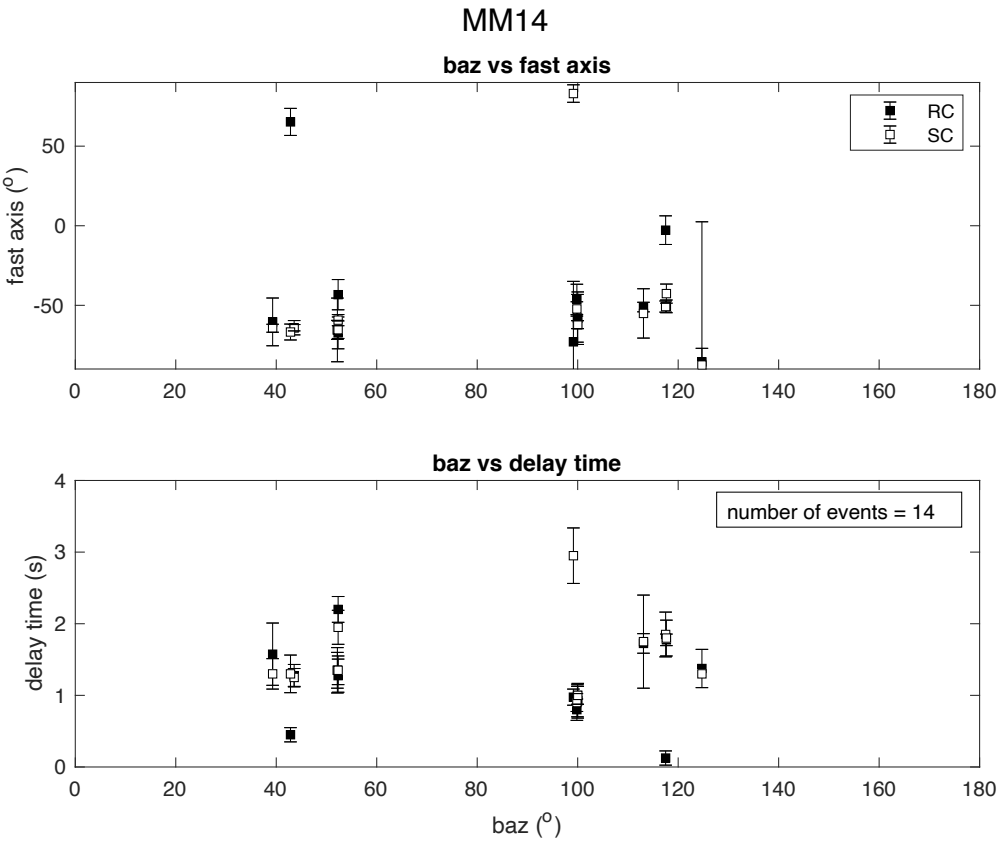

Figure A.13: Individual station results for MM14. Same notation as Figure A.1.

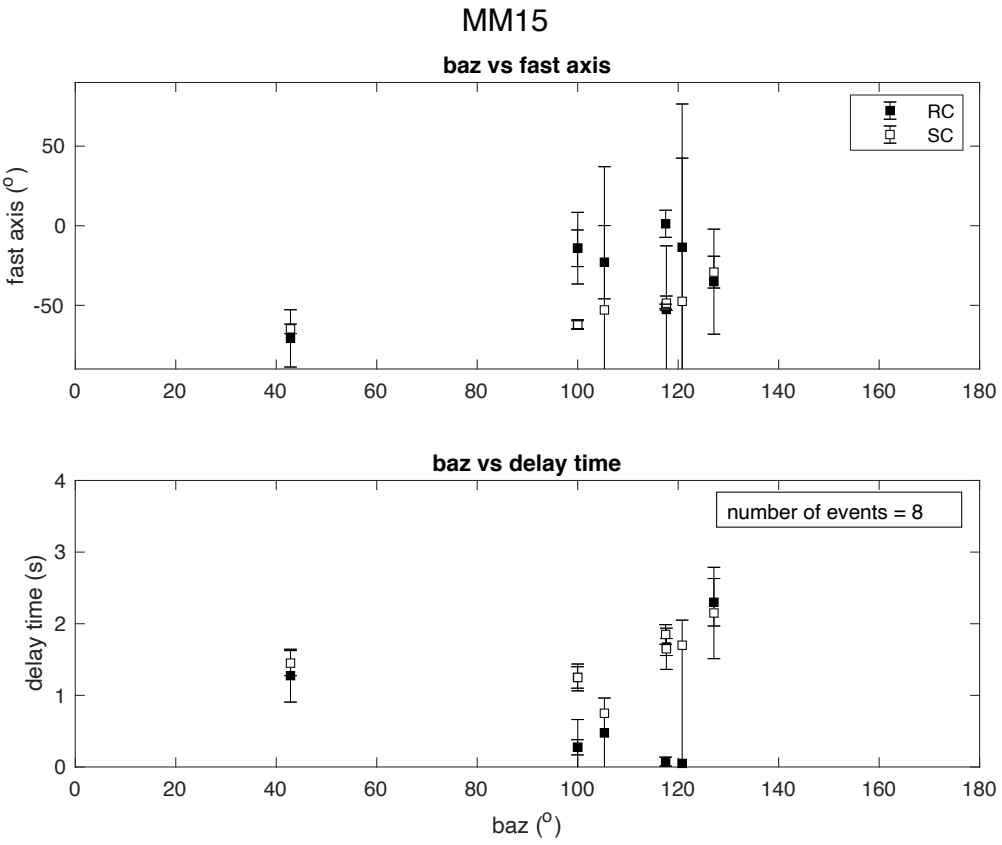

Figure A.14: Individual station results for MM15. Same notation as Figure A.1.

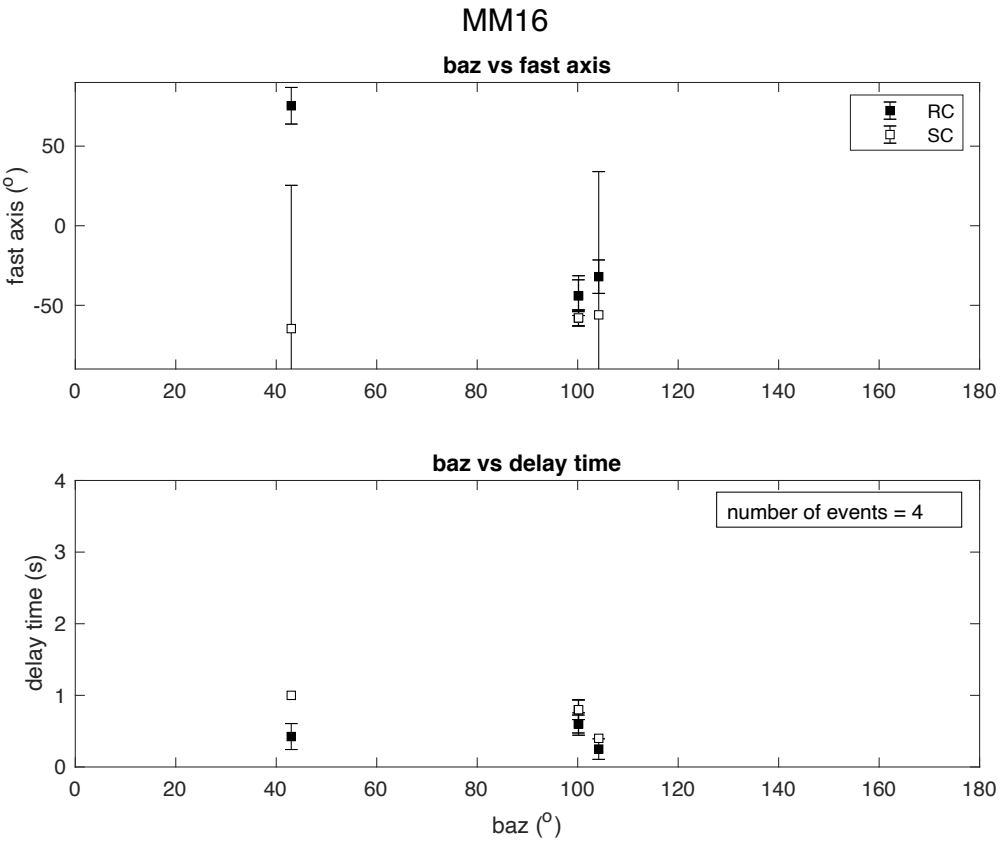

Figure A.15: Individual station results for MM16. Same notation as Figure A.1.

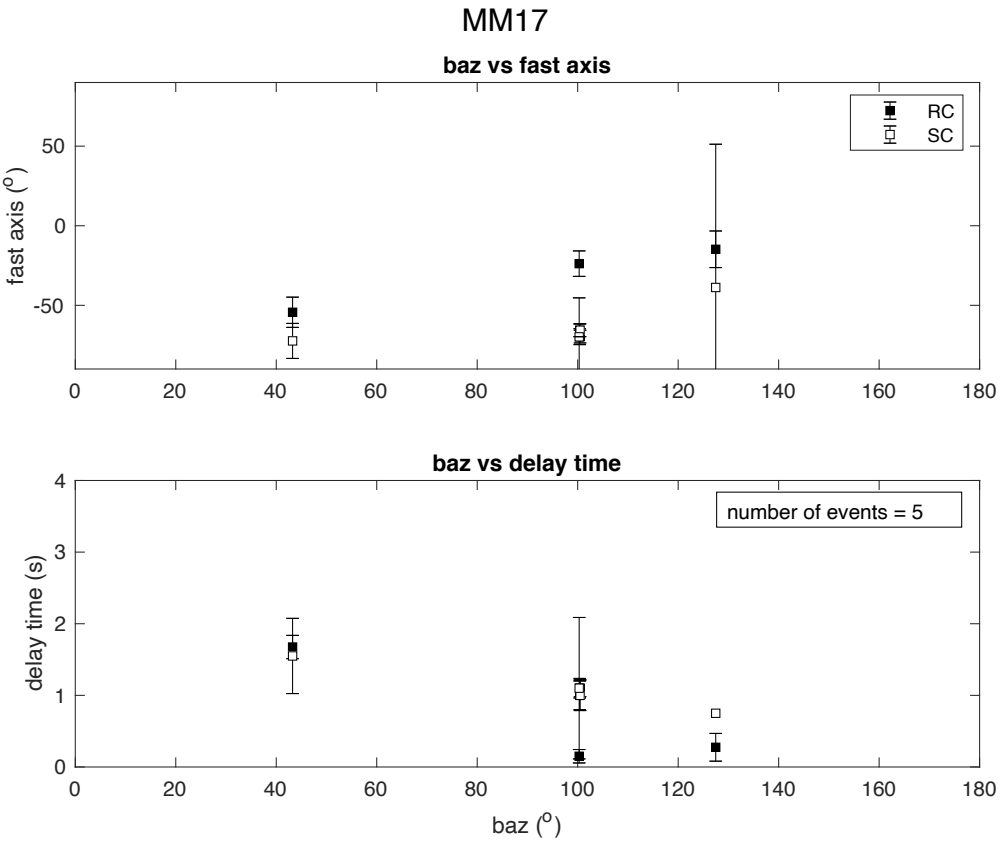

Figure A.16: Individual station results for MM17. Same notation as Figure A.1.

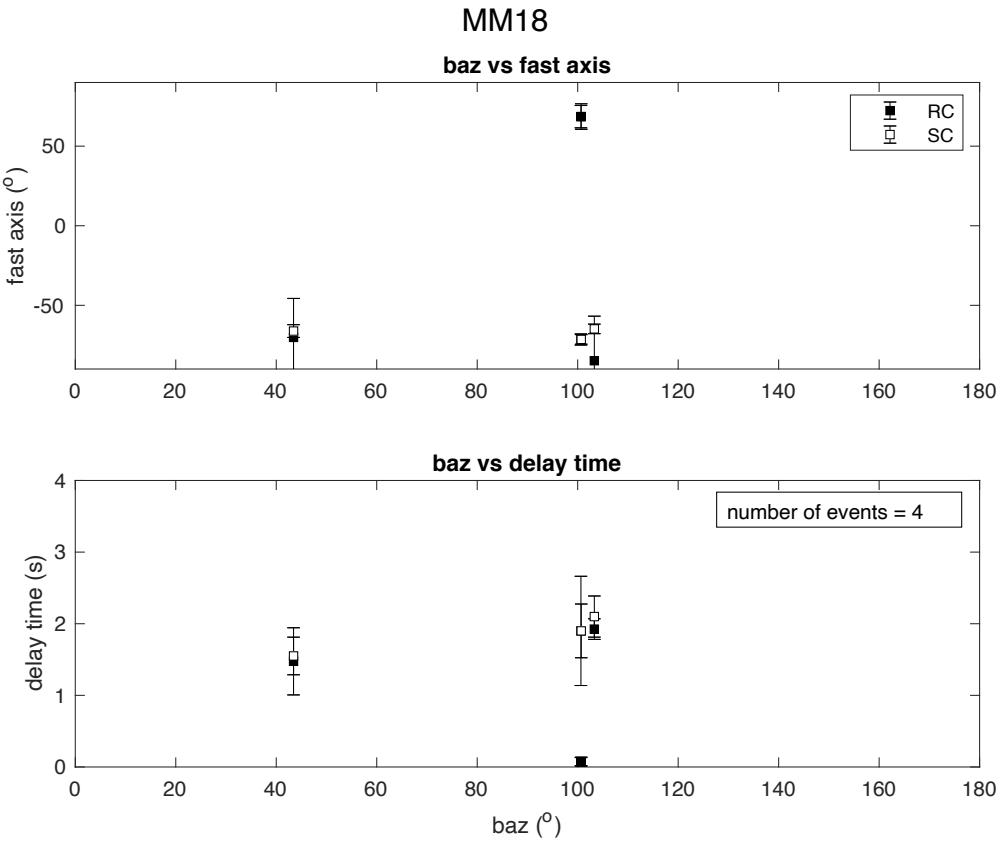

Figure A.17: Individual station results for MM18. Same notation as Figure A.1.

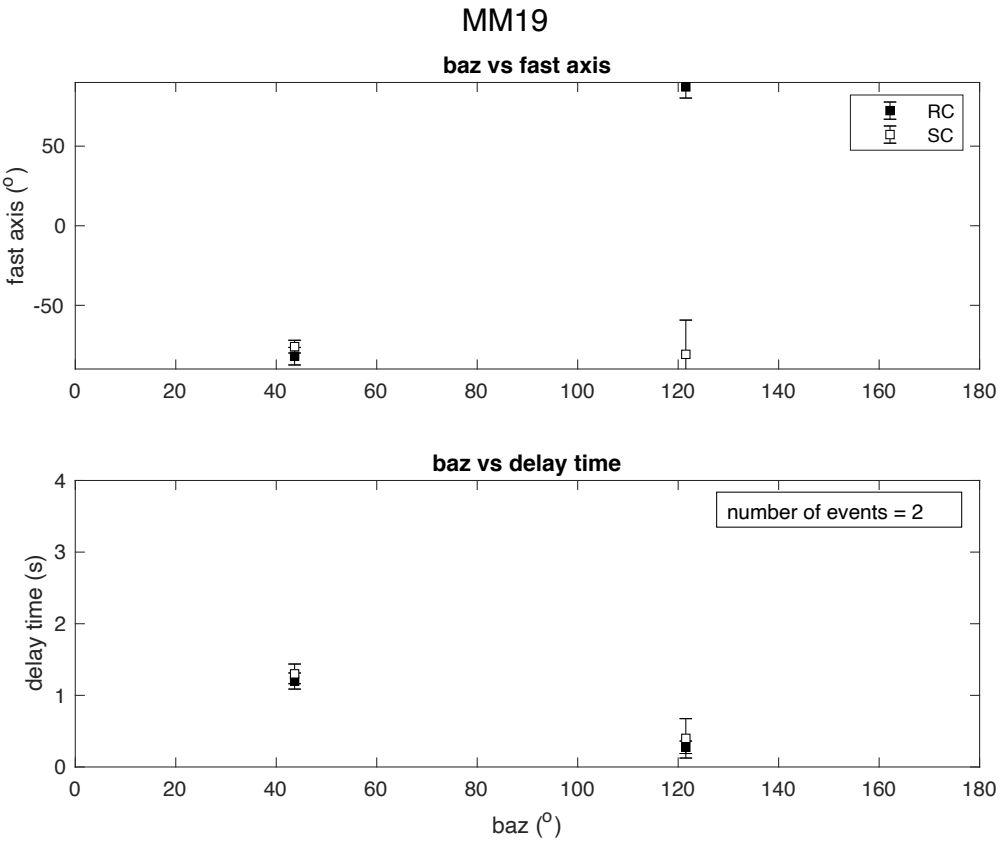

Figure A.18: Individual station results for MM19. Same notation as Figure A.1.

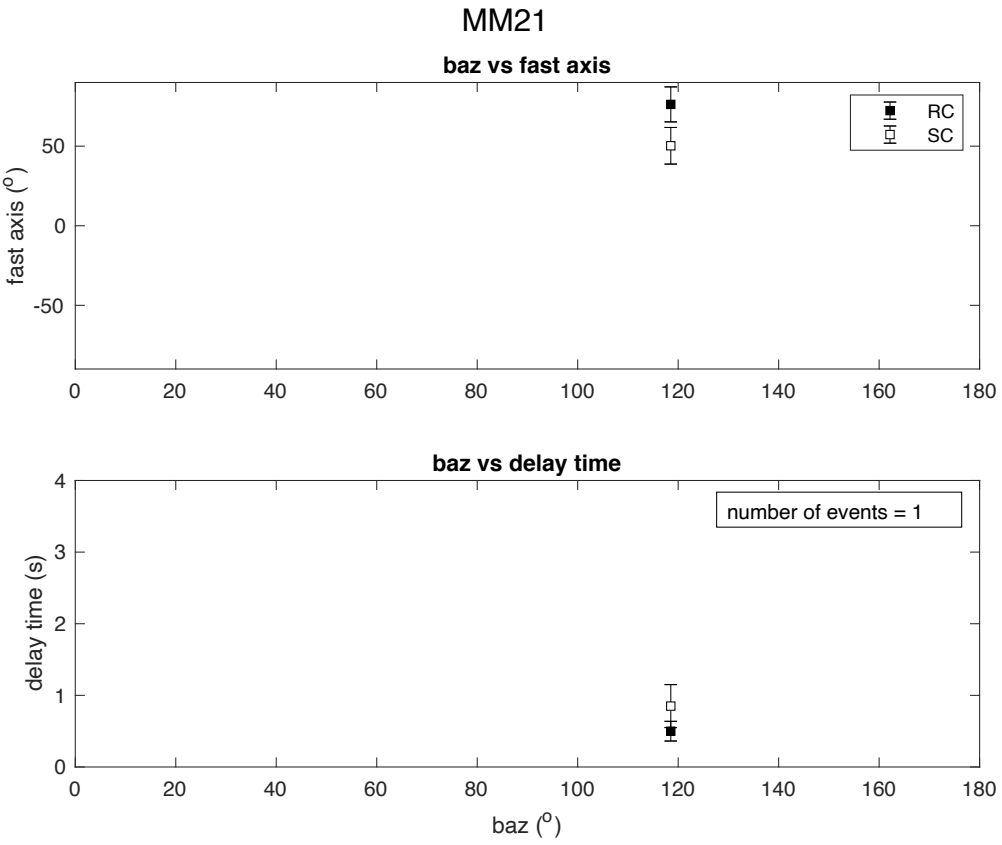

Figure A.19: Individual station results for MM21. Same notation as Figure A.1.

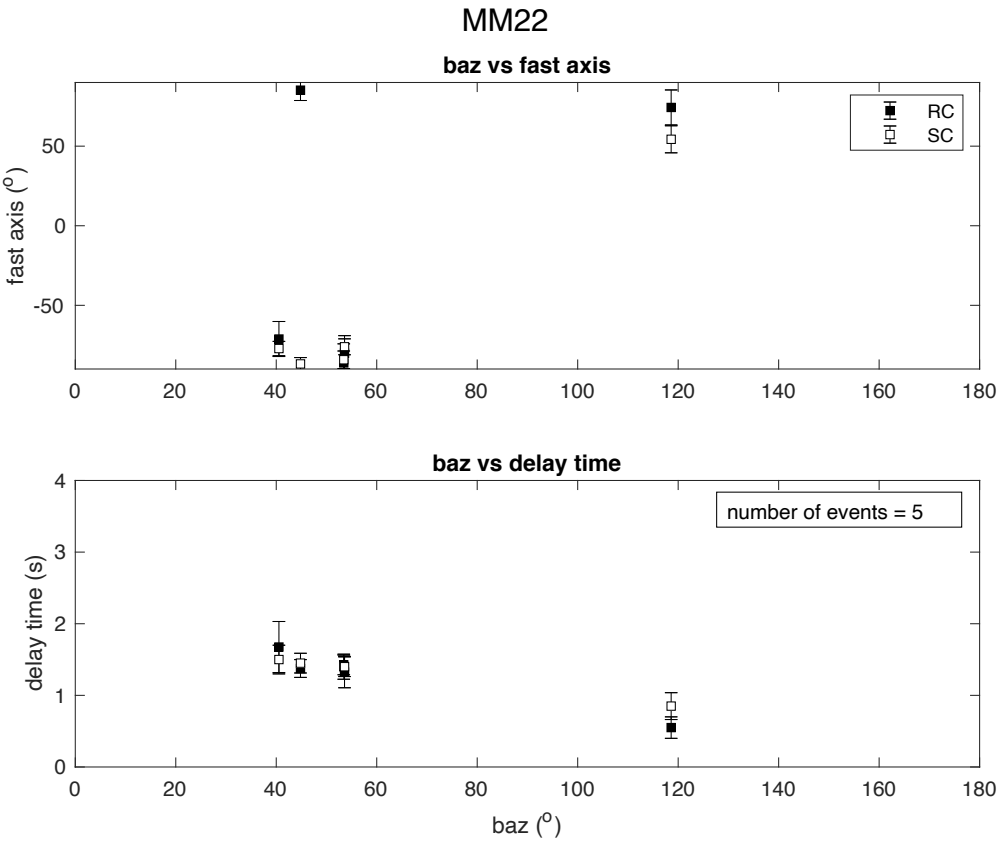

Figure A.20: Individual station results for MM22. Same notation as Figure A.1.

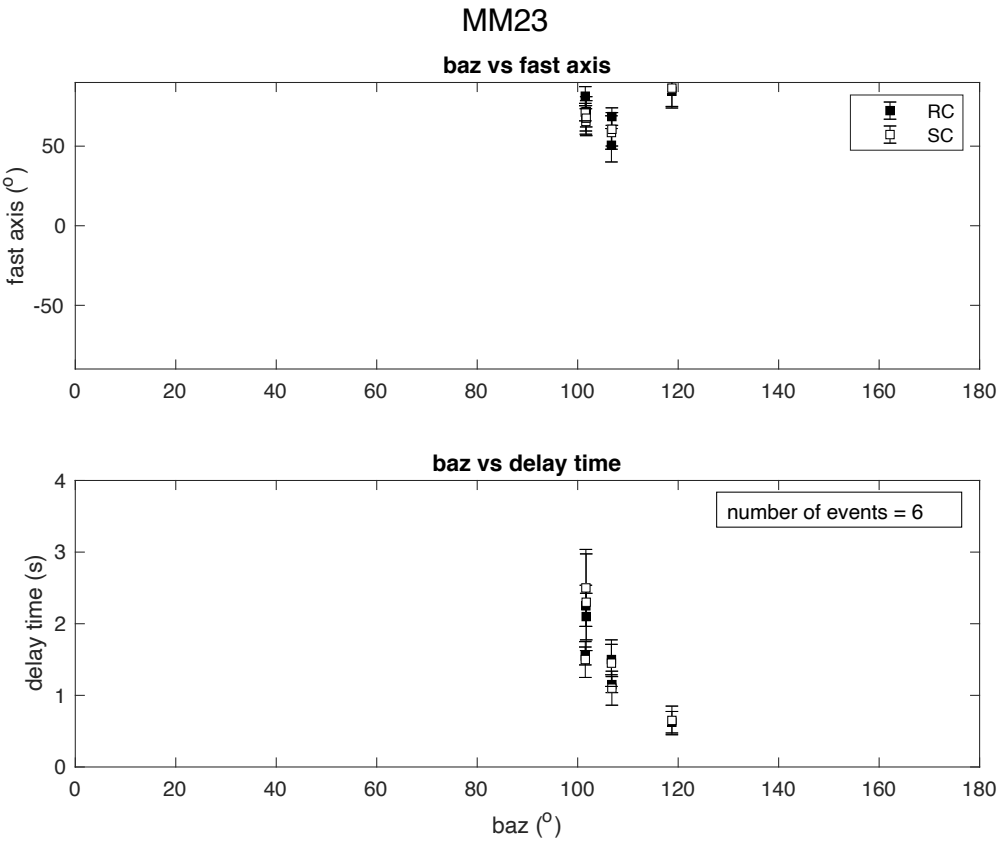

Figure A.21: Individual station results for MM23. Same notation as Figure A.1.

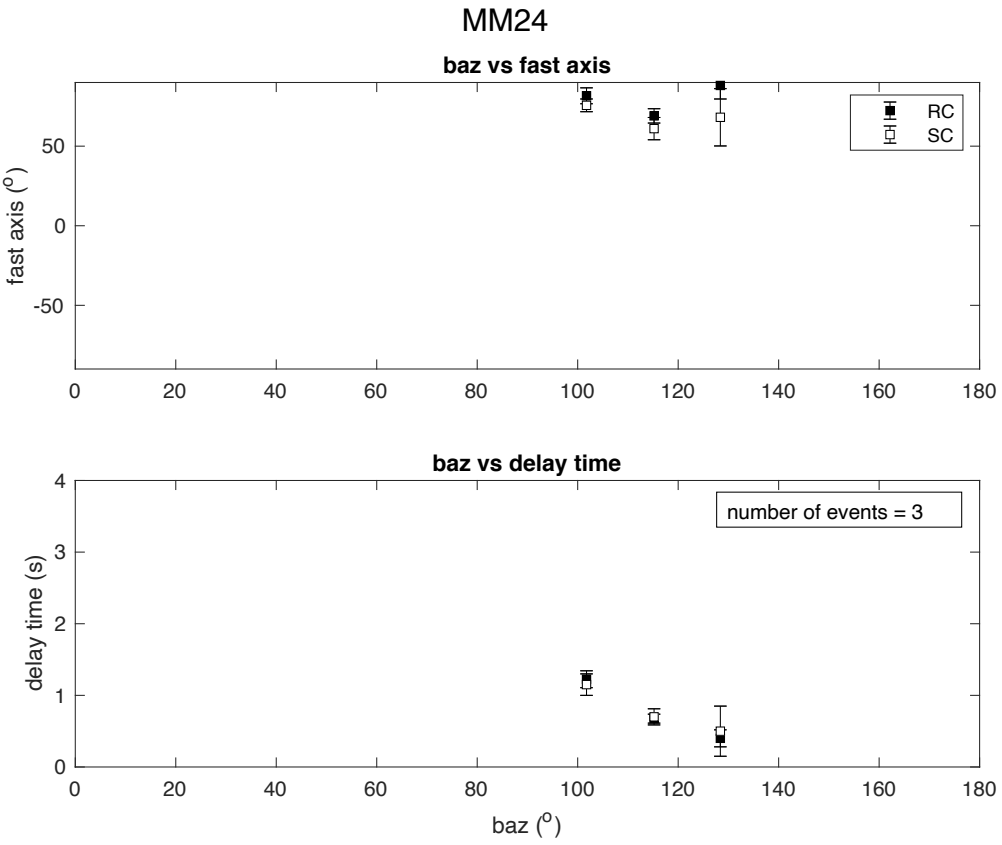

Figure A.22: Individual station results for MM24. Same notation as Figure A.1.

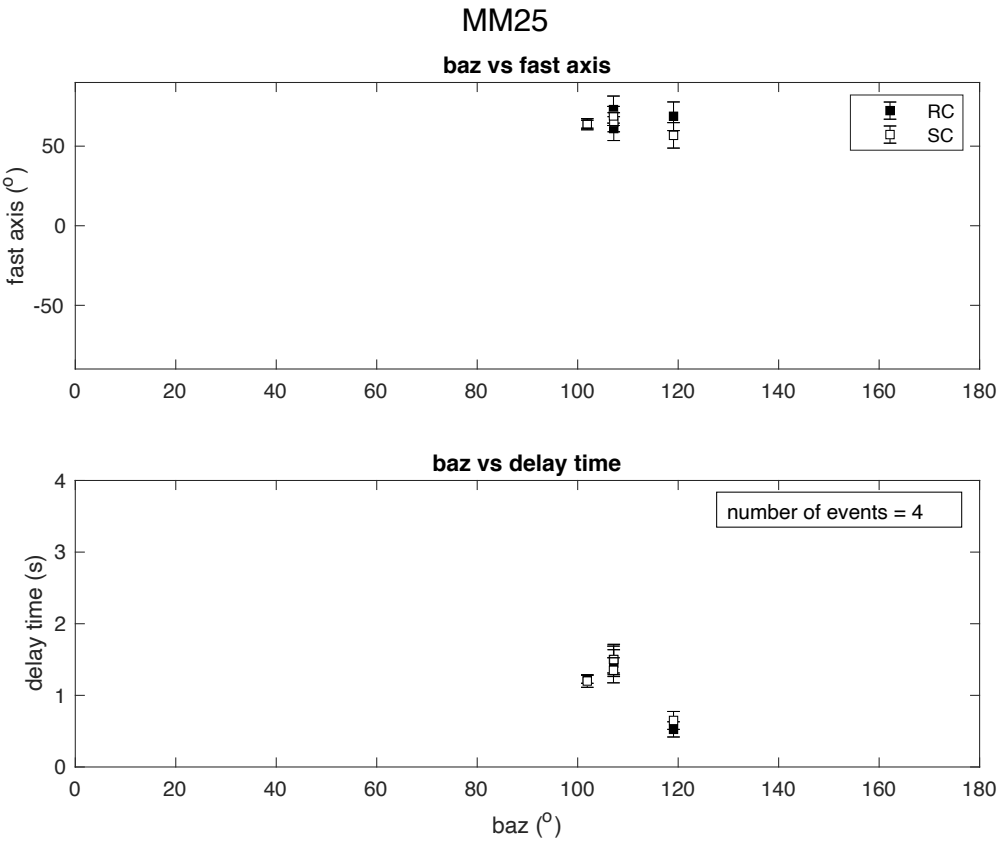

Figure A.23: Individual station results for MM25. Same notation as Figure A.1.

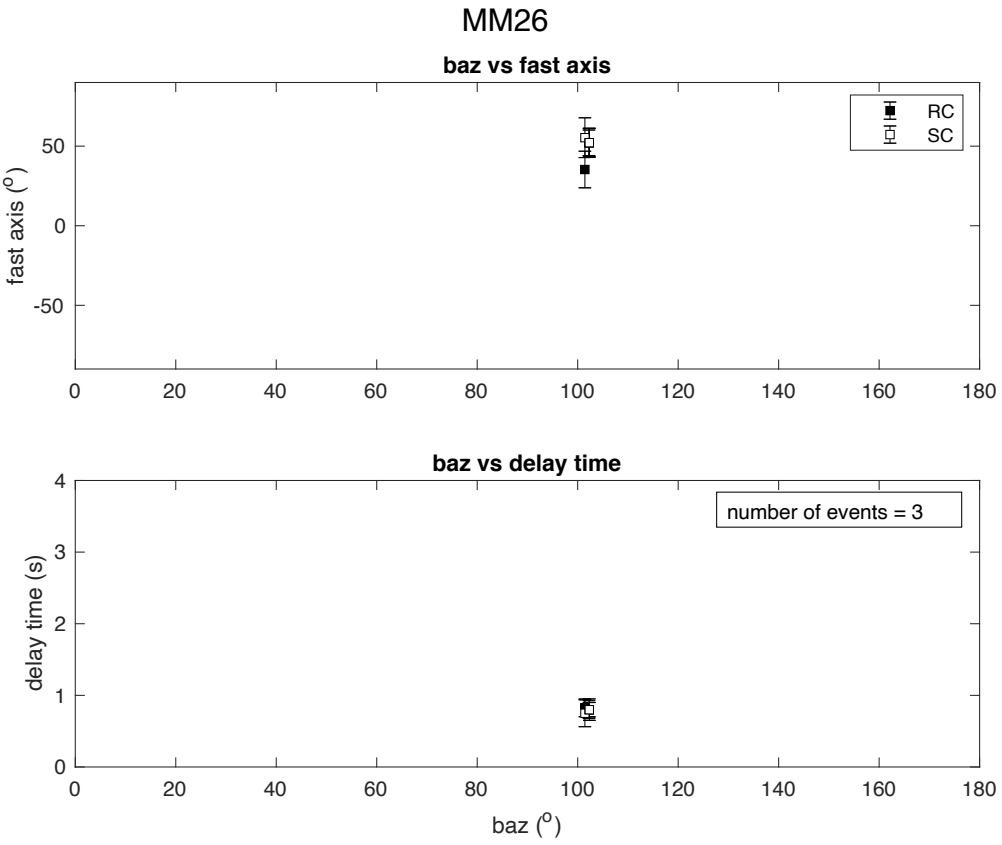

Figure A.24: Individual station results for MM26. Same notation as Figure A.1.

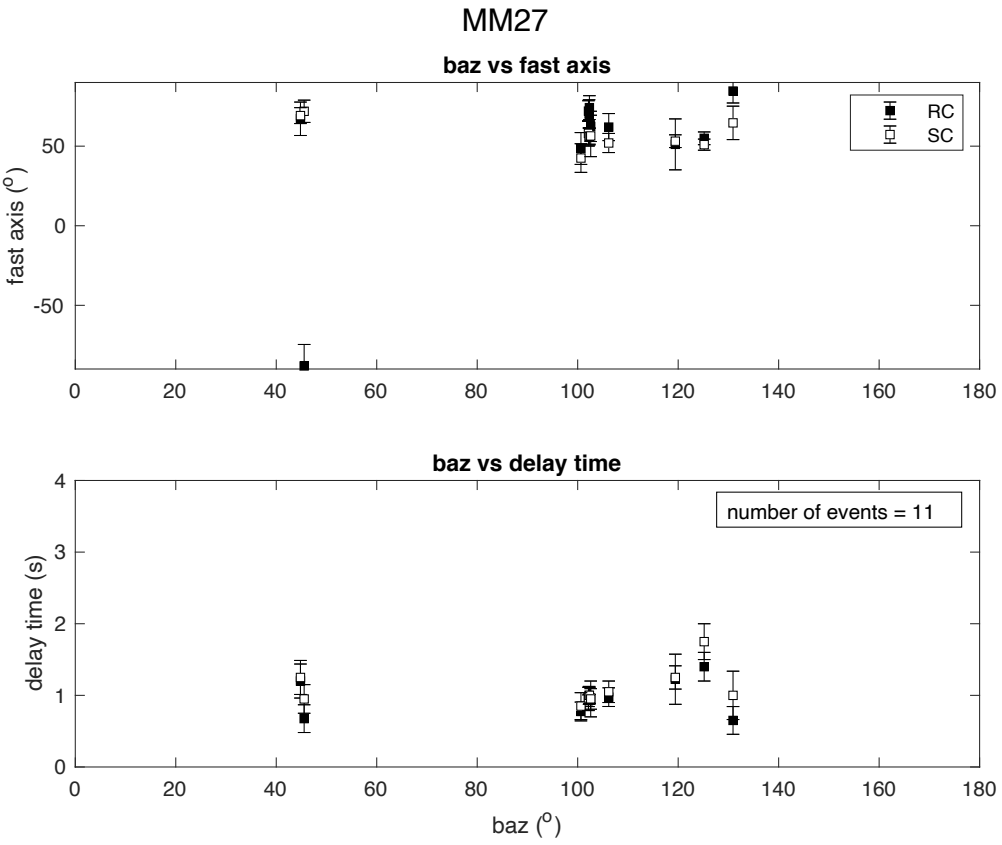

Figure A.25: Individual station results for MM27. Same notation as Figure A.1.

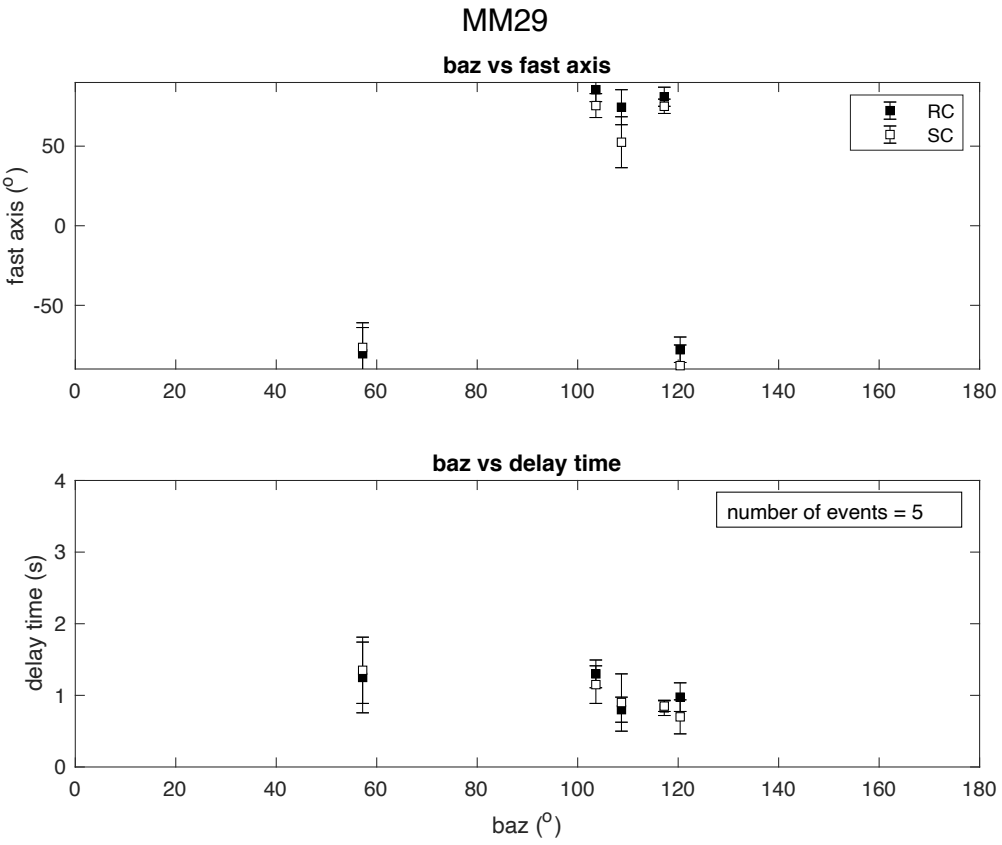

Figure A.26: Individual station results for MM29. Same notation as Figure A.1.

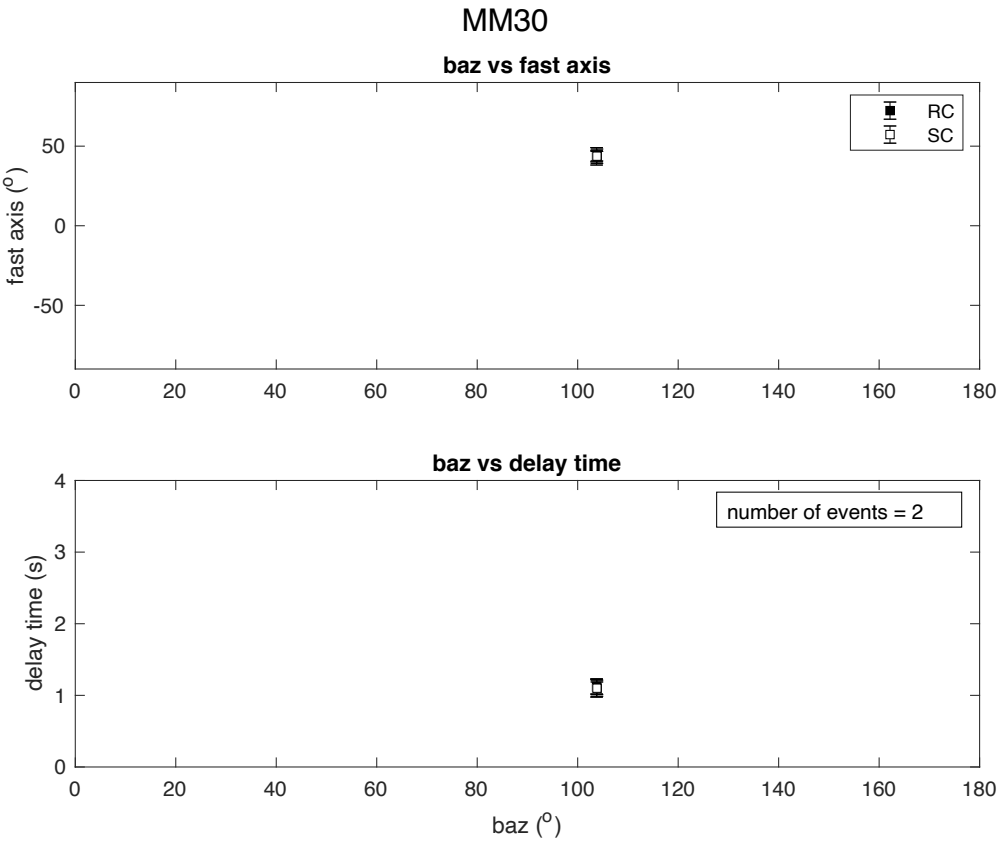

Figure A.27: Individual station results for MM30. Same notation as Figure A.1.

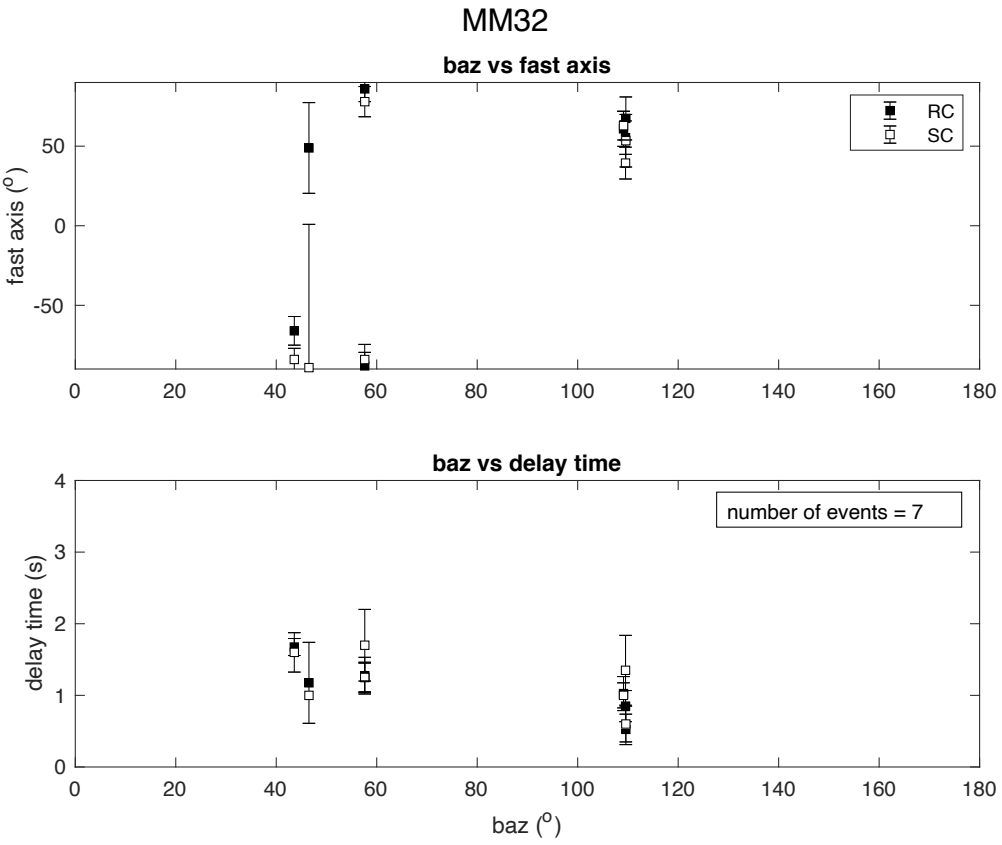

Figure A.28: Individual station results for MM32. Same notation as Figure A.1.

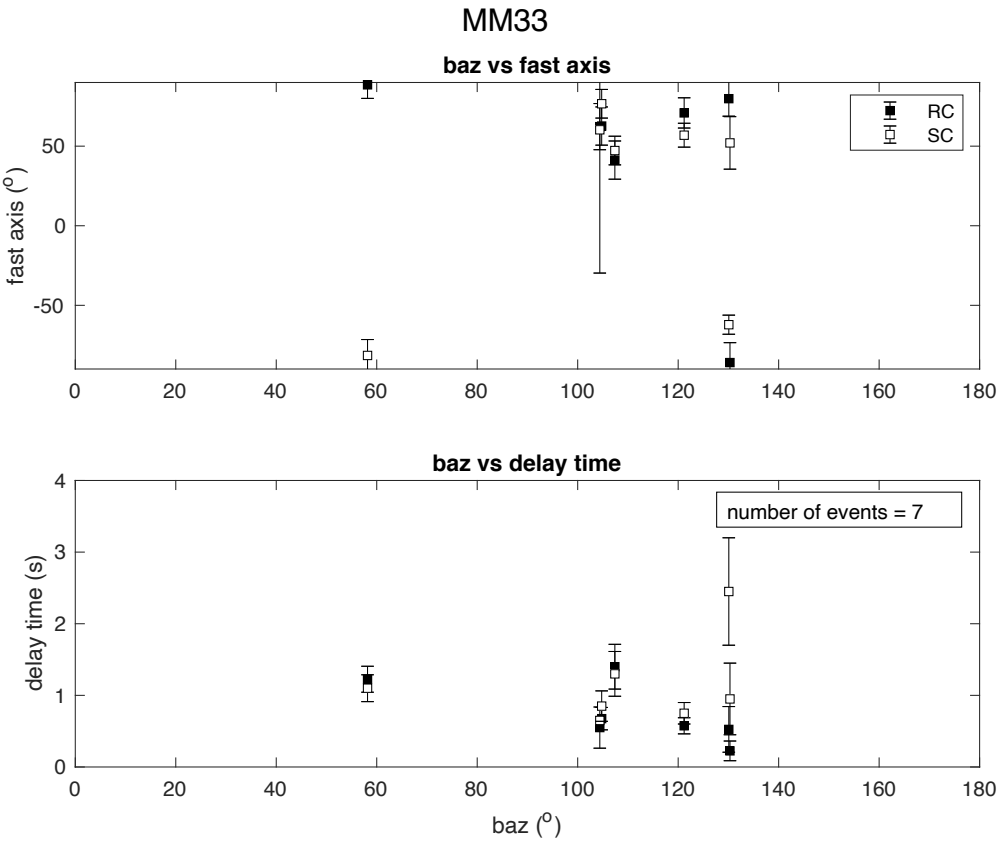

Figure A.29: Individual station results for MM33. Same notation as Figure A.1.

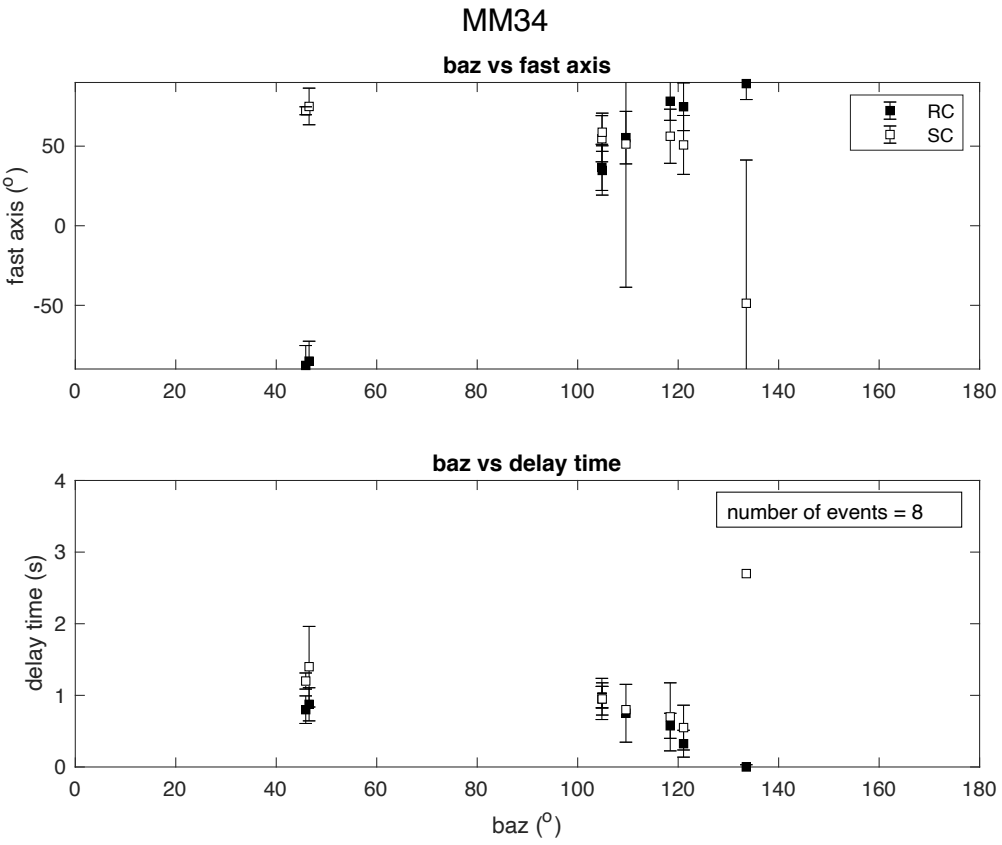

Figure A.30: Individual station results for MM34. Same notation as Figure A.1.

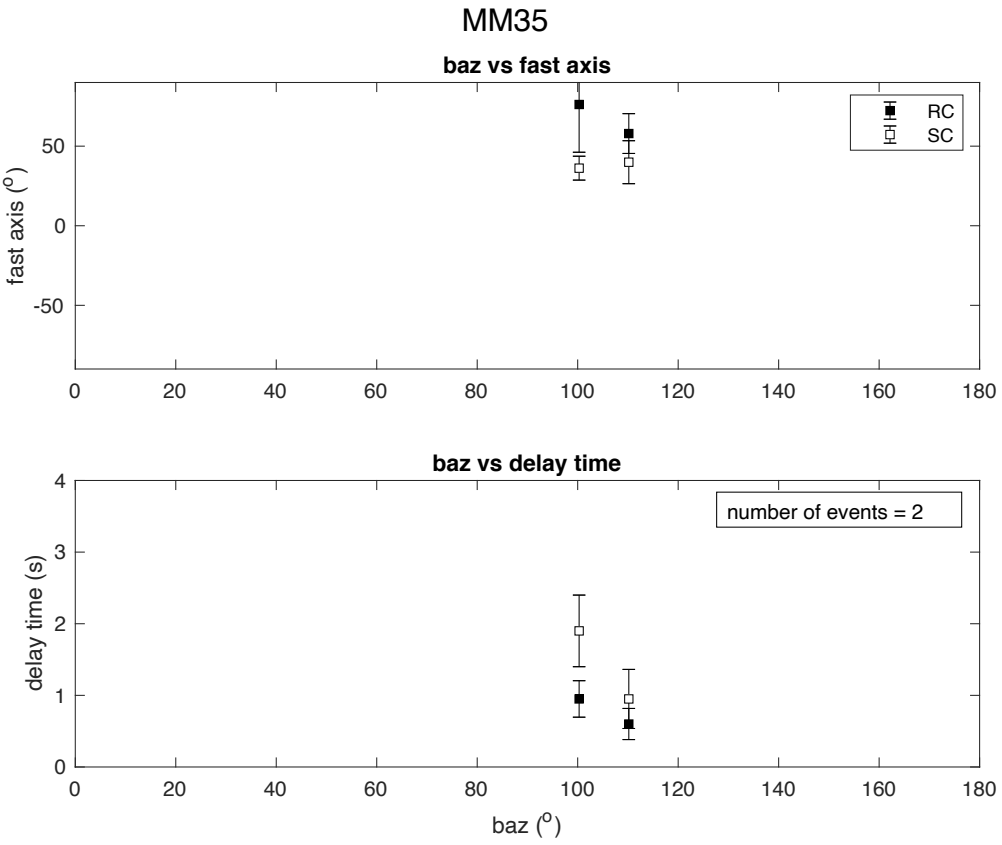

Figure A.31: Individual station results for MM35. Same notation as Figure A.1.

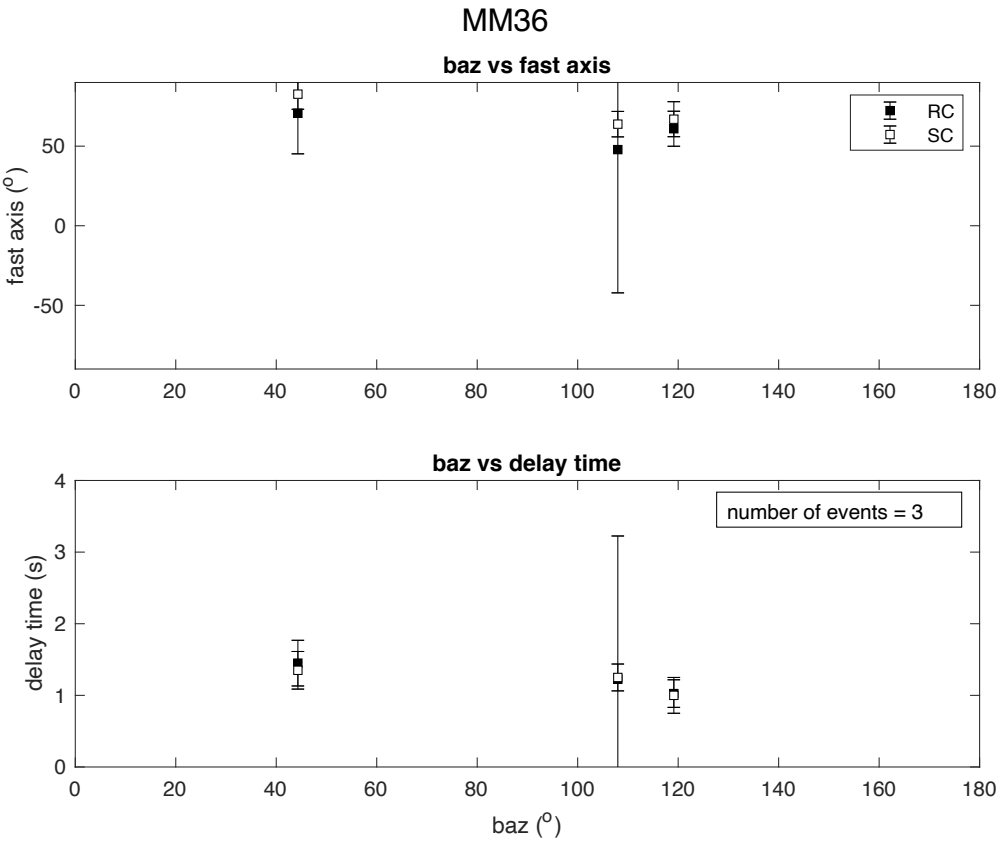

Figure A.32: Individual station results for MM36. Same notation as Figure A.1.

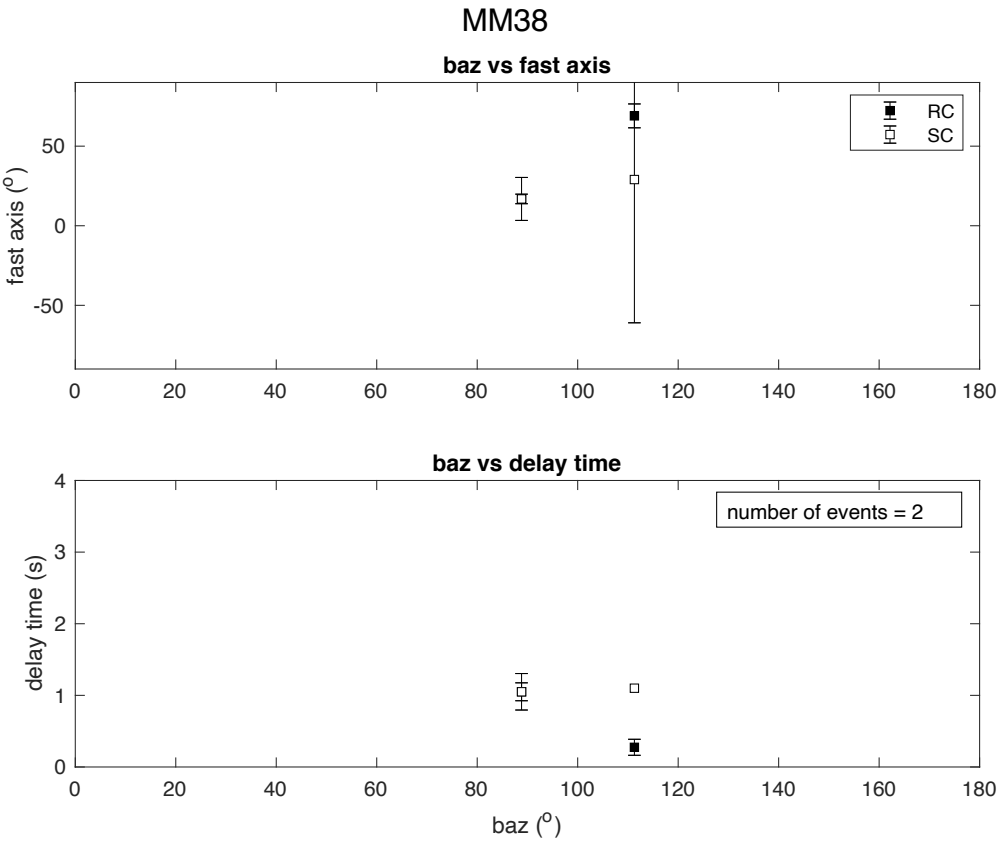

Figure A.33: Individual station results for MM38. Same notation as Figure A.1.

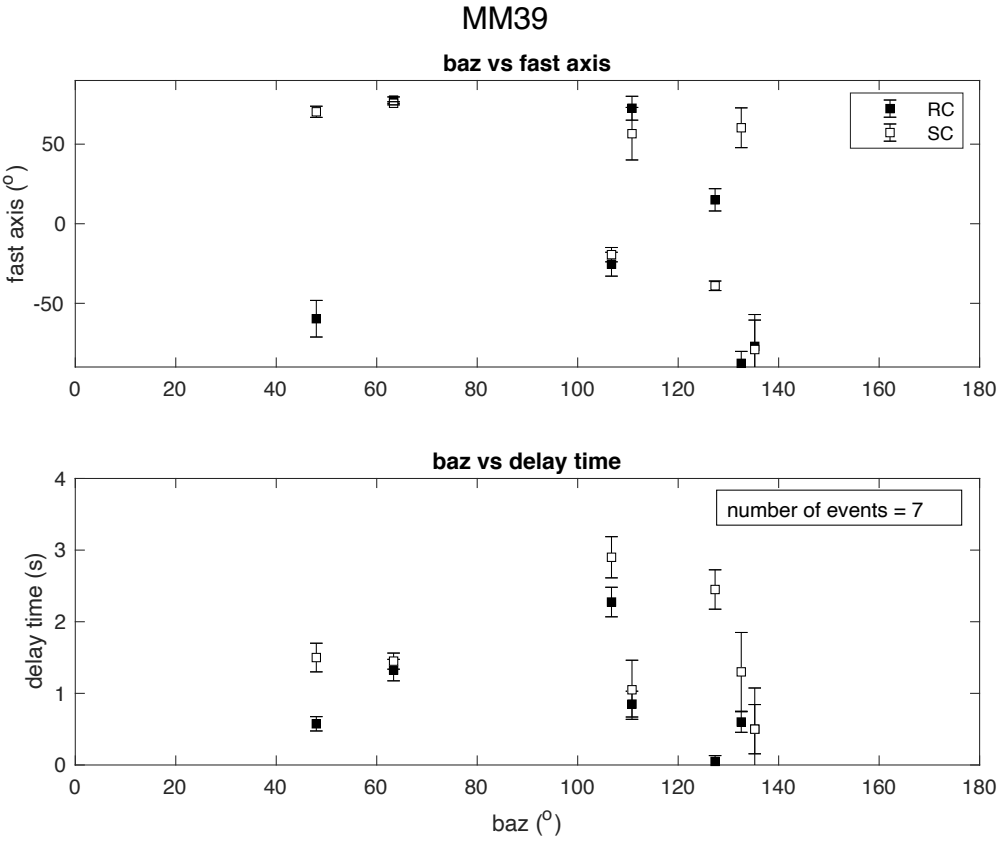

Figure A.34: Individual station results for MM39. Same notation as Figure A.1.

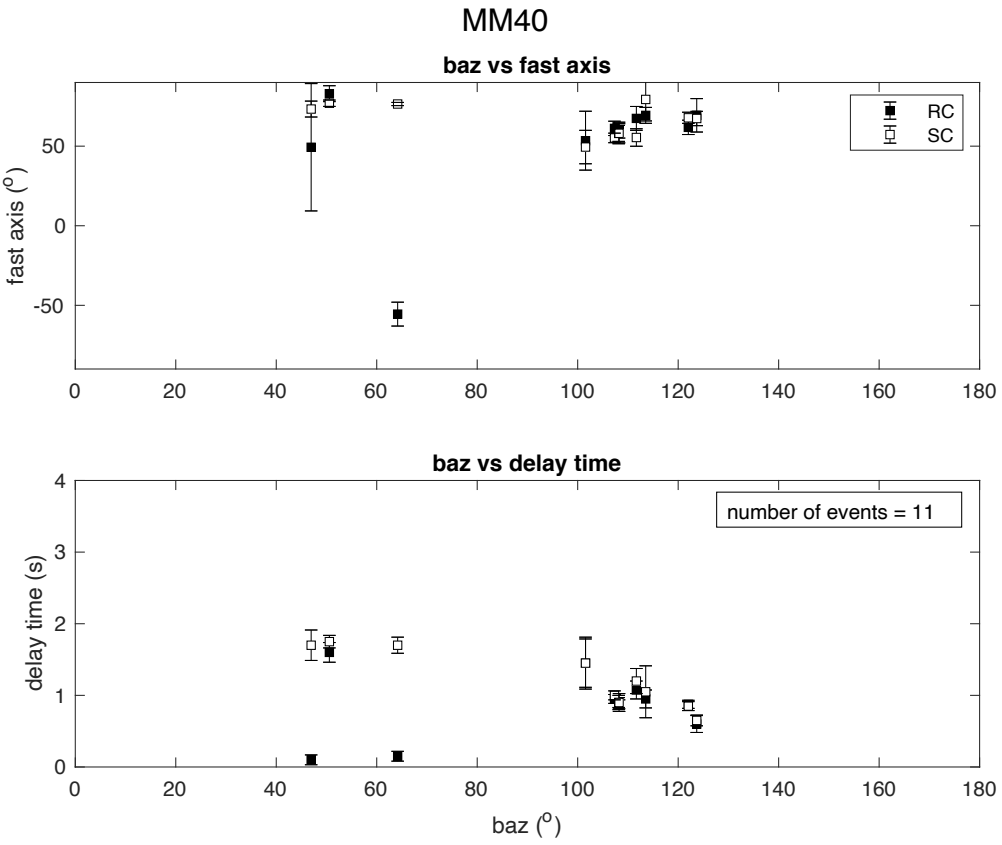

Figure A.35: Individual station results for MM40. Same notation as Figure A.1.